DISS. ETH Nr. 16455

Steps towards Structural Information in ESI-MS Gas Phase Investigations

A dissertation submitted to the

EIDGENÖSSISCHE TECHNISCHE HOCHSCHULE ZÜRICH

in partial fulfillment of the requirements

for the degree of

Doctor of Natural Science

presented by

Rolf Dietiker

Dipl. Chem., ETH Zürich

born 17.08.1975

citizen of

Bülach (ZH) and Thalheim (AG)

accepted on recommendation of

Prof. Dr. Peter Chen, examiner

Prof. Dr. Detlef Günther, co-examiner

Zürich, 2005/6

Meiner Frau Monika in Dankbarkeit.

Acknowledgement

At the end of my thesis it remains to thank many people working with me during that time.

I want to thank...

... Prof. Dr. Peter Chen for supporting me and contributing with many ideas and the possibility to work with all the equipment.

... Prof. Dr. Detlef Günther for the interest on the topic and all the time spent with the Co-Referee on this project.

... Rene Dreier for all the construction work on the drift tube and repair help on lab equipment and machines.

... Heinz Benz and Leo Weissberg (†)[1] for the help on the electronic development and the innumerable fixes on the electronics of the in-house built and all other equipment.

... Fabio Dilena for the preparation of the DCC quenching samples of the Zr-Ar ethyl polymerization complexes.

... Christian Adlhart for the important and interesting collaboration and discussions and the introductions on the MS machines.

... Christian Hinderling for the introduction on the MS machines and the important startup help on this project but who unfortunately left this group at an early stage of this project.

... Ruedi Hartmann for the good cowork on the cooled spray head unfortunately leaving this project due to a promising hydrogenation project and for being such a good colleague in the lab.

... Andreas Bach for the indefatigable reading and correction of this dissertation and a lot of interesting discussions.

---

[1] Leo Weissberg, the predecessor of Heinz Benz unfortunately died during the time this thesis.

. . . Eva Zocher for the interest and cowork on the serine mobility project and the cowork on the CID threshold measurements on copper complexes hoping to have transferred as much knowledge about our MS equipment as possible.

. . . All the rest of the group especially the members of our lab for having such a good working place atmosphere.

. . . Moni my beloved wife for all the love and patience waiting many evenings too long alone at home.

Published Parts of this Thesis

Reviewed Articles

- R. Dietiker, P. Chen, *in preparation*, **2006** (Publication about chapter 6).

- R. Dietiker, P. Chen, *Angew. Chem. Int. Ed.*, **2004**, 43 (41), 5513-5516.

Posters on Conferences

- 14th International Symposium on Homogeneous Catalysis ISHC-14, Munich, Germany, July 5-9, 2004
  "Extending ESI-MS gas phase methods used for investigation on reactive organometallic catalysts"; R. Dietiker, P. Chen

- Heidelberg Forum of Molecular Catalysis, Germany, June 27th, 2003
  "Separation of Isobaric Ions by High-Pressure Ion Mobility Measurements Coupled to an ESI-Tandem-MS"; R. Dietiker, P. Chen

- International Conference on Reactive Intermediates and Reaction Mechanisms, Ascona, Switzerland, July 7-12, 2002
  "Resolution of Isobaric Ions in a Conventional ESI-Tandem-MS by Ion-Mobility-Measurements"; R. Dietiker, Ch. Adlhart, P. Chen

- Heidelberg Forum of Molecular Catalysis, Germany, Dec. 7th, 2001
  "Resolution of Isobaric Ions in a Conventional ESI-Tandem-MS by Low-Pressure Ion-Mobility-Measurements"; R. Dietiker, Ch. Adlhart, P. Chen

- SCS Fall Meeting, Zurich, Switzerland, Nov. 12, 2001,
  "Resolution of Isobaric Ions in a Conventional ESI-Tandem-MS by Low-Pressure Ion-Mobility-Measurements"; R. Dietiker, Ch. Adlhart, P. Chen

Contents

Abstract

Electrospray mass spectrometry (ESI–MS) gas phase methods were extended by the addition of structural information by ion mobility spectrometry.

In a first attempt a conventional Electrospray ionization tandem mass spectrometer (ESI–MS/MS) was used to determine collision cross sections for aniline-H^+ and derivatives as well as for isobaric ions by applying retarding potentials at the exit of the collision cell. Literature values are reproduced, but the resolution is too low to achieve separation of analyte ions according to their collision cross sections.

A literature evaluation of different ion mobility setups was made followed by successful construction of a high pressure high field mobility cell fitting to the entry of a TSQ 700 triplequad ESI–MS. The complete hardware setup including electronic supplies was developed as well as driver software and spectra workup routines for different measurement modes.

Test measurements were performed with different analyte systems showing good performance and separation capabilities. A resolution factor of 50 ($t_d/\Delta t_{fwhm}$) was achieved as well as base line separation at the level of 6% difference in collision cross section. Literature values for o-/m-/p-phthalic acid dimethylesters are well reproduced as well as for aniline-H^+ and derivatives.

Ion mobility measurements on different catalytic systems and organic compounds were performed. In most cases the application of ion mobility measurements was new. Collision cross sections were measured of most of these species but however in some cases the designated separation could not be achieved. Based on these (negative) results improvement proposals are made.

On serine octamer clusters up to 8 different isobaric species were detected right at the border level of successful desolvation. The species could be assigned successfully to calculated literature structures. The detection of multiple species in this case is in

contrast published results on a different measurement setup.

Investigations on ethylene polymerization by access over quenching with DCC were made. A set of model compounds was used to measure the collision cross sections of differently branched isomers. The measurements and mobility calculations are in good agreement. Size selected Branching ratios were delimited by peak form integration.

In another project reactivity studies on the ionic Ir(PHOX) complex, an asymmetrical hydrogenation catalyst, were performed using mass spectrometry gas–phase reactions. Mechanistical pathways could be explored by related complexes. The reaction indicate that the hydrogenation proceeds by an Ir^{I}/ Ir^{III} rather than by the previously proposed Ir^{III}/ Ir^{V} polyhydride route.

Additionally a new, faster method for CID threshold measurements and improvements thereof in terms of energy distribution and reproducibility was introduced. The method is currently used for investigations on a large set of Cu^{I}(BOX) and Cu^{I}(PyBOX) complexes to measure absolute metal–ligand binding constants.

Zusammenfassung

Elektrospray-Massenspektrometrie- (ESI–MS) Gasphasenmethoden wurden erweitert durch die Hinzufügung von struktureller Information mit Hilfe von Ionenmobilitätsspektrometrie.

In einem ersten Versuch wurde ein konventioneller Elektrospray-Ionisations-Tandem-Massenspektrometer (ESI–MS/MS) dazu benutzt, Kollisionsquerschnitte von Anilin-H$^+$ und dessen Derivate, aber auch von isobaren Ionen mittels Bremspotentialen am Ausgang der Kollisionszelle zu messen. Dabei konnten Literaturwerte reproduziert werden. Allerdings ist die Auflösung zu gering, um eine Trennung der Ionen zu erzielen.

Literatur über verschiedene Ionenmobilitäts-Messanordnungen wurde evaluiert. Anschliessend wurde erfolgreich eine Hochdruck-Hochfeld-Ionenmobilitätszelle, welche auf das Quellen-Interface eines kommerziellen TSQ 700 triplequad ESI–MS passt, konstruiert.

Testmessungen mit verschiedenen Analyten zeigten gute Performance und gutes Trennvermögen. Ein Auflösungsfaktor von 50 ($t_d/\Delta t_{fwhm}$) und eine basislinienaufgelöste Trennung im Bereich von 6% Unterschied im Kollisionsquerschnitt wurde erreicht. Literaturwerte für o-/m-/p-Phthalsäuredimethylester und Aniline-H$^+$ und dessen Derivate werden gut reproduziert.

Ionenmobilitätsmessungen an verschiedenen Katalysatorsystemen und organischen Verbindungen wurden durchgeführt. In den meisten Fällen war die Applikation von Mobilitätsmessungen neu. Für die meisten Verbindungen konnten Kollisionsquerschnitte gemessen werden, leider konnte aber in einigen Fällen die erhoffte Separation nicht erreicht werden. Basierend auf diesen (negativen) Resultaten konnten wichtige Verbesserungsvorschläge gemacht werden.

Für Serin-Oktamer-Cluster wurden knapp an der Grenze von erfolgreicher Desolvatation 8 verschiedene isobare Spezies detektiert. Sie konnten erfolgreich errechneten Strukturen aus der Literatur zugeordnet werden. Dieses Resultat steht im Gegensatz zu publizierten Resultaten mit einer anderen Messanordnung.

Über Quenching mit DCC konnten Untersuchungen an Ethylen-Polymerisazions-produkten durchgefürt werden. Die verschiedenen Kollisionsquerschnitte von verschieden stark verzweigten Isomeren wurde mittels einem Set von Modellverbindungen gemessen. Die Messungen und entsprechende Mobilitätsrechnungen zeigen gute Übereinstimmung. Es konnten grössenselektierte Verzweigungsraten mit Hilfe von Peakform-Integrationen bestimmt werden.

In einem weiteren Projekt wurden mit massenspektrometrischen Gasphasen-Reaktionen Reaktivitätsstudien am ionischen Ir(PHOX)-Komplex, ein asymmetrischer Hydrierungskatalysator, gemacht. Mit verwandten Strukturen konnten mechanistische Pfade aufgeklärt werden. Die Reaktionen zeigten, dass die Hydrierung eher über einen Ir^{I}/Ir^{III} als einen vorgängig publizierten Ir^{III}/Ir^{V} Polyhydrid-Pfad abläuft.

Des Weiteren wurde eine neue, schnellere Methode für CID-Threshold-Messungen zusammen mit Verbesserungen in Bezug auf Energieverteilungen und Reproduzierbarkeit eingeführt. Die Methode wird im Moment für Untersuchungen an einem grossen Set von $Cu^{I}(BOX)$– und $Cu^{I}(PyBOX)$–Komplexen verwendet um absolute Metall–Ligand-Bindungkonstanten zu messen.

Chapter 1

Introduction

1.1   Chemical Background

Transition metal chemistry is a rapidly evolving field in chemistry. Transition metal compounds come in a huge structural variety and their capability to perform catalytical reactions makes them relevant for industrial processes utilizing homogenous catalysis based on transition metal complexes. The industrial catalyst business is worth more than 10 billion euro per year [1] and homogenous catalysts are also involved in many key steps in the synthesis of natural products.

Especially efficient carbon–carbon bond forming reactions are of major interest. One of the main focuses therein is the controlled formation of oligomers and polymers out of cheap carbon sources such as in ethylene polymerization reactions. Another important field for modern chemistry are well defined asymmetric hydrogenation reactions on various substrates. New catalysts even allow such hydrogenations on unfunctionalized olefins. Efficient further development of these and other important catalyst classes is conditioned on a detailed understanding of the mechanism of these systems including the key factors that control their activity and product selectivity.

However, studying mechanisms in transition metal chemistry is for several reasons a ticklish task. Often, catalytic reactions are multiple step reactions with many species in equilibrium with each other, the precatalyst, the catalytically active species, and substrate catalyst complexes, and they are very sensitive to solvents and counter ions. Usually these species cannot be separated and studied individually. Moreover, the potential surface around different reaction pathways is usually flat for transition metal complexes and small changes on a ligand can already completely alter the behavior of the whole catalytic system.

Most of the current analytical methods, especially those in solution phase, can investigate reaction mechanisms only as an unsharp picture by complete turnover characterization or are somehow limited to the product distributions without any insight into the important key steps.

In fact, many industrially used catalytic systems are not well characterized complexes but catalytic formulations or unseparated mixtures of components. In many cases even when defined complexes are used, the active form is a minor species within large amount of the inactive form.

1.2   Mobility and Gas Phase Chemistry

Studying transition metal reactions in the gas phase can circumvent many of theses limitations. The highly reactive intermediates can be generated in the gas phase and isolated in the vacuum. There, their intrinsic reactivity can be studied free from pre-catalyst/catalyst equilibria, free of solvent, and free of counter ions. Reactivity trends caused by different substrates or ligand sets can be attributed to individual reactive steps and are therefore easier to interpret.

Electrospray ionization tandem mass spectrometry has recently been demonstrated to be a versatile technology to transfer catalyst ions into the gas phase and to perform ion molecule reactions with the substrates of interest [2–6]. There it was also found empirically that the gas phase reactivity of transition metal complexes paralleled solution phase reactivity. In some cases the methodology allowed screening on a large library of catalysts prior to be synthesized and characterized as single compound.[7] Therefore electrospray ionization mass spectrometry (ESI-MS) has become the method of choice in our group gaining more and more importance in reaction screening techniques also in other groups.[2,8]

The main deficiency of conventional mass spectroscopy is that ions are only separated by their mass over charge ratio (m/z) and therefore ions with the same m/z (isobaric or isomeric ions) but different structure remain unresolved.

In this thesis the main focus is an attempt to introduce the missing geometrical information into the described ESI–MS gas phase investigations trough the measurement of collision cross sections using ion mobility spectrometry (IMS). IMS is a quite old method but was recently improved to give high resolution.[9–12]

Beside this, investigations on reaction mechanisms with extended sampling techniques as well as technical improvements in advanced measurement methods are also important parts of this thesis.

Part I

Development of Ion Mobility Measurements as Tool for Gas Phase Chemistry

Chapter 2

Ion Mobility – Introducing Geometrical Information in Mass Spectrometry

Summary

A deficiency of conventional mass spectroscopy is that ions are only separated by their mass over charge ratio (m/z) leaving ions with the same m/z but different structure unresolved. Ion mobility spectrometry (IMS) in high resolution setups published in the last 5 to 10 years can provide this separation in gas phase reactions.

2.1   Introduction

The main deficiency of conventional mass spectroscopy is that ions are only separated by their mass over charge ratio (*m/z*) and therefore ions with the same *m/z* (isobaric or isomeric ions) but different structure remain unresolved. A widely used technique to distinguish isobaric ions is the different fragmentation patterns obtained in collision induced dissociation (CID) experiments which can even be used to distinguish between enantiomers when chiral auxiliaries are used[13–17]. A small mass displacement of isobaric ions is also observed in quadrupole ion traps.[18–21] The explanation for the shift could either be the presence of neutral collision partners and therefore an influence of the collision cross section or the claimed dipole difference in the publications whereas the first explanation seems to be more reasonable. Nevertheless under special conditions these ions can even be separated[22].

Beside these methods the introduction of high resolution mass spectrometry techniques such as fourier transform ion cyclotron resonance mass spectrometry (FT-ICR MS) can also yield structural information by calculation of accurate energies and the corresponding mass defect of the the different species combined with multiple step fragmentation experiments[23].

One of the most important geometrical information on target molecules in gas phase reactions is about their 3D folding. Especially for larger molecules the folding and the resulting surface would have the most important impact on their reactivity. For example in the large field of asymmetric catalysts this is one of the key issues. For the methods described before, this is the most complicated information to obtain.

In the investigations of reaction pathways of organometallic catalysts via selected steps in the gas phase within a triple quad mass spectrometer as performed in our group[3–5, 7, 24–42] the real structures of the target molecules is in most cases the most important information. This information is often complicated or almost impossible to obtain with the given experimental setup. Therefore several possible structures have to be evaluated by other mostly theoretical methods.

To obtain this information a different approach which additionally has the possibility to be coupled to our quadrupole mass spectrometers would be a suitable choice for the gas phase reaction projects investigated in our group.

2.2   Ion Mobility – Revival of an Old Technique

One of the oldest and easiest methods to separate ions in the gas phase beside by their mass is to distinguish them by their collision cross section by ion mobility spectrometry (IMS), where the drift behavior of ions is measured along an electric field gradient against a stationary drift gas. In the case of a non reactive gas and soft collisions this can be understood in the simplest picture just as by their geometrical size. Using reactive drift gases could allow a direct observation of specific surface reactivity.

IMS has been known for more than 40 years as an analytical method[43] and has been described almost 100 years ago[44]. Even the first electrospray source was coupled with a drift tube[45]. This technique has been used analytically mainly for the analysis of trace organic vapors, especially for compounds such as explosives, drugs, and chemical warfare agents[46, 47]. The field detection of these analysts is currently probably the most widely used application for portable IMS analyzers. For example the Swiss Army uses such systems in large numbers as common detector called "CNG" or "SwissCam"[48] for the detection chemical warfare agents shown in figure 2.1 below.
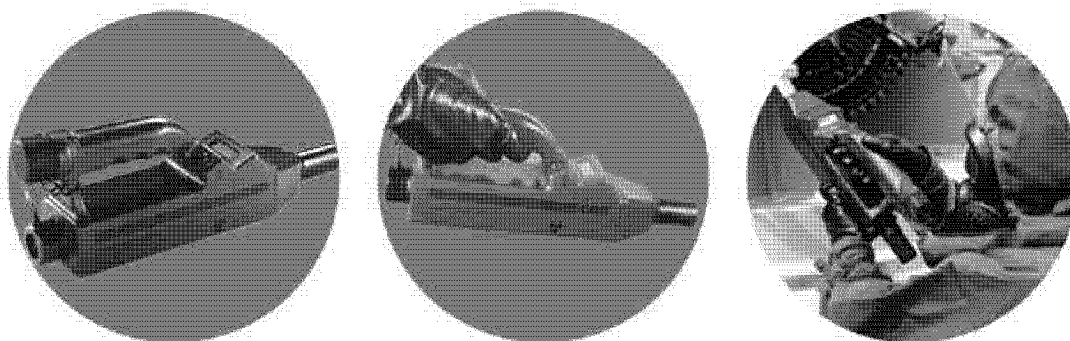
Figure 2.1: The Portable Mobility Cell Used in The Swiss Army for Chemical Warfare Detection (SwissCam or CNG)[48]

In the early years in some publications ion mobility was named plasma chromatography but as important difference to typical chromatography methods (as GC or HPLC) the interactions between the phases and therefore the resulting retention (or drift) times can be described, modelled and predicted in a reliable way.

Recently, high resolution mobility cells with resolution power > 30 have been developed by Clemmer and Hill [9–12]. These even allow the separation of peptide libraries by small differences in their folding behavior or the separation of chloroaniline versus iodoaniline.

2.3   Basic Ion Mobility Spectrometer Classes and Techniques

During the past 40 years many different classes and techniques for the measurement of ion mobilities through the measurement of either the drift time or the velocity of ions in different pressure ranges have been developed.

A method which will not be further discussed in this thesis is called field asymmetric waveform ion mobility spectrometry (FAIMS) in which a non-constant electrical field is applied along the drift region. For small field changes ions show an almost linear dependence on the electrical field strength for their drift behavior. Nevertheless changing the field strength in a wide range will usually cause a nonlinear dependency. In this method ions are separated using the asymmetric field dependency of their drift behavior applying a asymmetric waveform to the electrodes. This method is commonly used in different applications [49–54] but a simulation of the spectra is currently not available which was one of the most important features for a direct geometrical investigation.

2.3.1   Pressure Ranges and Limitations

To initiate a mobility experiment, ions are usually introduced into a region ("drift tube") filled with a defined pressure of a collision gas or a gas mixture. The movement and the correlated current kinetic energy E_{kin} of an ion is controlled by its initial kinetic energy (by previous acceleration)E_0, the retardation by collisions with the gas molecules ΔE_{coll} and by an acceleration with the field intensity E if an electrical field is applied along the drift region[55].

Basically two important pressure regimes are used in a mobility experiments. Both are classified by the the behavior of the ions at zero drift field conditions (e.g. no

electrical field is applied along the drift region).

- **low pressure limit:** This is fulfilled at low pressures when the initial kinetic energy is high enough to let the ions pass the whole length of the drift region without an applied field along the region. In this case the terms of the initial kinetic energy E_0 and local acceleration have to be included in a physical description of the movement.

- **high pressure limit:** This is fulfilled at high pressures where the ions would completely lose their drift velocity within a small fraction of the drift region length if no field is applied. Under these conditions, applying a uniform field, the comparatively small initial kinetic energy E_0 can be neglected and the local acceleration by the electrical field is in equilibrium with the retardation by collisions. This ends up in a field dependent constant drift velocity.

For these limits two specific physical descriptions can be made which will be discussed in more detail and as practical application in chapter 3 for the elastic collision model under low pressure limit conditions and in chapter 4 for a collection of models under high pressure limit conditions.

2.3.2 Most Commonly used Sources

Almost all important analytical ion sources can be used in IMS. The four most common ion sources were used:

▶ Electrospray ionization (ESI) [9,11,12,56,57]

✳— (UV-)LASER ionization (mostly pulsed) [58–62]

❈ Radioactive irradiation ionization with Ni-63[46] or Am-241 (commercial)

ϟ electron impact ionization[63–65]

Some IMS cells are also coupled to the exit of other ion separation or storage devices such as ion traps [9,12,56,66], sector [67] or quadrupole mass filters [11,60–65] or reaction chambers[66].

2.3.3   Additional Timing or Selection Devices

To measure the desired drift behavior of the ions either the drift time through a drift region of a defined length or in the low pressure limit the remaining kinetic energy of an ion at the exit of the drift region can be measured. The remaining kinetic energy can be measured by stopping voltages at the exit region. (for more details s. chapter 3).

Measuring the drift times of the ions requires a timing or a package formation of the ions. This could be done with a pulsed source at the entry which is given directly for a pulsed LASER irradiation ionization or with pulsed fields or ion timing devices in the ionization region for EI or radioactive ionization. With all the mentioned ionization methods this could also be achieved using an ion trap to collect and reeject the ions which additionally also has the possibility to increase the molecule number density for weak sources.[9,10,12,56]
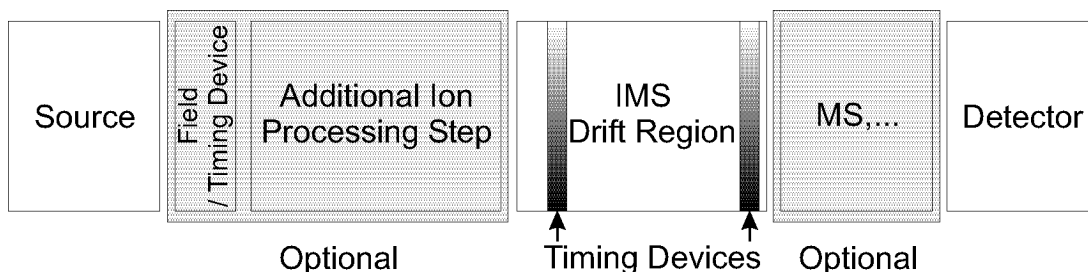
Scheme 2.1: A general setup (block scheme) for ion mobility measurements

Another more universal and more practical method is to add a timing device within or right before the drift region which is for example used in the high resolution mobility cell used in Hill's group[11,57]. This timing technique is also the method of choice in almost all setups with precoupled ion separation modules.

For the detection and separation of the ion packages a moderately fast time dependent detection (0.02–0.1 ms per time point for high resolution cells at high pressure limit) or a second timing device is required. A direct detection with electron multipliers, multi channel plates or simple electrodes with high amplification detection is also possible.

In many cases another mass separation step after the mobility measurement is used to extend the information content to a second dimension. The only suitable fast mass spectrometry technique with full 2D capability for a direct detection is time-of-flight mass spectrometry (TOF-MS)[49-52]. Nevertheless a second timing device after the mobility cell allows also slower mass detection techniques like quadrupole or sector mass filters to be used. Coupled to compact mass spectrometers of these types with short reaction times a time dependent measurement on a preselected mass (mass filter mode) can also be made without additional timing devices[9, 12, 56, 60-65]. A more detailed description of the most common timing methods can be found in chapter 4.

Some groups recently started to build more complicated coupling methods with up to three or four collision cells, mass filters and ion trap storage regions stacked together with an IMS cell which allow more specific applications such as library coupled peptide analysis[68] or even automated sequencing of peptides[49-52].

2.3.4   General resolution issues

The most important line broadening factor in mobility measurements is the thermal line broadening by the internal kinetic energy which has an effect on the observed drift path (timed measurement) as well as on the detected final kinetic energy (low pressure limit experiments with kinetic energy detection as described before). Distortions by a not completely uniform field are somehow small and the most distorted ions are usually collected by the walls of the drift tube.

In the low pressure low field limit a line broadening of several eV caused by the internal energy is large compared to the total loss of kinetic energy by collisions during the path through the drift cell. Since this is the available separation scale (several 10s up 200 eV) high resolution can not be achieved.

In high pressure applications starting at pressures of several mbar up to one bar the thermal movement is on one hand more decelerated by many more collisions and on the other hand a distribution up to 5 eV is small compared to the total field and the possible total loss of kinetic energy of several keV.

2.4   Conclusion – Experimental Approaches
to Introduce Mobility

While a large number of possible measurement setups with different advantages and disadvantages are described in literature the careful choice of the right method remained one of the important issues. At least for the ion source electrospray as the main ionization technique used in our group was confirmed to be a good choice by a large number of publications over a long time period.

A technically simple attempt to measure ion mobilties was demonstrated in 2000 by Bowers and coworkers[69] who measured the loss of kinetic energy that ions experience upon collisions in a conventional collision cell of a triple quad mass spectrometer. Due to the simple integration with our machines and because no additional building blocks had to be built and added to our machines, this method was used and extended as first attempt at mobility measurements with our equipment (s. chapter 3). These experiments work in the low pressure limit.

To meet the resolution and separation requirements for gas phase experiment projects[3–5, 7, 24–42] a high pressure drift tube fitting to a conventional TSQ 700 triple quad mass spectrometer has was built in a second attempt. The setup is based on described high resolution mobility cells at 1 bar directly coupled to a ESI source which is also used for peptide analytics most closely resembling the one used in Hill's group [11, 57]. The electrical field applied to the drift region in a series of evenly spaced metal rings is about 300 V/cm (s. chapter 4).

2.5 Ideas

A high resolution drift tube should open the access to a broad field of new experiments and extended results coupled with other gas phase reaction measurements. Possible target experiments are the detection of trans/cis isomers, branching ratios of catalysis products or living catalyst systems, or investigations on catalyst structures concerning the ligand and substrate locations and conformations. Other possibilities are the separation of enantiomeric ions with help of chiral additives to the drift gas over different binding constants as well as reactions under higher pressures in the drift tube for investigations of for example ethylene polymerization catalysts like the Brookhart[70] or Ziegler-Natta[71] type catalysts. Since both catalyst types were investigated in our group after preparation in liquid phase a gas phase coordination[41] or polymerization within the modified TSQ spectrometers were never successful probably because of the low concentration of ethylene at several mTorr for the given reaction cross section.

Chapter 3

Ion Mobility Measurement in a Conventional Mass Spectrometer [1]

Summary

A first experiment for directly probing three–dimensional structural information in the gas phase from collision cross sections uses the collision cell of a conventional mass spectrometer and retarding potentials. The performance of the setup is presented here as well as a short introduction into the electrospray ionization technique and tandem quadrupole mass spectrometry.

---

[1] All experiments that are described in this section have been elaborated in collaboration with Christian Adlhart from our group and where also part of his Ph. D. thesis.[28]

3.1 Introduction

In 2000, Bowers and coworkers[69] have demonstrated a new principle of ion mobility measurement, namely measuring the loss of kinetic energy that ions experience upon collisions in a conventional collision cell of a triple quad mass spectrometer.

Based on this method an adaption to our triple quad mass spectrometer was made to evaluate the resolving power and selection possibilities. This method allowed for a time and resource saving introduction of a mobility measurement method. It avoids extensive changes to the spectrometer and avoids the need of an additional in house built analytical separation stage.

The fitting of the experimental kinetic energy distribution to a simple model based on fully elastic collisions and hard sphere models of the ions was successful. More advanced mobility models are described in chapter 4.1.

3.2 Electrospray Ionization Mass Spectrometry

Mass spectrometry (MS) has a long and diverse history as analytical tool in chemistry.[72] Many investigations in the past years have led to new ionization techniques for large and complex species to be vaporized without substantial decomposition. The most successful techniques developed so far are electrospray ionization (ESI)[73–75] and matrix assisted laser desorption (MALDI)[76] which have revolutionized the analysis of biomolecules and were awarded by the Nobel Prize in chemistry in 2002.[72, 77, 78] The successful application of electrospray to transition metal complexes which are generally not volatile, thermally unstable partly due to weakly bound ligands and thus difficult to ionize by conventional methods is another important field for soft techniques.[79] The softness of the ionization process extends the range of organometallic complexes from very simple compounds of the type $[\mathrm{ML}_n]$ (L: simple ligands like H, O, alkyl, CO, H_2)[80] to more complex "real world" catalysts used in organic synthesis.[2] Therefore electrospray ionization mass spectrometry (ESI-MS) has become the method of choice in our group gaining more and more importance in reaction screening techniques also in other groups.[2, 8]

3.2.1 Electrospray Ionization (ESI) and Desolvation Techniques

The electrospray ionization method allows the transfer of ions in solution into the gas phase under very mild conditions. It therefore is not an ionization method in the same sense as electron impact where a neutral precursor is ionized by removal of an electron. The electrospray process as dispersion of liquids by the aid of an electric field originates from the paint and coating industry. In 1968 Dole and coworkers[45] demonstrated the capability of electrospray to transfer macromolecular ions into the gas phase. Their analytical method, however, was limited by the use of a drift time spectrometer. In 1984 Fenn *et al.*[73, 74] coupled an electrospray source to a mass spectrometer and applied it to the mass spectrometry of biomolecules.[75] They realized that proteins could be electrosprayed without denaturation. Noncovalent receptor–ligand complexes and even viruses remain intact.[81]

Macromolecular biomolecules are typically electrosprayed as a series of ions with up to 30 positive charges and have to be deconvoluted to their native mass. This happens through aggregation of a different number of H^+, Li^+, and Na^+ ions from buffer salts in the electrospray solution to the polar groups in the proteins. Multiple charging allowed biomolecules to be handled within the typical *m/z* range for quadrupole mass filters. Organometallic complexes, on the other hand, are small compared to biomolecules and appear in a defined charged state (up to 2 positive or negative charges of their intrinsic charge). ESI of organometallic complexes has been reviewed in general[79], as well as in specific applications.[2] For some extremely oxidation sensitive complexes electrospray can also directly oxidize in a soft way by one or two stages. In case of neutral complexes this can enable the possibility of investigation with this technique.

Electrospray is a complicated process involving charged droplet formation, fission and field desorption. Although ESI is now in common use in biological applications, its component processes and mechanisms especially the formation of gas phase ions from the previously formed droplets are poorly understood[82, 83] (single ion in droplet theory[45, 84] or ion evaporation model[85, 86]). Both of these processes are very complex, depending strongly on an intricate interplay between variables such as flow rate, applied field, and solution properties including conductivity, surface tension, concentration, dielectric constant and viscosity, as well as the structure and conformation of

the analyte molecules. The most likely mechanism closely resembles field desorption, which also gives very "soft" ionization.

In a typical experiment, a 10^{-9} to 10^{-5} M solution of the analyte is pressed trough a capillary with a flow from 1 μl up to 1 ml per minute to a tip held at a high potential of several kV. As the solution emerges from the spray tip forming a cone, charged droplets are formed in the strongly dispersing electrical field at the tip following the field to the counter electrode which could be a high transmission mesh or could contain a transfer opening to the next stage (s. figure 3.1). In most of the commercially available ESI-MS machines the spray process is improved by application of sheath gas (mostly N_2) blowing over the spray tip. The finely dispersed droplets now need to loose the major part of the solvent being thereby reduced in size until they undergo the formation of naked gas phase ions as described before.
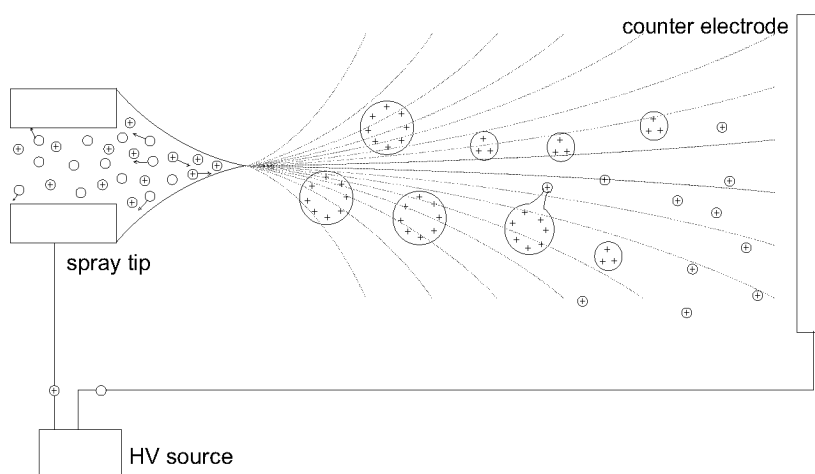
Figure 3.1: Electrospray droplet formation in the applied high field

This process is called the desolvation process and it is normally accelerated by a region of raised temperature of 100 to 300°C (*heated open room technique*) or with the *heated capillary technique* adding differential pumping beside the raised temperature of the same range. This method is mostly used in commercially available mass spectrometers also in FINNIGAN TSQ and LCQ types used in our group (figure 3.2). It can make the desolvation process even softer due to the additional expansion cooling and the reduced collisions compared to a heated open room technique but requires one additional step of differential pumping making the setup slightly more complicated.

Nanospray

A advanced technique called nanospray reduces the size of the spray tip opening diameter to several μm or even nm by fine etching techniques. This has the effect of on one hand much stronger field line dispersion which leads to the possible lowering of the spray potential to several 100V, on the other hand a possible reduction of the solvent flow to several nl per minute at the same low concentration level which decreases the necessary amount of analyte in a quite remarkable way at even higher resulting ion flow. A substantial raise in the ion yield by a factor of 10^3 for the spray process can be observed.[87] A nanospray source can easily coupled to the conventional mass spectrometers or is even commercially available.

3.2.2   Quadrupole Mass Spectrometry (QMS)

The continuous ESI source is ideally coupled to a continuously operating mass filtering device like a quadrupole mass filter as shown in a block diagram for our ESI tandem mass spectrometer of the type FINNIGAN TSQ 700 (figure 3.2). After being generated and desolvated by the heated capillary region, gas phase ions pass the differentially pumped skimmer region where they flow from several millibar pressure into high vacuum. A perpendicular field (applied with the so called tube lens) which primarily serves to guide the ions into the off axis skimmer can be used as an adjustable parameter to induce collisions with ambient gas and control the mode of fragmentation which allows to remove weakly bound ligands to generate coordinative unsaturated complexes for reactivity studies. For our ion trap spectrometers of the type FINNIGAN LCQ classic this part remains the same. After the differential pumping the mass filtering processes and additional gas phase treatment during the path through multipole ion guides can take place.
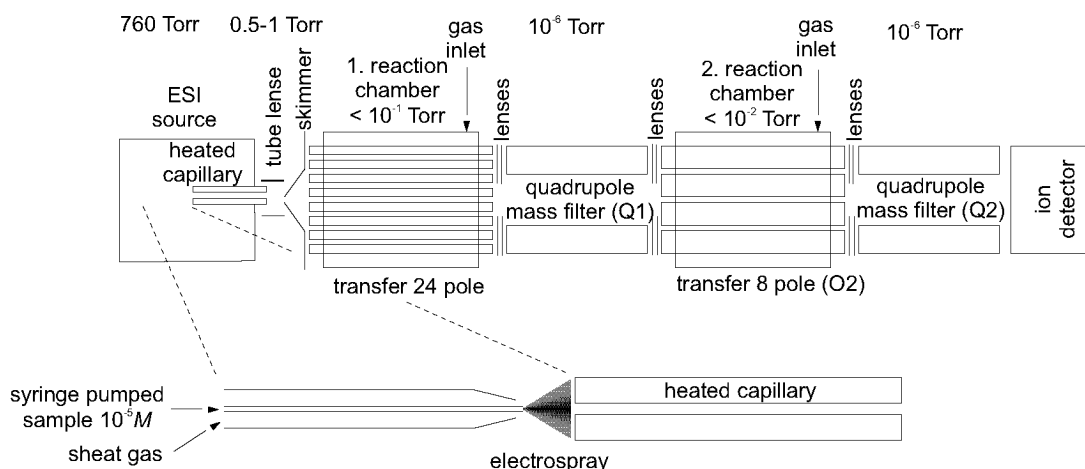
Figure 3.2: Block diagram of the modified FINNIGAN TSQ 700 ESI MS.

Generally quadrupole mass filtering works by the use of parallel application of an alternating voltage and a d. c. voltage part to two dimensionally definable quadrupole. This results in stability or instability of different mass ranges in the resulting field at different values for the two parts. In an ion trap (e.g. LCQ) ions are stored and selected under stable field conditions and then mass scanned by destabilizing part by part the masses at one edge of the stored range by changing the field conditions.

In the case of the stretched quadrupoles (e.g. TSQ) the stable field region produces transparency only for drift through of ions in the selected mass range which can be used as constant mass filter or as mass scan sweeping the field conditions. The basic functionality of quadrupole and multipole devices in a more detailed discussion can be found in the dissertation of Christian Hinderling[41].

3.2.3   Modified FINNIGAN TSQ 700 Tandem Mass Spectrometers

For our modified FINNIGAN TSQ 700 tandem mass spectrometers the remaining ion pathway is described as follows: In the high vacuum part the ions "diffuse" through the radio–frequency (RF) octapole (or 24–pole in the case of our older modified machine) where the ions are either thermalized by collisions with inert gas or reacted with reagent gas at a pressure of up to 100 mTorr. Additional information about the role and the advantages of the 24–pole can be found in section 9.2. After the first quadrupole mass filter (Q1) ions can be accelerated (-200 ... 200 eV) into the RF octapole collision cell (O2) were they can again be reacted with neutral molecules as reactant at a pressure of up to 10 mTorr. Collisions can energize ions to facilitate gas phase reactions. Under appropriate conditions, the reaction barrier can even be measured. Ions are finally detected with an electron multiplier. The tandem mass spectrometer allows four principal operational modes. a) The mass analyzer mode where either Q1 or Q2 are scanned while the other quadrupole mass filter serves in a transmission mode as an ion guide; b) The daughter ion mode where Q1 is used as a "purifying" filter to allow the transmission of ions with a specific mass over charge (m/z) ratio and Q2 is scanned to analyze the products formed by reactions of the purified ions with reaction gas in O2; c) The parent scan where Q1 is scanned while Q2 filters a specific m/z which allows to scan for a priori unknown ions which react to a known product; d) The neutral difference scan where Q1 and Q2 are scanned parallel with a specified $\Delta m/z$ to look for ions which undergo a specific change in mass.

3.3   Theoretical Model for the Measurement of Ion Mobility

An exponential dependency between the ion mobility and the loss of kinetic energy of an ion upon collision with a stationary target gas can be derived when elastic collisions between the ions and the stationary target gas molecules are assumed. Deriving a relation between the energy that is transferred in an elastic collision similar to what has been done for inelastic collisions [88] allows to calculate the ion mobility.

3.3.1   Energy Loss of a Particle Upon Elastic Collisions
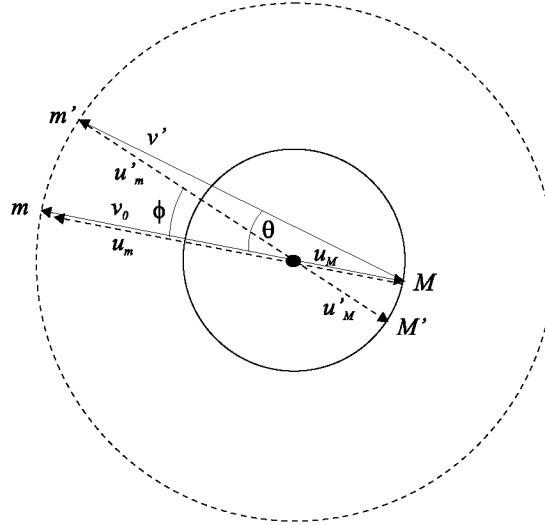
Figure 3.3: Elastic collision between an ion m and a stationary gas molecule M in laboratory and center–of–mass frame.

In the center–of–mass frame (figure 3.3), the ion m and the target gas molecule M move initially with a relative velocity $v_0 = v_m$ (stationary target gas). The center of mass velocities u_m and u_M are given by

$$v_0 = u_m + u_M \tag{3.1}$$

$$u_M = \frac{M}{m+M} v_0 \quad \text{and} \quad u_m = -\frac{m}{m+M} v_0 \tag{3.2}$$

after the collision with energy conservation

$$\frac{\frac{1}{2}mM}{m+M} v_0^2 = \frac{\frac{1}{2}mM}{m+M} v'^2 + \Delta E \tag{3.3}$$

and

$$u'_m = u_m \quad \text{and} \quad u'_M = u_M \tag{3.4}$$

where ΔE is the energy transferred to the stationary target gas. In laboratory frame, m will, after the collision, have a velocity v', at an angle $v_0 v'$ being equal to θ. The velocity of m after the collision is

$$\vec{v'} = -\vec{u}_M + \vec{u'_m} \tag{3.5}$$

$$v' = \sqrt{(u'_{mx} + u_M)^2 + u'_{my}{}^2} \tag{3.6}$$

with the relations

$$u'_{mx} = u'_m \cos \phi \tag{3.7}$$

$$u'_{my} = u'_m \sin \phi \tag{3.8}$$

where ϕ is the scattering angle in the center–of–mass frame. After substitution (and with Equation 3.4) Equation 3.6 becomes

$$v' = \sqrt{(u_m \cos \phi + u_M)^2 + (u_m \sin \phi)^2} \tag{3.9}$$

and in terms of energy

$$\Delta E = E_0 - E \tag{3.10}$$

$$\Delta E = E_0 - \frac{1}{2}m \left[(u_m \cos \phi + u_M)^2 + (u_m \sin \phi)^2 \right]. \tag{3.11}$$

For several collisions, the average scattering angle ϕ is 90° [69]:

$$\Delta E = E_0 - \frac{1}{2}m \left[u_M^2 + u_m^2 \right] \tag{3.12}$$

substituting for u_m and u_M

$$\Delta E = E_0 \left[1 - \frac{m^2 + M^2}{(m + M)^2} \right] = E_0 \left[\frac{2Mm}{(m + M)^2} \right] \tag{3.13}$$

where ΔE is the loss of kinetic energy in the laboratory frame that the ion experiences upon an average elastic collision. For t collisions the energy of the ion is given by:

$$E_t = E_0 [1 - \Delta E]^t \tag{3.14}$$

$$= E_0 \left[1 - \frac{2Mm}{(m + M)^2} \right]^t \tag{3.15}$$

3.3.2   Collision Number t

The number of collisions, the collision number t, depends on the collision cross section

$$\bar{t} = zd\Omega \tag{3.16}$$

where z is the number density of gas molecules, d is the flight path of the ions in centimeters, and Ω is the collision cross section of the ion. The exact flight path of the ions is unknown and the approximation that the flight path is independent from the pressure has to be made, which is acceptable for an RF only octapole collision cell where the ions are confined to axis of the cell. The number density z can be defined as

$$z = \frac{N_A p}{24790} \tag{3.17}$$

where 24 790 is the molar gas constant in cubic centimeters at standard temperature and pressure. Equation 3.16 and 3.17 can be substituted into Equation 3.15 and the average translational energy of an ion as it leaves the collision cell $\overline{E}_x$ is given by

$$\overline{E}_x = E_0 \left[1 - \frac{2Mm}{(m+M)^2} \right]^{\frac{N_A p d \Omega}{24790}} \tag{3.18}$$

3.4   Experiments

The principle setup for an ion mobility experiment by measurement of the loss of kinetic energy is illustrated in Scheme 3.1. Once the ions of interest are generated and mass selected in Q1, they are accelerated at a specific kinetic energy by the potential of the collision cell (O2) before they pass into the collision cell (the potential of the ions is shown in the lower part of Scheme 3.1). In O2, ions partly lose their kinetic energy due to collisions with the stationary target gas in O2. Their remaining kinetic energy is read out at the exit of the collision cell by observation of the ion current while scanning a lens potential (stopping voltage) at the exit of the collision cell independently from the acceleration voltage: ion signal will be observed as the stopping voltage is lower than the kinetic energy of the ions.

In practice, in our modified FINNIGAN TSQ 700, a diagnostic DAC scan was used which is designed to observe the ion current depending on any instrument parameter. It turned out that the ion kinetic energy was broadened by scanning either of the three
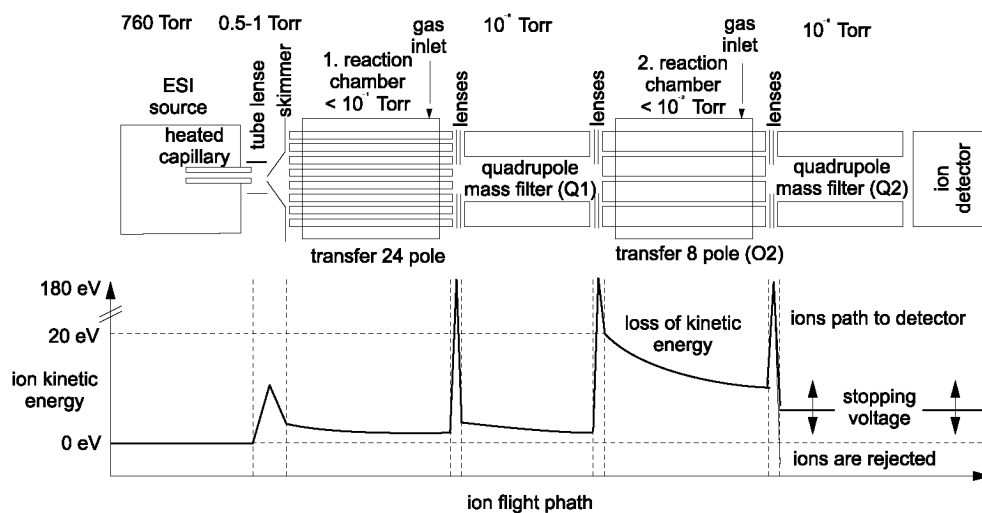
Scheme 3.1: Schematic TSQ 700 mass spectrometer. The lower part gives the ion kinetic energy. The stopping voltage is applied on Q2.

lenses (L3-1 to L3-3) at the exit of the collision cell and that scanning of the potential of Q2 was more efficient to generate sharp stopping voltages. The time delay between the detector and Q2 could be neglected as the time range of a scan was in the range of seconds while the time range between Q2 and the detector was $\ll$ 10 ms. Throughout all the experiments reported, helium was used as a stationary target gas for two reasons. Firstly better collision statistics are achieved as the loss of kinetic energy per collision is smaller for helium than for heavier target gases, and secondly the investigated ions can be prevented from undesirable collision induced dissociation.

Figure 3.4 shows a three dimensional sigmoidal fit of the ion current of chloroaniline versus the stopping voltage at different He target gas pressure. The ion current is broadened by the kinetic energy distribution of the ions after Q1 which is $\approx$ 4 eV FWHM. A plot of the inflection points in figure 3.4 against the manifold pressure for choroaniline is shown in figure 3.5 which can be fitted according to Equation 3.18. The collision cross section can be calculated from the slope of the straight line (at $p = 0$, the fit should cross through 10^0, the discrepancy can be avoided by correcting for E_0).
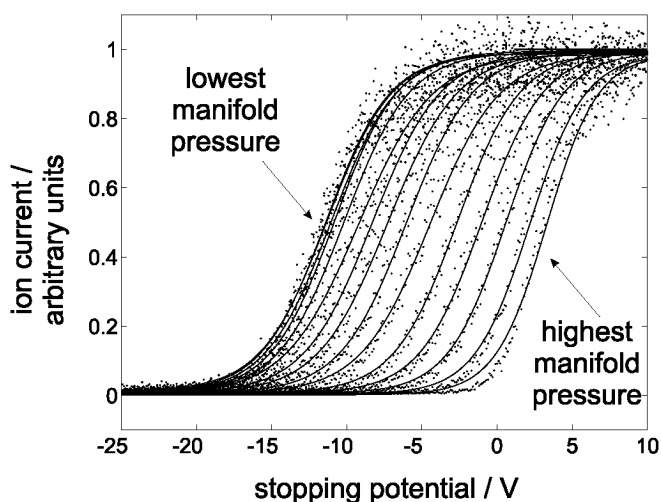
Figure 3.4: Sigmoidal fit to experimental retarding potentials at different pressure of helium in the collision cell.

3.4.1   Collision Cross Section of *p*-H–, F–, Cl–, Br–, and I–Aniline

The (uncorrected) collision cross sections for {*p*-(H,F,Cl,Br,I)–aniline-H}$^+$ are shown in Table 3.1 and compared with the ion radii obtained by Hill *et al.* [89] in a high resolution drift tube with He using a hard sphere scattering model without corrections for long range effects. The correlation of our values with Hill's values is shown in figure 3.7. Except for the value for {*p*-Br–aniline-H}$^+$, there is a good correlation between our data and Hill's data, although all values seem too be systematically to high. In principle, Hill's data can be take as the reference for corrections of the collision cross sections, because uncorrected entities may account for:

- The initial ion kinetic energy which is lower than 13.5 eV since the ions experience collisions with background gas before they enter the collision cell.

- The He gas pressure as it is read out from the hot cathode gauge.

- The ion path through the collision cell is longer than the length of the cell

There is so far no good explanation for the deviation of the {*p*-Br–aniline-H}$^+$ cross section as all species have been mass selected prior to the collision cell and therefore desolvation effects, which are a burden in drift tube spectrometry can be excluded. In Hill's experimental setup [11,90], on the other hand, the drift tube was kept at 250°C and the ions were additionally mass selected with a quadrupole mass filter after the
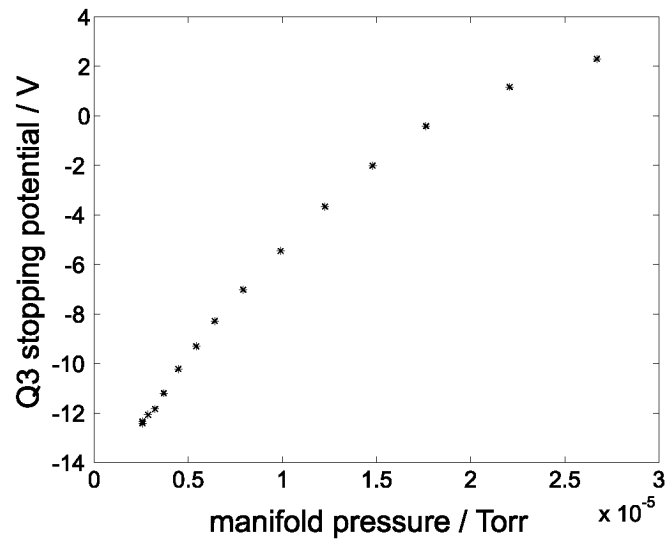
Figure 3.5: Loss of kinetic energy in CID cell depending on target gas pressure for chloroaniline with He as target gas.
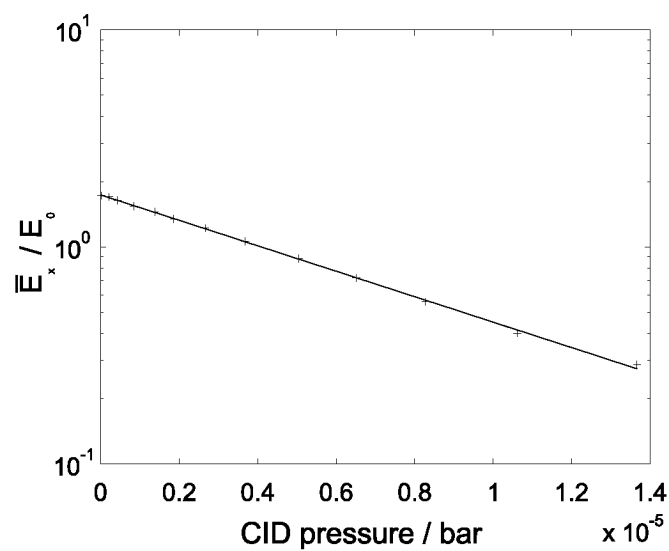

Figure 3.6: Fit of the ion kinetic energy to the model $E_t = E_0(1 - \Delta E)^t$ with $t = zd\Omega$ and $z = \frac{N_A p}{24790}$ (Equation 3.18). Ω is calculated from the slope; d is 15 cm.

R	Ω	r_{He} / Å	$r_{ion}=\sqrt{\frac{\Omega}{\pi}}-r_{He}$ / Å	Hill, [89]
H	55.06	1.03	3.16	2.38
F	59.07	1.03	3.31	2.43
Cl	72.54	1.03	3.78	2.60
Br	94.23	1.03	4.45	2.65
I	99.91	1.03	4.61	3.02

Table 3.1: Collision cross sections obtained for a distance of 15 cm, an an initial ion energy of 13.5 eV, and without corrections for the hot cathode He gas pressure.
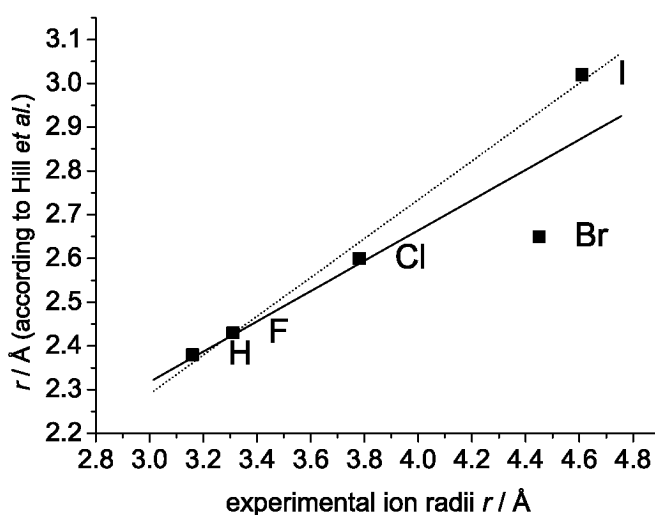
Figure 3.7: Correlation of ion radii for H–, F–, Cl–, Br–, and I–aniline obtained by Hill *et al.* with our experimental data. Solid line, linear fit Y = A + B * X A=1.279, B=0.346, and R=0.897; dashed line, Br omitted: A=0.959, B=0.444, and R=0.996.

collision cell, therefore desolvation effects can also be excluded in the reference experiments. Interestingly, when Hill *et al.* changed the stationary gas from He to more polarizable gases like Ar, N_2, and CO_2, all measured ion radii increased with polarizability and moreover, the ion radii obtained for iodoaniline were smaller than those for bromoaniline [89]. Given that polarizability accounts that much for the ion mobilities, an explanation for the increased ion radius obtained for $\{p\text{-Br–aniline-H}\}^+$ in our retarding potential experiments as compared to the ion radius from drift tube experiments may be an increased susceptibility to polarizability in the retarding potential experiment.

Figure 3.8: Loss of kinetic energy in CID cell depending on target gas pressure for {Glu-H}$^+$ and {Cs}$^+$ with He as target gas molecules.

3.5 Performance Features

3.5.1 Separation of Isobaric Ions

A further application of the measurement of collision cross sections by loss of kinetic energy is to use the collision cell (O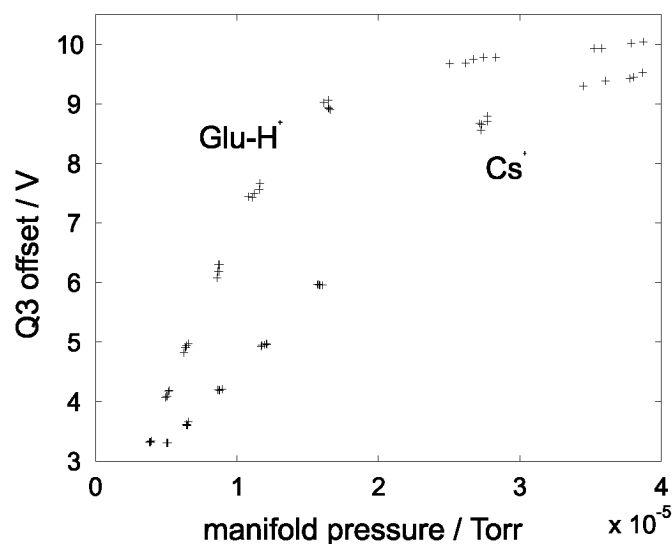2) as a separation device for ions with identical mass (isobaric ions and isomers) that cannot be separated by their m/z ratio from solution or after gas phase experiments in the 24-pol. Therefore an experiment with the two isobaric ions {Glu-H}$^+$ (protonated glutaric acid) and {Cs}$^+$, both appearing at a m/z of 133 in the MS, was made. Figure 3.8 shows the kinetic energy of the {Glu-H}$^+$ and {Cs}$^+$ ions depending on the He pressure. At $\approx 1.5 \times 10^{-5}$ Torr manifold pressure an energy discrimination of almost 3 eV between the {Glu-H}$^+$ and the {Cs}$^+$ ion can be achieved. For separation, however, either the internal energy of the ions of ≈ 4 eV (FWHM) has to be reduced to 1.5 eV, which can be achieved if the ions are thermalized in the 24–pole and Q1 is operated in RF–only mode but this would mean to surrender the mass selection capability in Q1. Alternatively the ions can be accelerated more strongly which also increases the energy discrimination proportionally. This method is limited by collision induced dissociation appearing at higher energies.

3.6 Conclusion

The measurement of the kinetic energy of ions exciting the collision cell can indeed add the dimension of structural information in mass spectrometric methods as has been demonstrated here for different anilines or for the conformation of biopolymers [69]. The measurements can be performed in commercially available triple quad mass spectrometers and thanks to the MS/IMS/(MS) setup which has also been reported recently for conventional drift tube IMS [49–52,91]. Obtained collision cross sections can be attributed unambiguously to the species of interest rather than to any solvation adducts.

Even with the shown well agreeing fits and multiple pressure measurements the resolution power of this low pressure method was not high enough for our requirements. The method can be used only in a small application field concerning our groups gas phase chemistry projects. For the planned separation of different conformers of catalysts or catalysis products the method does not give sufficient resolution and is therefore not suitable.

Chapter 4

Construction of a High Pressure Ion Mobility Cell (Drift Tube) Fitting to a Conventional FINNIGAN TSQ 700 Mass Spectrometer

Summary

In this chapter the development and deployment of a compact high pressure high field drift tube for mobility measurements fitting to the inlet of a standard FINNIGAN TSQ 700 is described. Its goal is to include structural information at a high resolution level into MS gas phase experiments.

4.1 Technical Introduction

Based on the results of chapter 3, the construction of a high pressure high field drift tube with high resolution for mobility measurements fitting to the inlet of a standard FINNIGAN TSQ 700 became the main project of this thesis. Calculation models, resolution requirements, simulation of internal electrical fields and technical issues are discussed as well as first test measurements.

4.1.1 Calculation Methods for Collisional Cross Sections

One of the most desirable features of the high pressure limit mobility measurements with constant field is the possible modelling of the drift behavior and the corresponding collision cross section with the drift gas through the collision integral Ω.[92] A huge number of models for these cross sections were published in the last 40 years which use different complexity of the collision modelling.

Depending on the chosen drift gas type or mixture and its ability to have non trivial interactions with the molecule surface of the ions of interest, the the accuracy and suitability of the described models differ. For example the interactions of a nitrogen binding complex with the drift gas will need a different level of theory to be described with nitrogen as collision gas than with an inert gas like helium. Holding this in mind it seems to be important to choose carefully the calculation model for the investigated system and, if possible, to calculate the cross sections with more than one model to evaluate the quality and agreement of the models. The somehow remarkable differences between the descriptions can be seen in figure 4.2.

The simplest approach is by a exact hard sphere models using Van der Waals radii or other suitable atomic radii to describe the drifting ion. As every model it can be modeled as simulation with a large number of classical trajectories[93, 94] to achieve statistical relevance. But the advantage of this model is the possibility to describe it in a defined way by integrations.

The Bower's Projection Approximation (PA) Model[95-98]

The Bower's projection approximation (PA) model is one of the most commonly used methods of the exact hard sphere model types. The ion is modeled by a collection of overlapping hard spheres with radii equal to hard sphere collision distances. The collision cross section is defined by an integral over the cross sections of the sphere model in all possible room directions implying an accurately calculated structure.

An orientationally-averaged geometric cross section can be determined by averaging the geometric cross section over all possible collision geometries when a molecular dynamics (MD) run on the structure is performed. This model can give fast and quite accurate results for the cross sections of simply describable molecules models if the structure can be calculated in a trustable way.

Exact Hard–Spheres Scattering (EHSS) Model[99]

Another hard sphere approach is the exact hard–spheres scattering model (EHSS) using 100% elastic collisions as described in chapter 3. The ion is modeled by a collection of overlapping hard spheres with radii equal to hard sphere collision distances (as in the PA-model mentioned before). The orientationally-averaged momentum transfer cross section is calculated by determining the scattering angles between the incoming buffer gas atom trajectory and the departing buffer gas atom trajectory on the hard sphere model surface.

If additional surface effects with the drift gas are present, the EHSS and the Bowers PA model have to be corrected by more complex models. Especially for highly reactive ions or ions with strongly inhomogeneous charge distribution, the additional interactions produced by these effects are important.

The Trajectory Method (TM)[93, 94]

Beside the integration methods and classical trajectories, the numerically more expensive trajectory method (TM) is used as another important approach. The most commonly used TM calculations treat the ion as a collection of atoms, each one represented by a 12-6-4 (force field) potential proposed by Mason and Schamp [100]. This potential contains an adjustable force parameter γ ranging from 1 to 0 according to

how dominant the role of the charge-induced dipole interaction in the collision is. A typical form of the 12-6-4 potential for one atom is shown in figure 4.1.
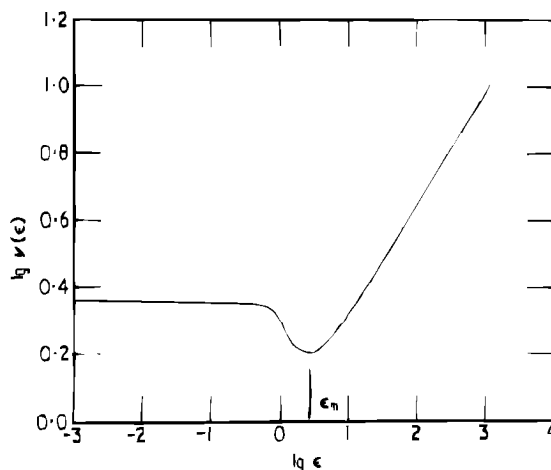

Figure 4.1: A typical interaction potential is the 12-6-4 potential.[101]

The effective potential is obtained by summing over the individual atomic contributions and then trajectories are run in this potential to obtain the scattering angle (the angle between the incoming and departing buffer gas atom trajectory). Due to the used potential, this method takes additionally more care of gas-ion interaction effects due to inhomogeneous charge distributions, but consumes quite reasonable computation times using a statistically reasonable number of trajectories (eg. several 100'000 to 10'000'000). In almost all of the cases (if no reaction with the drift gas takes place), this method describes the collisions in a sufficient way to model accurate drift times.

Scattering on Electron Density Isosurfaces (SEDI)[102]

Advancing the electron density treatment, a method called scattering on electron density isosurfaces (SEDI) was developed in Jarrold's group.[102] Taking the general fact that molecular electronic orbitals have irregular shapes, a surface of equal electron density has to be defined numerically as a set of points in space. This can be performed in different levels of theory starting at an EHSS like model. The points comprising a surface are located on a three-dimensional grid of variable periodicity while the quality of the treatment is strongly dependent on its fineness.[102] To include more advanced interactions all possible calculation methods for the isosurface like MNDO, DFT, MP2 or even higher methods can be taken. The standard SEDI is calculating the collision cross

sections by collision integrals. The most important difference is, that SEDI also can include inhomogeneous repulsive interactions and molecule orbital mixing effects. In the basic form still no attractive interactions can be included. Figure 4.2 shows clearly the differences of hard sphere and SEDI surface descriptions of a C_{18} ring cation, where the hard sphere models often describe the collision cross sections too large.
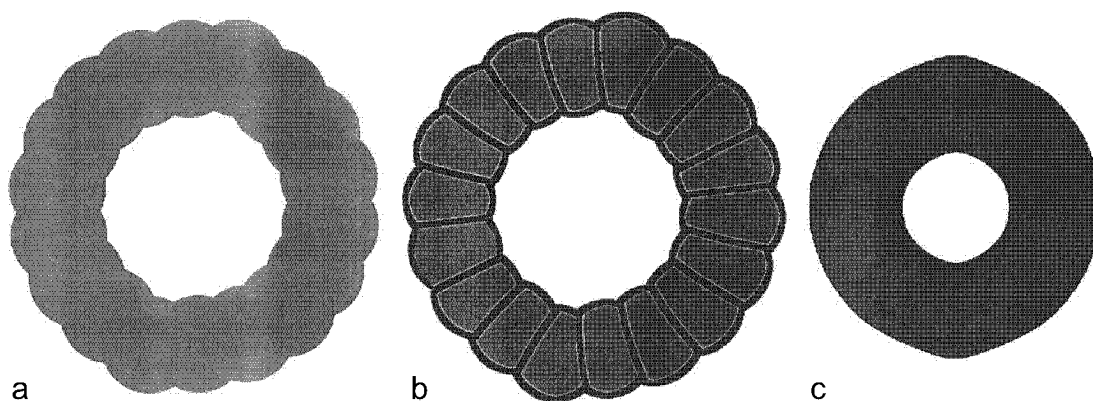

a   b   c

Figure 4.2: Representations of a C_{18} ring cation by
a: Projection approximation (PA),
b: Exact hard-spheres scattering (EHSS) and
c: Scattering on electron density isosurfaces (SEDI). [103]

Isodensity Trajectory Hybride Methods (SEDI-TC)[102]

With the described trajectory method, scattering trajectories on any electron density isosurface instead of the summed atomic force field can be performed. This leads to the possibility to mix the SEDI and TM methods to the powerful SEDI trajectory calculation hybrid method (SEDI-TC). Like in SEDI, advanced descriptions of the molecule orbitals can be chosen, but due to the needed calculation power the use of these methods is not preferred if not highly necessary for the investigated collision systems.

All the trajectory methods can partly cover more interactions than the limited integration methods. This leads to a closer description of the measured cross sections. The SEDI-TC has a better description for small and irregular molecules than TM while for larger molecules the results start to approach each other. [103] This fact seems to get important in terms of feasibility of the corresponding calculations to evaluate measured

data for larger molecules as peptides or other biomolecules[11,51]

Some real complicated systems can only be well described by full reaction surface calculations with quite expensive computational methods which is still not suitable at the moment.

Mobcal - A Program to Calculate Mobilities[94,99,104]

Mobcal is a program which includes the three most basic calculation methods EHSS, Bowers PA and TM mentioned before. It was developed in Jarrold's Group[94,99,104] and can be downloaded as source code or Windows executable at their web page free of charge. The code for it is written in FORTRAN 77 in a well understandable and changeable way, including a documentation for the important parameters.

It uses a start file where the input and output file name beside a random number seed are specified and an input file which contains the number of atoms, coordinate units, charge distribution, a scaling factor (usually 1.0000) and a single coordinate set or a series of coordinate sets from a MD run.

In the program code some important additional parameters are commented to be changed before compilation. The default and predefined atom types are H, C, N, O, Na+, Si, S and Fe. To use other elements, a block of own parameters can be defined. Beside this, at a commented place the number of TM and EHSS trajectories can be set.

For most of this projects subsequent mobility calculations this program was used.

4.1.2   Desired Features and Requirements

The project environment, the gas phase experiment types in our group and other experimental project ideas for our mobility drift cell give the following requirements for the selected ion mobility method:

- **The resolution power has to be in the range of several %.**
  Most gas phase experiments carried out in our group, especially those for reaction mechanism investigations are made on organometallic complexes which allow in most of the cases a large number of different reasonable conformations to be assumed. Most of this conformations are expected to have only several %

of difference in collision cross section. The ability to distinguish by small differences for the detection of cis/trans or branching ratios or structural differences of complexes as well as to try separation of enantiomers by gaseous additives requires the same range of high resolution.

- **The machine has to be built with an interface to be coupled to a standard FINNIGAN TSQ 700 and / or FINNIGAN LCQ classic.**
  To be suitable for our experiments, an ion mobility selection step has to have the ability to be directly coupled to our FINNIGAN TSQ and/or LCQ quadrupole mass spectrometers. Especially for advanced gas phase experiments it has to be coupled to one of our modified FINNIGAN TSQ 700 mass spectrometers.

- **The measurement should be only time dependent on a slow milisecond time scale or time independent.**
  Quadrupole mass spectrometry is known to be a more or less slow MS method (ms range). Also if the detection is at a constant mass most of the multiple step machines will have several milliseconds of signal decay.

- **Electrospray is the source of choice.**
  Most of our investigated systems are weakly bound complexes which need a real soft ionization method. Some are air water and acid sensitive. Currently is the handling knowledge for such compounds in our group most advanced in electrospray.

- **The measurement should give a result which is cross section dependent in a more or less trivial relation to have the possibility to make structural assignments by mobility calculations.**
  Due to the planned observation of not completely structurally known systems, the calculation of cross sections on mostly calculated structures seems to be the only suitable route to perform assignments to the measured cross sections.

4.1.3 Available Mobility Measurement Modes and Techniques

Limiting the ion mobility measurement setup to high pressure high field methods a field has to be applied to the drift cell and the measurement of the cross section dependent parameter has to be carried out by either timing devices, a pulsed source measuring drift times or by the asymmetric waveform method mentioned in section 2.3 which will not be selected due to the requirements concerning mobility calculations discussed in section 4.1.2. The experiment will be carried out in the high pressure limit where all ion movements due to the current kinetic energy including thermal movements will be stopped by multiple collisions within a short range. Applying a uniform field an assumption that the initial kinetic energy E_0 is negliable and the local acceleration by the electrical field is in equilibrium with the retardation by collisions can be used. This formulates a field dependent constant drift velocity where K is the ion mobility, which depends from the collision integral Ω and the electrical field strength E.[57,92]

$$\nu_d = KE \quad \text{and} \quad t_d = K\frac{l}{E} \tag{4.1}$$

The ion mobility K can be formulated out of Ω as follows in equation 4.2, where N is the density of the uncharged drift gas in molecules per cm^3, z the charge of the ion, e the unit charge, M the mass of the ion, m the mass of the neutral drift gas molecule and T the absolute temperature in K.[92]

$$K = \frac{3ze}{16N}\left[\frac{1}{m} + \frac{1}{M}\right]^{1/2}\left(\frac{2\pi}{kT}\right)^{1/2}\frac{1}{\Omega} \tag{4.2}$$

In literature sometimes the reduced mobility K_0, the normed mobility to 273 K (T_0) and 1 bar (p_0), is mentioned which results from equation 4.2 and was published[92] with taking care of the temperature dependent N as:

$$K_0 = K\frac{p}{p_0}\frac{T_0}{T} \tag{4.3}$$

Timing Methods

Choosing electrospray as constant ion source, the pulsed source method will require a field pulsing method or ion collection by an ion trap before the mobility region like the setup used in Clemmer's group that is shown in figure 4.3.[9,10,12,56] This setup would

allow pressures in the millibar range and would additionally enable the possibility to shift the whole base potential of the drift tube during the measurement due to the trapped ions. Storing the ions would result in close to 100% ion transmission for the experiment in time resolved detection. Furthermore, this would allow an increase in number density which is advantageous for weak sources.
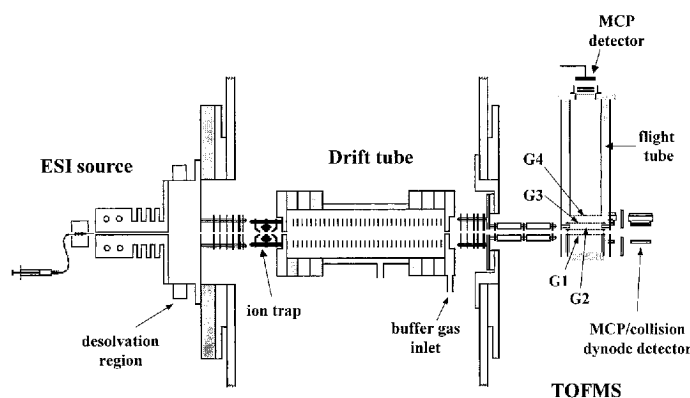

Figure 4.3: An IMS setup with precoupled ion trap and ESI source as used in Clemmer's group[10].

Timing by Additional Timing Devices - Ion Gates

For methods with additional timing devices within the drift region, any coupled gas phase technique before or after the IMS cell would be possible. These devices have to stop or trap the ions completely which is usually done by a three or more times stronger field orthogonal to the drift field. Several techniques with fine grids, alternated fine wires, stacked ion lenses or mechanical shutters have been published.[11,105,106] The most commonly used gate type is the *Bradbury-Nielsen type gate*[107] which is built with fine wires in a plane connected to alternating potentials (+/-/+/-/+/-/...) applying a quite high closing field at low potentials due to the small distance between the wires (> 1 kV/cm at 40–100 V). Using these timing devices, different measuring modes with one or two gates are described in literature. At the entry of the drift region in some setups a nontimed part is present to flatten out the field in the timed region and to force the ions into a more uniform flow.

In the following part the most common gate pulsing methods are described, illustrated by the gate functions and artificial resulting spectra:

One Gate Pulse Method[11,108]

The simplest timing method with ion gates within the drift region uses only one gate at the entry of the timed part of the drift region. It is usually held closed opening only for a time short pulse of 0.1 to 2 ms depending on the desired resolution and signal intensity requirements. This results in an ion pulse which separates into different ion packages due to collisions at the different cross sections arriving at different retention or drift times t_d relative to the pulse zero time. If a fast detection is present, a time dependent ion mobility spectrum can be acquired directly as shown in scheme 4.1. For this method a time dependent detection is mandatory.
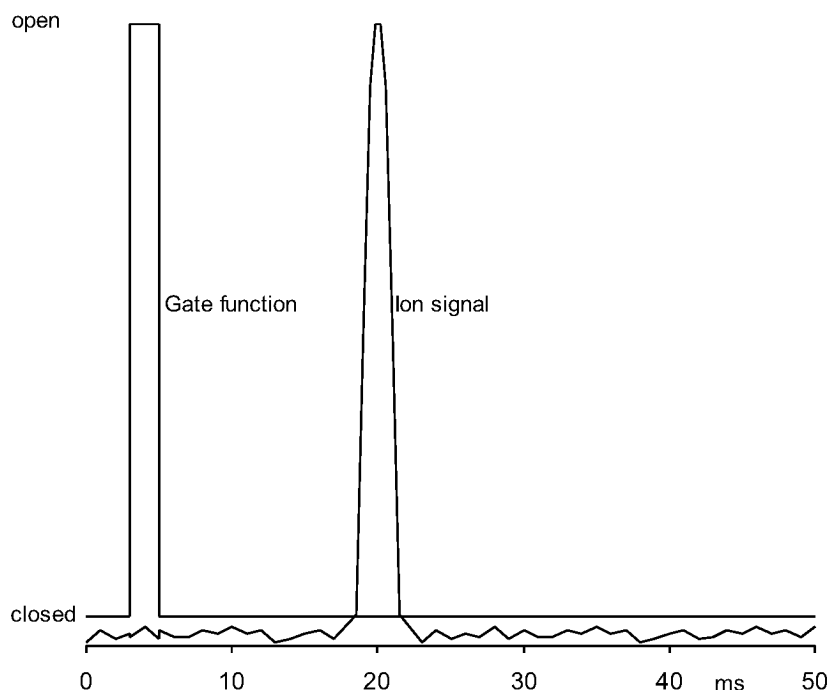

Scheme 4.1: The one gate pulse method used in most setups.

The ion transmission for this type of experiment and the detected ion signal depends on the opening time and the resulting gate function integral versus the maximal drift time of the observed ions which is the total transmission integral. This is only in the 10^{-3} to $5 \cdot 10^{-2}$ part range for the high resolution case, but the experiment can be averaged by repeatedly pulsing the gates to gain better signal to noise ratio (S/N). The total duration of one measurement is the maximal drift time of the ions which is usually in the 30 to 100 ms range.

Two Gate Mobility Cutout Sweep Method[108]

To avoid the requirement of a time dependent detection a second gate can be used at the exit of the drift tube. It adds the capability to cut out desired drift times. This allows to produce pulses of cross section selected ions. To measure a mobility spectrum the timing difference between the two gates can be sweeped. The pulse forms and widths are chosen similar to the one gate method as shown in scheme 4.2. Usually the two opening durations are identical.
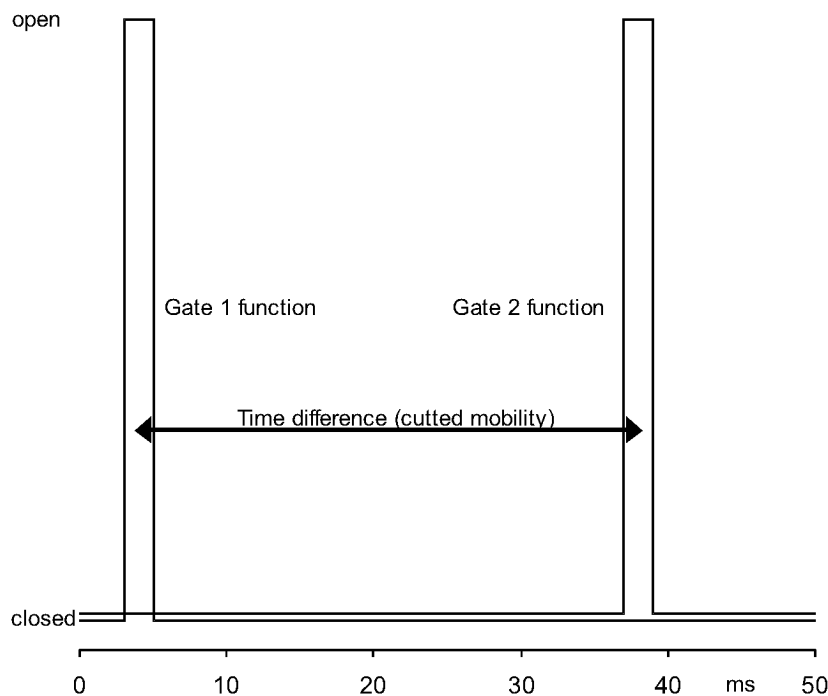

Scheme 4.2: The two gate mobility cutout sweep method.

The total transmission function is the convolution of the two gate functions which in the case of two narrow rectangular functions is a triangular function of the same base width. This divides the transmission for the ions at the selected drift time by another factor of 2. The total transmission for all ions is even smaller, divided again by the quotient of the total transmission and the gate function integral which ends up in the 10^{-6} to 10^{-4} part range. Nevertheless the detected ion signal intensity per recorded data point remains at the same level. Averaging to gain better S/N ratios can be done by simply slower sweeping of the time difference. The duration of an experiment is the maximal ion drift time per data point which is substantially longer than the one gate

method and ends up in the 10 to 100 s range depending on the number of recorded points.

Two Gate Fourier Transform (FT) Method[108]

In the 80's a new and more advanced two gate method was published[108]. Instead of the short opening pulses for the two gates a regular square wave was applied synchronously on both gates. Depending on their cross section, the drift time of the ions is in or out of resonance with the square waves producing an interference weighted signal.
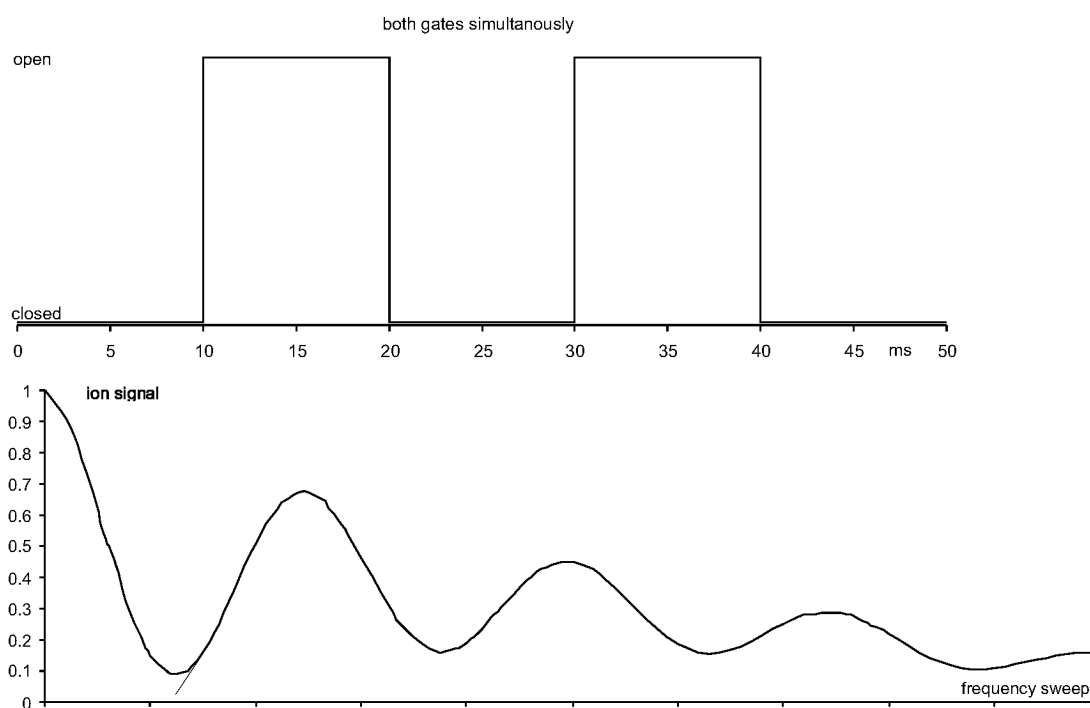
Scheme 4.3: The two gate fourier transform method.

The convolution function of the two gate functions can be described as a regular sawtooth function at the given frequency of the gate function square wave. The sawtooth function can be described itself by a sinus wave with a defined series of overtones. Sweeping different frequencies, the folding of the time dependent spectrum (equal to the one gate method spectrum) with this function is in this case close to a

inverse fourier transformation which ends up in a interference spectrum in the form of a FID (free induction decay) shown in figure 4.3. The forward fourier transformation (FT) of the recorded signal results again in the drift time spectrum showed in figure 4.4.
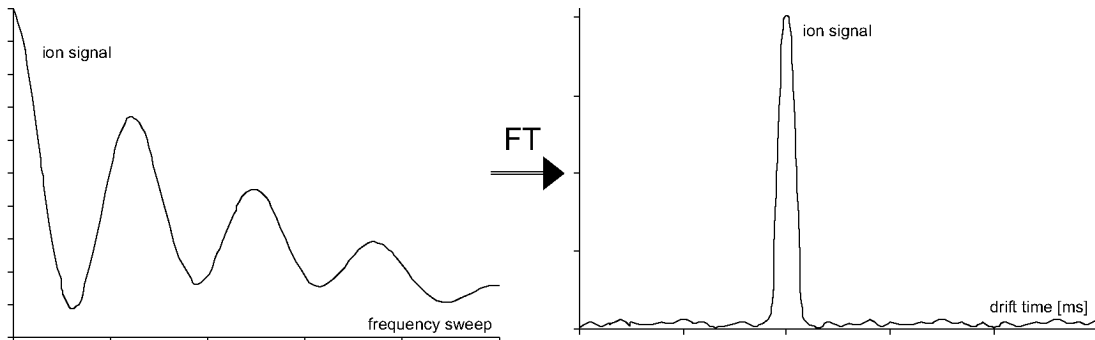
Scheme 4.4: Fourier transformation to the mobility spectrum.

The resulting difference between a convolution with a sawtooth function compared to a sinus function in the experiment is a slightly different envelope of the FID which produces primarily a slightly different mobility peak form (s. section 4.2.2). It can be partly corrected by mathematical treatment of the FID. Another obvious fact is, that the frequency and time domain are exchanged compared to usual fourier transform methods which doesn't change the mathematical relations at all. Half of the inverse of the smallest frequency gives the maximal drift time of the ions. Having ions with longer drift times present results in backfolding mirroring at the maximum drift time like the maximum frequency effect in NMR.

The total time needed for the experiment is again at least the maximal drift time per data point like in the two gate mobility cutout method, but the most important difference compared to the other methods is the ion signal transmission of near 50% which is far more than for the "classical" one and two gate methods. Averaging can be done in fact by acquiring longer on one data point or by averaging of multiple FID "shots".

4.2   Evaluation of the Different Technical Setups

In this section the evaluation and selection of the geometrical setup and the desolvation technique as well as the mobility measurement techniques and methods best fitting our requirements and machine environment are discussed.

4.2.1   Evaluation of the Different Methods for the given Environment and Requirements

The most important advantages and disadvantages especially those concerning our QMS setups are collected below in table 4.1.

Method	Advantages	Disadvantages	Avail. for ESI-QMS
Pulsed source	fast high transmission	time dependent source dependent[1]	mass filter only
Ion trap source	fast ion accumulation high transmission	time dependent complicated to build	mass filter only
One gate method	fast easy to build[2]	time dependent medium transmission	mass filter only
Two gate method	time independent easy to build[2]	slow low transmission	all modes
Fourier method	time independent high transmission easy to build[2]	slow advanced data handling	all modes

Table 4.1: Measurement method evaluation table
1: The complexity to build is source dependent
2: Depending on the gate and drift region design

Since high pressure mobility measurement setups are known to be not highly effective in terms of the total ion transmission through the drift region due to expansion by collisions with the drift gas and collection of the ions approaching the walls[11], total transmission of the timing method is a main selection issue. Beside this, an ion trap as collection unit and the pulsed source setup for ESI are both quite complicated to build but could probably added in the future.

The building of two timing devices (an entry and exit gate) is mandatory for the *fourier transform measurement setup* which fulfills both requirements of high ion transmission and time independency. The usability of the simple *one gate pulse method* on our mass spectrometers should also be tested with the final device. To simplify the construction for the desolvation region of the high field high pressure drift tube, the *open room technique* (discussed in section 3.2.1) was selected with about one third of the length of the whole drift region before the first timing device.

Taking one bar as drift pressure and minimizing the size of the additional devices, a modular drift tube was designed which fits to the entry of FINNIGAN TSQ 700 and LCQ. This guarantees modularity and moveability of the device to be able to profit from all the advantages of the differently modified machines in our group.

4.2.2 Mathematical Evaluation of the Sawtooth Transformation and S/N Capabilities of the Chosen Setup

To visualize the differences of the transformations with the real gate functions of the *two gate fourier transform method* and to evaluate the S/N capabilities of the FT method and thus the detection ability of low intensity signals a simulation with Math-CAD 2001i[109] was performed.

An artificial spectrum containing three peaks was generated using the gaussian peak described in equation 4.4 with t = time [s], m = peak position [s], w = peak width [s] and h = peak integral. For the calculation 2048 data points were simulated, using the peak parameters shown in table 4.2.

$$peak_i(t, m_i, w_i, h_i) = h \cdot \frac{1}{\sqrt{2\pi}w} \cdot e^{-\frac{(t-m)^2}{2w^2}} \qquad (4.4)$$

i	1	2	3
m	0.010	0.030	0.063
w	0.00025	0.0004	0.0008
h	1	1	1

Table 4.2: Parameters of the calculated peaks

Summing up the three resulting peak functions results in the original IMS spectrum shown in figure 4.4. The subsequent calculations all start from this original spectrum.
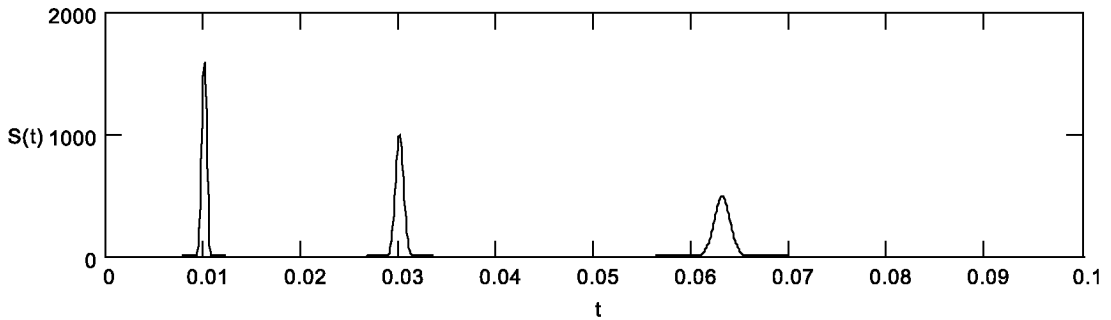

Figure 4.4: Calculated original IMS spectrum. t: time [s]

For the visualization of the differences between convolution with sawtooth gate functions compared to an inverse (fast) fourier transformation (IFFT)[1], the total peak function was convoluted with sawtooth functions using the same frequencies as for the sinus waves used in the IFFT. The resulting FID's are shown in figure 4.5 (normalized).
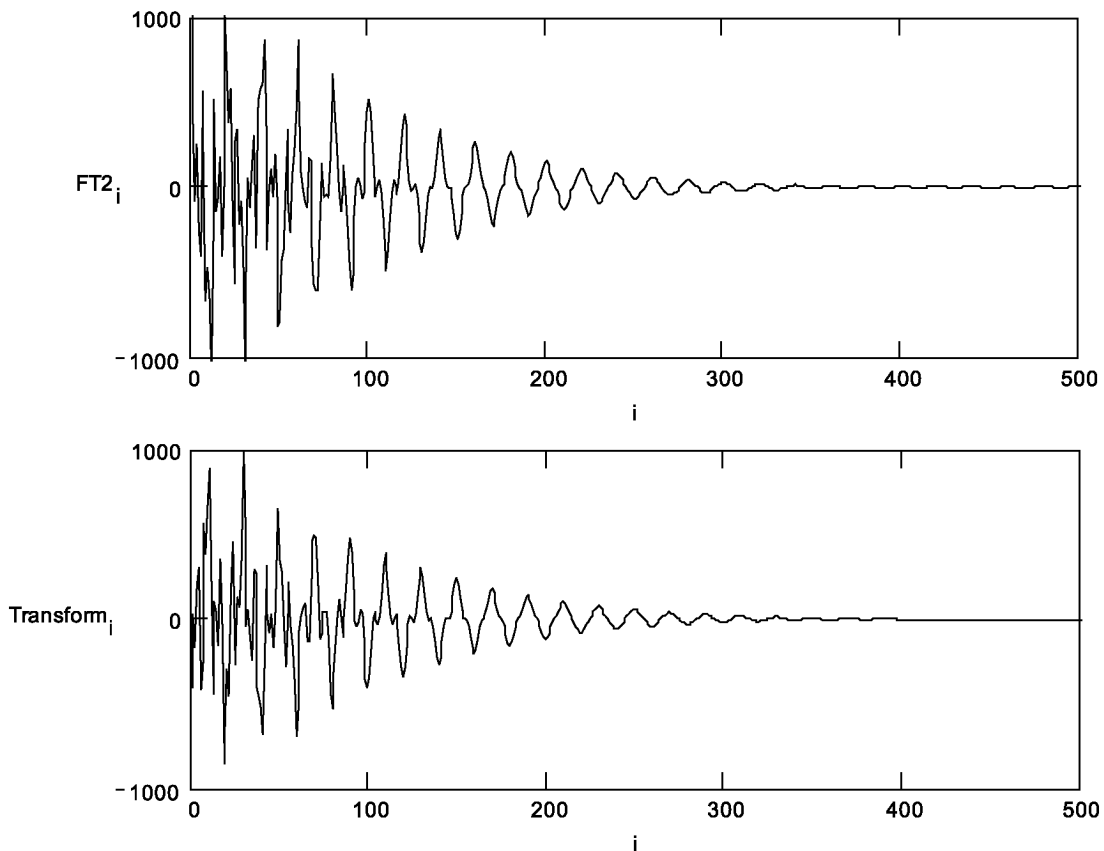

Figure 4.5: Resulting FID's in the frequency domain. x: frequency [points] upper: IFFT, lower: sawtooth transformation

Only a small difference in the envelope of the resulting FID function is visible as discussed in section 4.1.3. An FFT of the sawtooth transformed original spectrum results in lorentz like peak forms that differ especially at the base from the original gaussian-like peaks (upper spectrum in figure 4.6).

Using only half of the sampling points in the FID stage (frequency domain) results in a Nyquist effect[110] mirroring the drift times higher than the half inverse frequency

---

[1]IFFT: Discrete (digital) fast fourier transformation algorithm[110] used in many programs as MathCAD[109] and MATLAB[111]

sampling step at this line (well visible in figure 4.6). A change of the sampling step will also change the mirroring line and shifts the artefact peaks altered through this effect. Therefore a test measurement at different sampling steps could discover such artefact peaks.
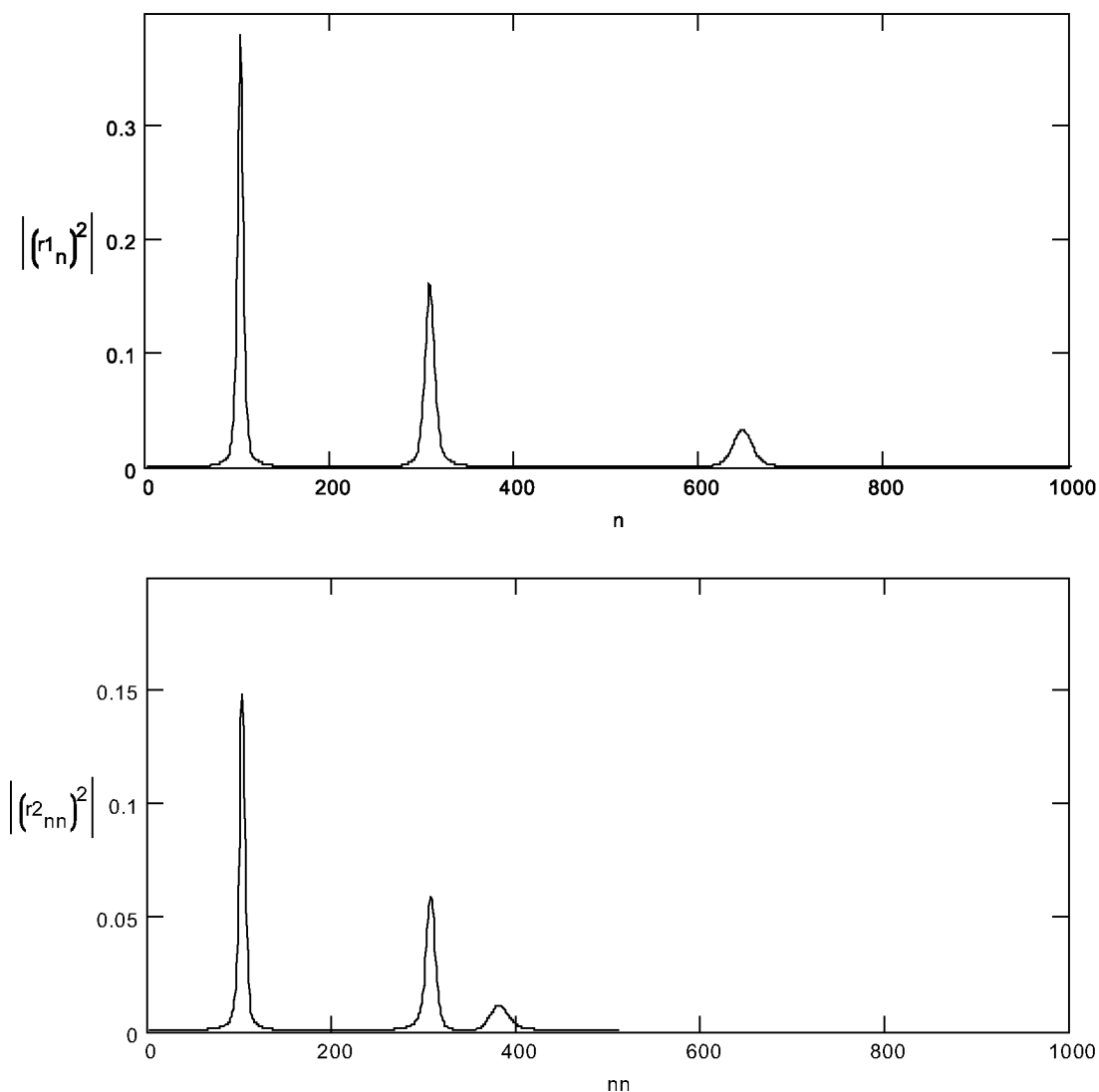

Figure 4.6: Nyquist[110] effect: IMS spectrum after the FFT using all (upper) and half (lower) of the sampling points. x: time [points]

Because of the quite low total ion transmission of all high pressure mobility measurement setups quite low signal intensities for the ions of interest are expected. Therefore the robustness of the peak detection against high background noise is important.

To simulate the behavior and capabilities of the FT method a simulation with artificial noise using white noise of 0, 20 and 40% of the maximal intensity was added to the FID signal before the FFT transformation. The resulting spectra after the FFT are shown in figure 4.7. Also at the 40% noise level the peak positions are still detectable just reaching the limit of the method for the broadest peak of the series.

Conclusion

The MathCAD simulations clearly showed the slight differences in the detected mobility peak forms of the sawtooth transformation of the *two gate fourier transform method* in comparison to the time dependent detection which is less important than the transmission amelioration.

The Nyquist effects can be detected and beaten easily by just making test measurements at different sampling steps resulting in a shift of the altered peaks by this artefact.

The S/N test shows powerful robustness of the fourier transform method against even strong noise. Averaging n series of the measured data will lower the noise by the usual factor of $\sqrt{n}$ which can be easily done at different stages of the measurement.
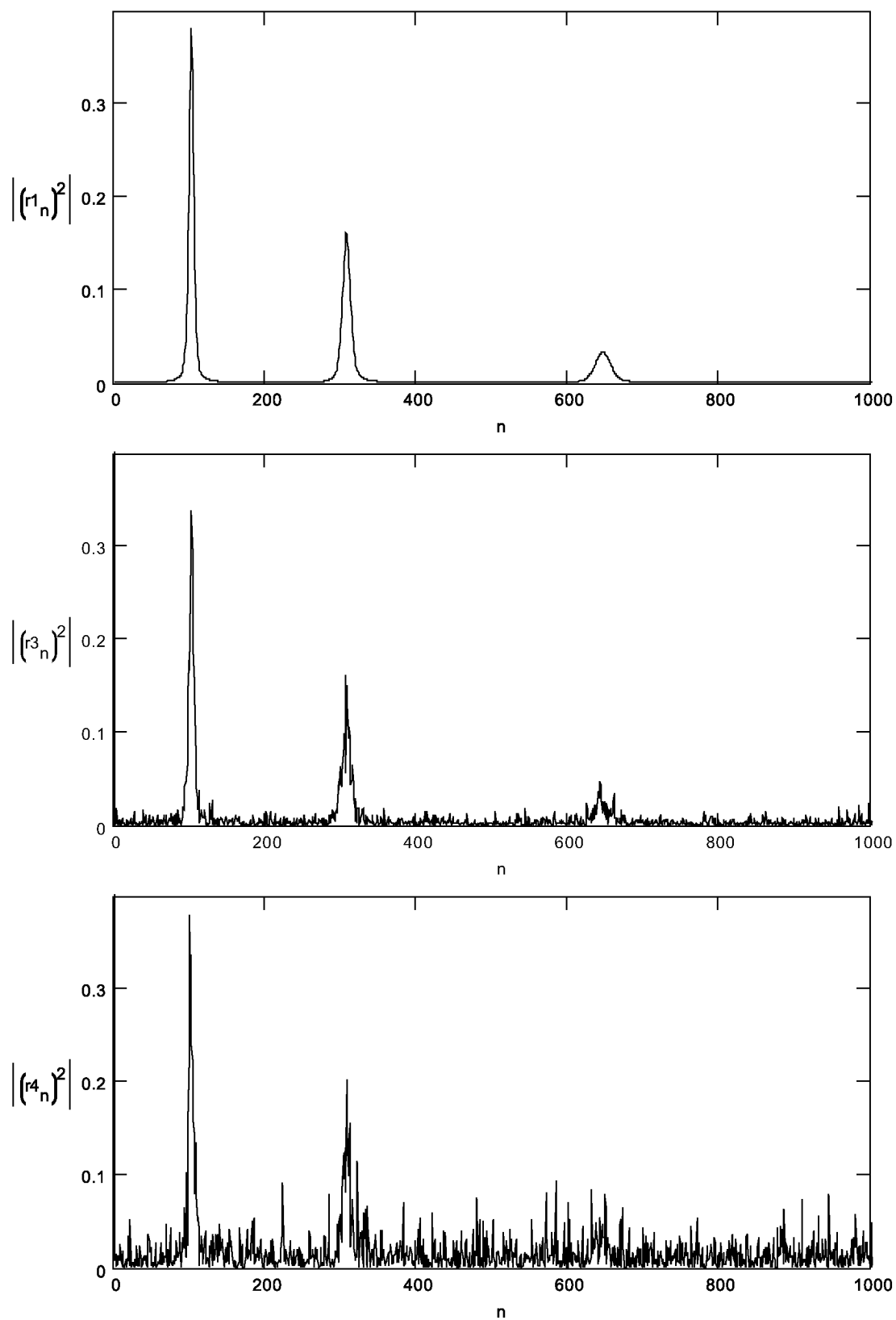
Figure 4.7: S/N effects: IMS spectrum after FFT adding artificial noise
at the FID stage. upper: 0%, middle: 20%, lower: 40%,
x: time [points]

4.2.3   Simulations and Geometrical Details

For the evaluation of the geometrical construction details of the drift tube simulations with SIMION 6.0[112] on the full setup (including the interface at the exit of the tube) were made. The most important points of interest were the uniformity of the field in the timed region (between the two gates) and focusing/defocusing effects at the exit.

The uniform field is typically achieved by connecting a series of evenly spaced rings (separated by a nonconducting material) with equal value resistors. The tube design was planned similar to the one used in Hills group[11]. The strong field of up to 300 V/cm along the main drift region was planned to be applied with a stack of 21 (8 desolvation region + 12 timed region + 1 exit region) alumina rings altering with PEEK (Poly Ether Ether Ketone) rings as insulators with a stack distance of 1 cm.
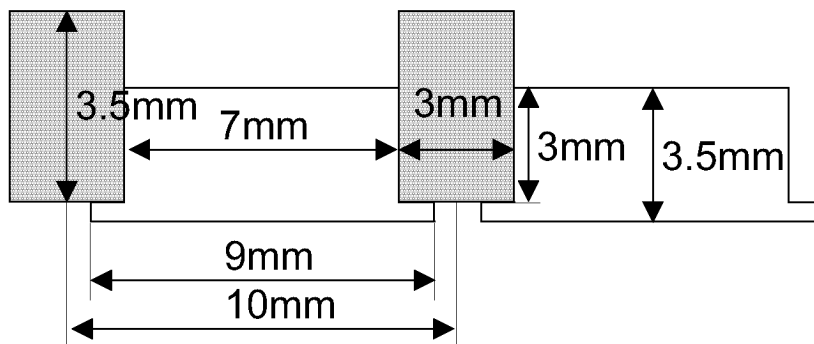
Scheme 4.5: Profiles of the stacked PEEK and aluminium rings.

After literature study of different setups focusing on field, ion collection effects and construction stability an inverse t profile for the alumina ring with a small interleave to the PEEK rings was chosen. The exact profile and dimensions of the peak and alumina rings are shown in scheme 4.5. The inner diameter of the alumina rings was set to 49 mm, the outer diameter to 60 mm. The full drift tube was simulated cylindrical symmetric with a simplified ring profile (insulator stack form neglected). Therefore only two dimensions are shown in the output graphics.

The simulation in the middle of the timed region of the drift tube near the wall gave a quite flat form of the field. Only close to the wall does a visible distortion take place (s. figure 4.8). Most ions drifting within the first half of an alumina ring in the distorted region will be collected by the wall due to the field lines which will result in a small signal decrease. In the second half of the ring electrode a small distortion

of the drift path is possible. The section of remarkable distortion is small compared to the section of the whole drift region but it is probably one of the important sources of the final peak width in high field drift tubes beside the thermal broadening. Hill *et al.* recently published a solution to that issue with a new ring profile containing an additional collector plate part pointing into the drift region[113]. The price to pay for the better resolution is another decrease of the total transmission by more than the ratio of the additionally covered section to the complete drift section gaining several percent of resolution.
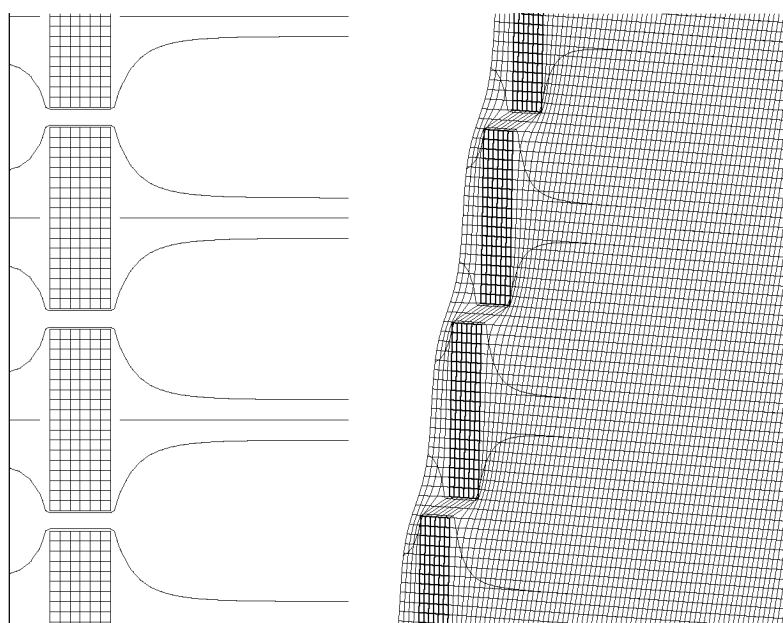

Figure 4.8: Field simulation near the ring electrodes.
right: potential lines, left: field grid and potential lines

For the primary setup it was planned to build two Bradbury-Nielsen type gates in between of the aluminium rings which behave in the transparent mode like a grid on the given potential. Setting it to the average of the two bracketing potentials it should flatten out the field. The gates in transparent mode were approximated in the simulation as simple points in the two dimensional picture.

At the exit of the tube two detection plate rings in plane with the heated capillary entry were planned offering additional detection possibility and also partly flattening out the exit field. Between the exit gate and this plate only one ring electrode was planned. In the simulation of the exit potentials in figure 4.9 important distortions also

coming partly through the exit gate into the timed region were discovered. This could affect the resolution in a significant way.
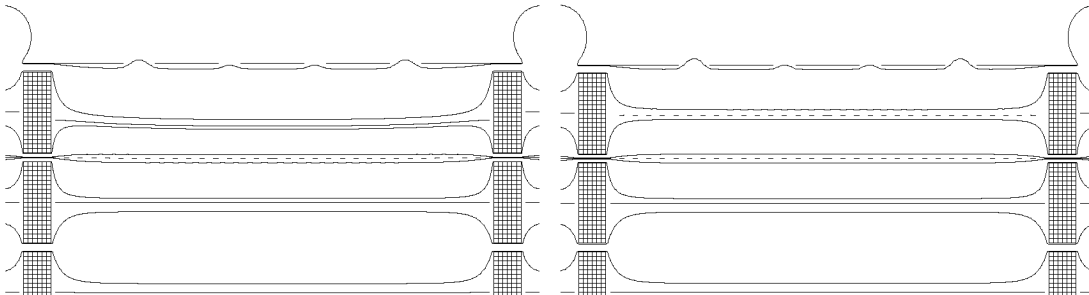

Figure 4.9: Exit of the drift tube with and without additional grid.

As solution for this problem the idea of a fine grid with high transmission exactly in the middle of the last ring electrode on the same given potential was simulated by the same point technique as the gates. A new simulation resulted in quite a uniform field in the problematic region. Therefore this grid was scheduled to be added in the second development step of the drift tube.

While the collection plate rings would detect a large section of the ions in the tube, the interface to the heated capillary will only uptake a much smaller part of them due to its diameter compared to the whole drift diameter. A positive effect of taking only the central ions is an increase in resolution which was desired an therefore forced by slightly defocusing the ions at the exit as described in other setups[11]. Ions drifting in the middle of the tube will have straighter flight path than those closer to the walls that feel less of the field distortions caused by the rings as discussed before.
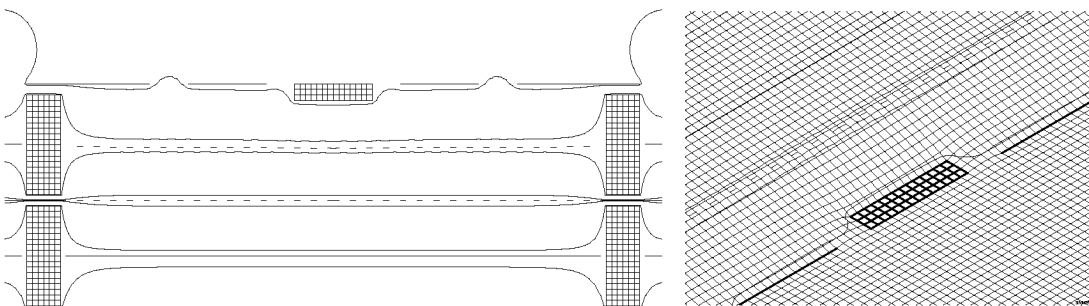

Figure 4.10: Focusing tip on the heated capillary.

Nevertheless the effect of an additional tip in a flat disc form on the heated capillary pointing into the drift region was simulated. The most important question was its effect on the field in the timed region. As figure 4.10 shows, almost no distortion of the timed field part but a small focusing effect is observed.

The last important part to look at was the field uniformity at the entry of the timed region and in the desolvation region. The potential lines at the entry of the drift tube show a uniform field after the third ring in figure 4.11 (final tube version shown) if an entrance grid is used. Leaving this apart the field at the entry would point in the direction of the walls and therefore capture most of the ions.
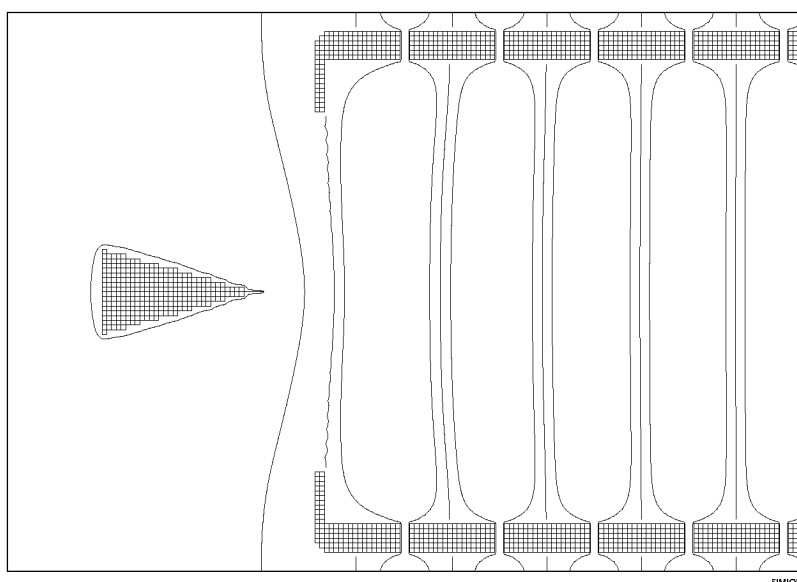

Figure 4.11: Potential lines at the entry of the drift tube show a uniform field after the third ring.

Conclusion

With these simulations the designed geometry was verified to give a sufficiently uniform field within the timed drift region. With additional features like the field correction grid in the last aluminium ring or the focusing tip on the heated capillary entry the performance of the drift tube could be even more improved in a final version.
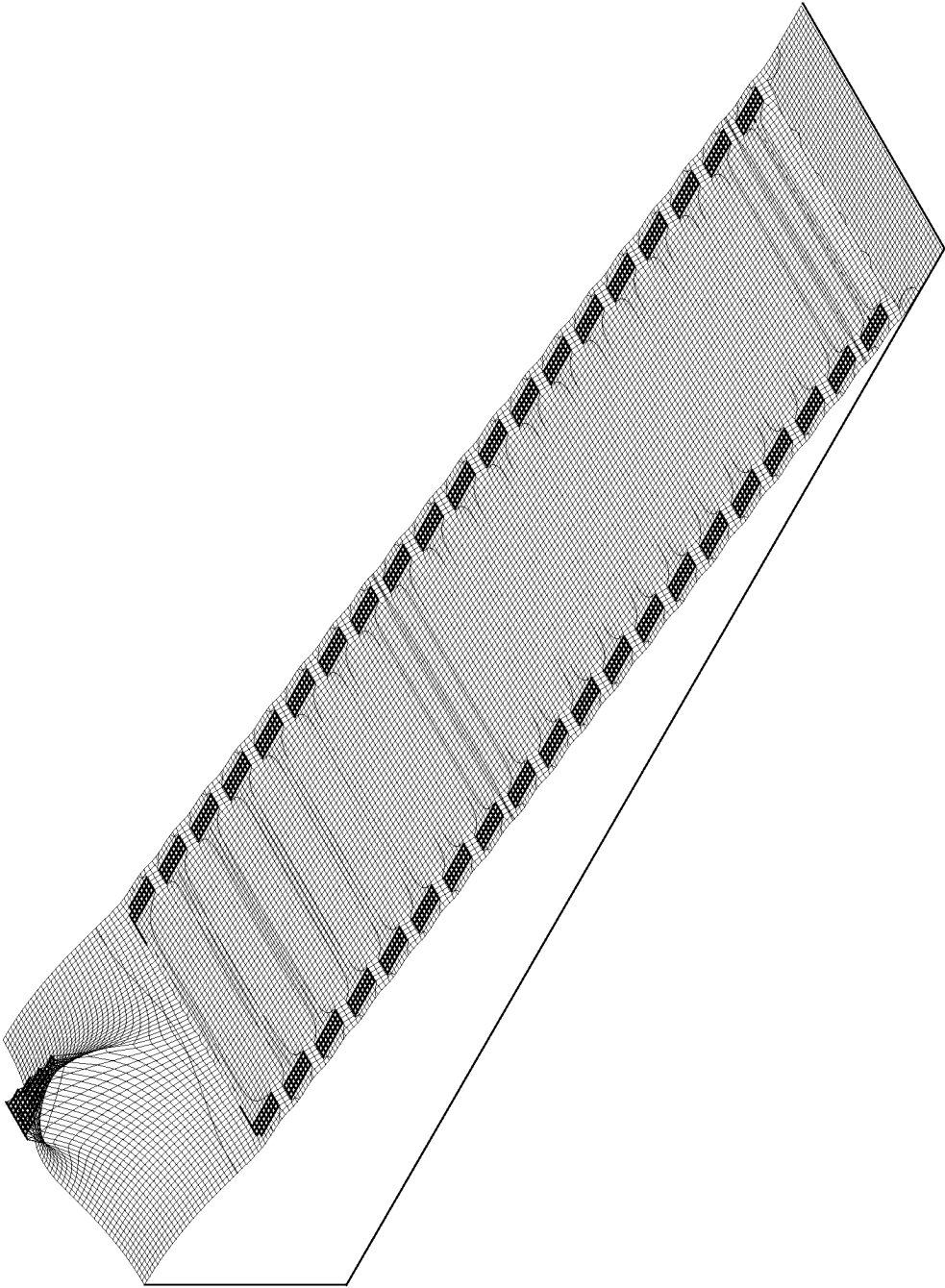
SIMION

Figure 4.12: Potential lines and field grid of the complete drift tube
(second version)

4.3 Design and Construction of the Actual High Pressure Drift Tube

After the calculations described in section 4.1 a first design was drafted and subsequently improved in a second step. The operation temperatures were planned to be between 100 and 250°C(desolvation, cluster prevention), the operation voltages up to 6 kV (up to 12 kV for the spray tip) which is an important fact for the whole design and the characteristics of the insulators. This limits the usable materials quite strongly to metals, ceramics and some high temperature polymers which are easier to machine than ceramics. Two polymer types were selected for different insulating parts in the heated region: PTFE or Teflon®(PolyTetraFluoroEthylene) a soft polymer which stands up to 260°C for wire insulations and foils and PEEK (PolyEtherEther-Ketone) a hard semicrystalline thermoplastic which stands up to 265°C for the inner skeleton parts.

All the described parts were built in the in-house mechanical and electrical workshop at ETH Zurich.

Building the Drift Region

The drift region as inner part of the drift tube was designed as a stack of 21 aluminium rings with PEEK insulators in between. The section profile of the rings is already shown in scheme 4.5. For the peak insulators square plates with rounded edges were cut out of a 3 mm PEEK sheet. The edges were drilled for the mounting on a stability rod (s. scheme 4.6). The clearance was set to 60 mm to fit the interleave of the aluminium rings. The four stability rods were built completely out of PEEK including the nuts at the upper end.[2]

Spray - Entrance Grid

As discussed in section 4.2.3 a grid at the entrance is required for the field to guide the electrosprayed droplets into the drift region. The entrance ring was designed to carry

---

[2]The initially chosen stainless steel could not be successfully insulated against discharges even by ceramic and interleaving PEEK parts.
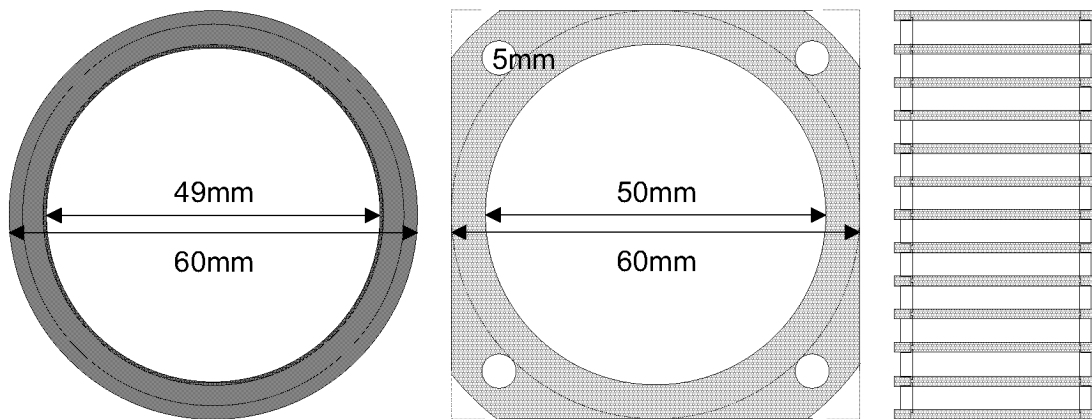
Scheme 4.6: Draft of the stacked aluminium (left) and PEEK (middle) rings.

an electroformed 20" copper mesh of 95% ion transmission (20 copper wires per inch, 0.00127" − 30 μm wires, BM0020-03-C, Internet Mesh Inc. Anoka, Minnesota, USA). It was built out of a aluminium cap with rounded entry edges fitting over a support ring for the mesh secured by two sinked 1 mm metric stainless steel screws avoiding any visible edge upon this high voltage.[3]

As spray head either a standard ESI source from a TSQ 700 or an in-house built spray head can be used.

Bradbury-Nielsen Type Gates

The Bradbury-Nielsen type gates were mounted replacing a standard insulation PEEK ring and were located after the eighth and before the last aluminium ring bracketing the drift region. The planned wiring at distance of 0.6 mm with alternating electrical connection was first tried with different hole patterns on a PEEK unit but proved to be too complicated to build. Therefore we chose to directly spot-wise weld the fine Pt wires of 30 μm diameter in a distance of 1.2 mm onto 0.5 mm thin stainless steel

---

[3]In the first building attempt the first aluminium ring was milled to have a parabolic outer shape carrying a flatly parabolic shaped stainless steel mesh which was hold by a larger PEEK plate at the entry which didn't show sufficient ion transmission(s. figure 4.13.

plates which have the same radial shape as the PEEK insulators. The wire positions were chosen to result in a 0.6 mm distance between the alternating wires when two plates were put together with the wired side. In between the two plates a 0.3 mm thin PTFE insulation foil was added. The resulting "sandwich" was then mounted in between of two 0.75 mm strong PEEK insulation plates of the same shape. The end capsules of the connector wires were welded directly onto the outside part of the stainless steel plates. This results in a slight interleave between the two alternating poles in the drift direction. Nevertheless the construction still produces a high enough perpendicular stopping field at an applied voltage of 40-50 V.

Wiring and Contacting

For the wiring in the inner part soldering is not recommended due to the high temperatures and possible aggressive vapors. Therefore only screwed or plugged contacts were used. The 1MΩ high temperature resistors (Caddock MS 220)[4] with gold wires were directly screwed onto the alumina rings by cold plated brass screws.

While all normal insulation plates where bridged by one resistor, the reference voltage of the gates was set by 2 + 2 parallel resistors resulting in two times 0.5 MΩ (s. left side of scheme 4.7). Each gate has three necessary connections: the reference output of the resistor bridge and two inputs for the gate electrode plates.

For the high voltage connections copper lacings with a diameter of 1 mm and 1 mm teflon insulation were screwed to the aluminium rings and to connectors built out of brass screws and PEEK sockets at feed through positions to be connected by the outside wires ended up by gold pins. The connector for the 6 kV at the entry ring was connected directly over a gold pin on this ring and taken trough the front plate back to the side.

The outside wires are then soldered to SHV connectors using a special high temperature soldering tin alloy with a melting point of 375°C. The SHV connectors are mounted in a a aluminium box sitting on the side of the outer housing.

---

[4]Caddock MS 220 1 MΩ power metal film resistors, max. 1 kV and 275°C, ΔR 0.5%, Caddock, Riverside, California
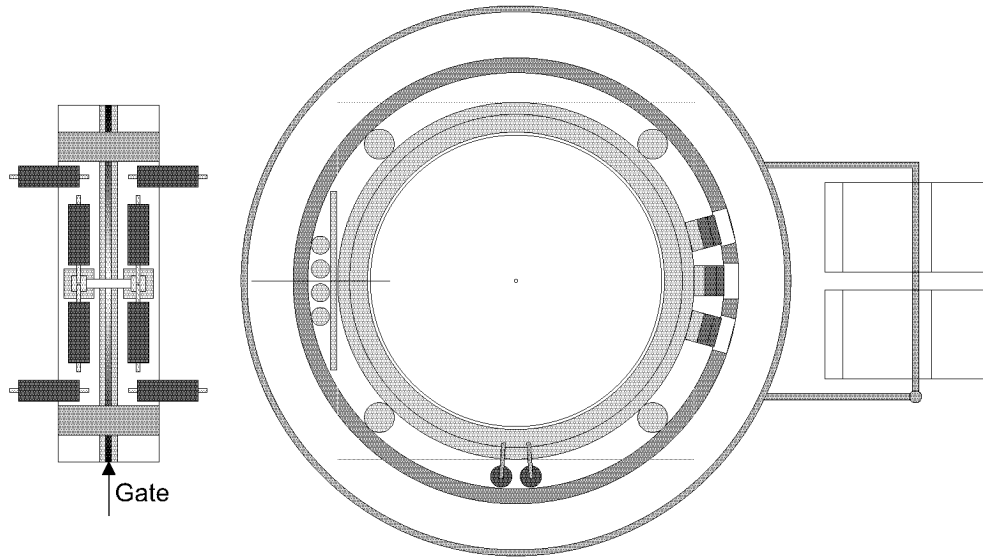
Scheme 4.7: Resistor bridge and vertical section of the drift tube.

Electrical Insulation

As a first insulation shell a 75 mm outer diameter glass tube with a wall thickness of 2.5 mm also holded by the two PEEK end plates was produced which contained 7 connection holes at the location of the high voltage connector sockets.

Heating / Gas Heating

The glass insulation tube was taken as support for a glass silk insulated heating cord (6 m x 4.5 mm, 230V/873 W, max. 450°C, Isopad, Heidelberg, Germany). The heating cord was wound over the whole length of the glass tube and thermally insulated by 3x1 mm glass wool mat and a aluminium foil cover omitting the seven high voltage connection holes.[5] For the heating regulation two Pt100 (100 Ω linearly temperature dependent platinum resistor) were placed, one Pt100 in the middle of the coiled heating cord between the windings, the other beside gas preheating tube.

---

[5]Before the necessary change of the material for the stability rods the heating was built inside of those with four stainless steel heating tubes (118x2.5 mm).
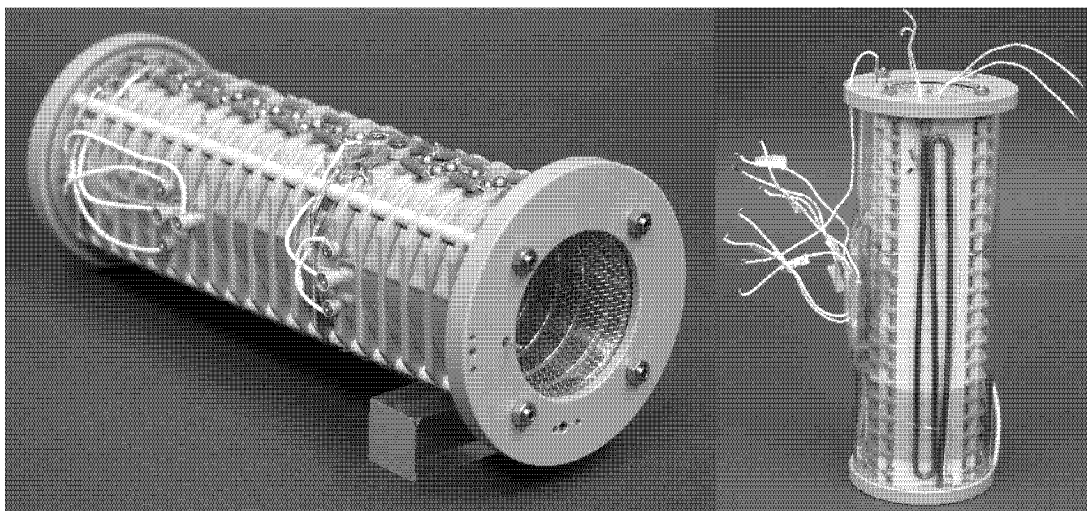
Figure 4.13: Pictures of the inner part of the drift tube (first design)

To preheat the drift gas three turns of a SWAGELOK 1/8" copper tube was mounted in the region between two heated rods. The upper end makes a 90° turn over a PEEK interface connected to another 1/8" SWAGELOK tube for the gas supply. The lower end was plugged into the PEEK end plate. The gas then passes through a flute inside the end plate into the drift tube (s. figure 4.13 – right side).

Interface / Back Plates

The PEEK back plate was built in two parts shown from both sides in figure 4.14. The outer ring contains the counter threads to the four stability rods and the gas flute. On the inlay two copper plates were mounted for a possible direct ion detection (screwed through it by welded on threads). The outer plate is at the reference voltage while the inner plate is coupled to a low current detection. To pick up reference voltage from the heated capillary of the mass spectrometer pointing into the small hole inside the inner plate, a tracer pin sitting in a PEEK holder is pressed onto the heated capillary by a brass leaf spring on its back mounted with the same nut as the reference plate on the other side ensuring the direct contact. The nuts of both plates are connected to a shielded teflon insulated coaxial copper cable of only about 15 cm length to enable low current detection.
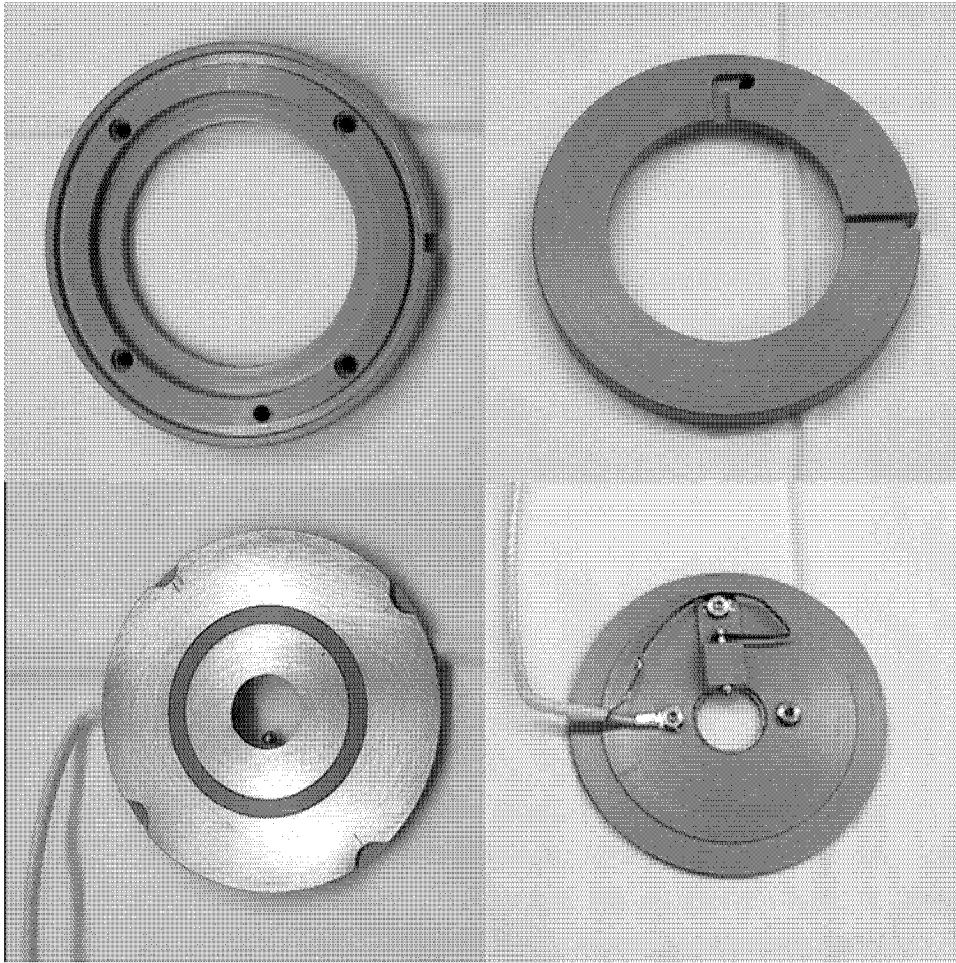
Figure 4.14: The two parts of the back plate of the drift tube.

As discussed in the calculations in section 4.2.3 an important improvement of the electrical field at the exit can be made with another mesh electrode. Therefore the last aluminium ring was cut into two halves mounting a mesh of the same type as for the entry grid screwed together by 4 sinked 2 mm stainless steel screws.

Housing and Mounting

The package was then mounted inside a grounded 90 mm diameter aluminium housing built out of three pieces held together with metric screws. The back piece was build to fit exactly into the entry of a TSQ 700 API interface omitting 3 breathing pipes to reduce thermal contact (s. figure 4.8).
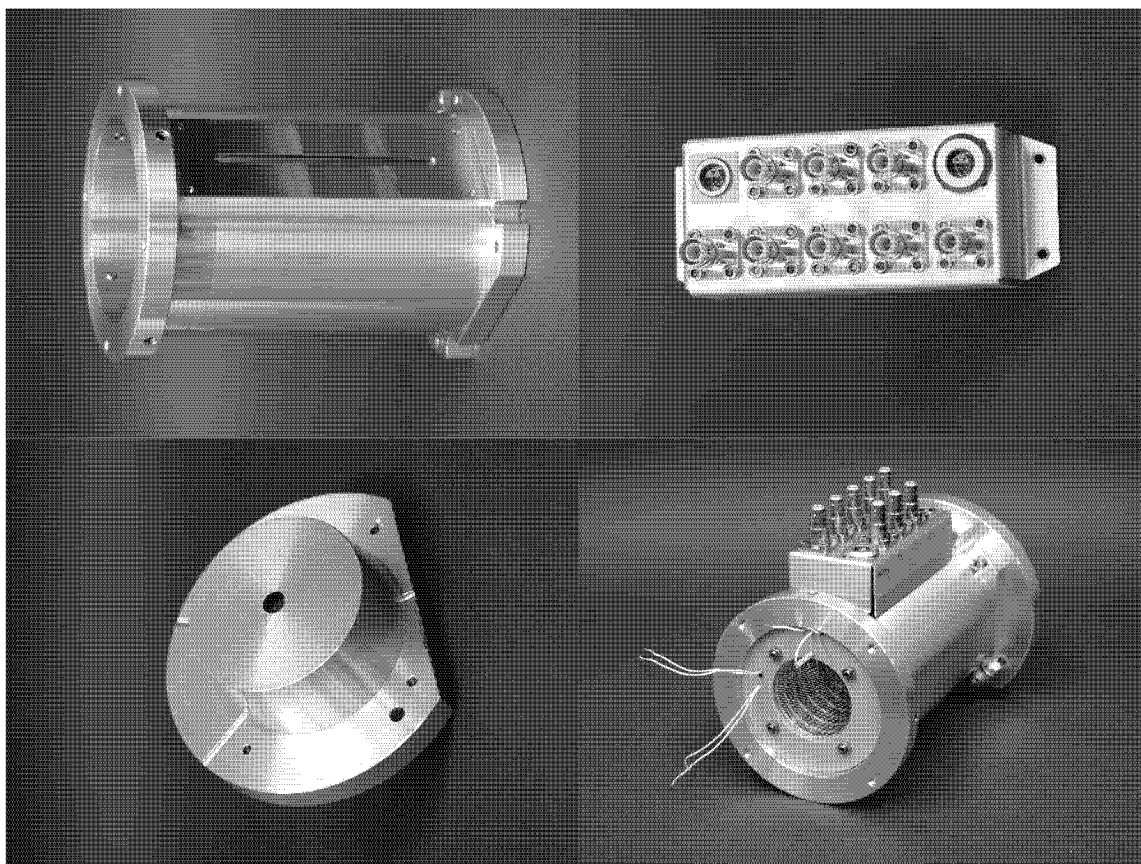
Scheme 4.8: Parts of the outer housing and the complete drift tube.

Initial Tests

The full setup was tested upon successful heating and the behavior under the desired 6kV drift field voltage. The final mount of the modified setup shown in scheme 4.9 can operate at 6 kV (tested at 220°C) with He and N_2 gas flow with good ion transmission. Additionally several ion transmission tests at 6 kV connecting the drift tube to a TSQ 700 MS were made with a 10^{-5} M solution of tetra-butyl-ammonium in methanol using the standard TSQ electrospray source at 10-11.5 kV. In the final version of the drift tube the ion transmission reached acceptable values.
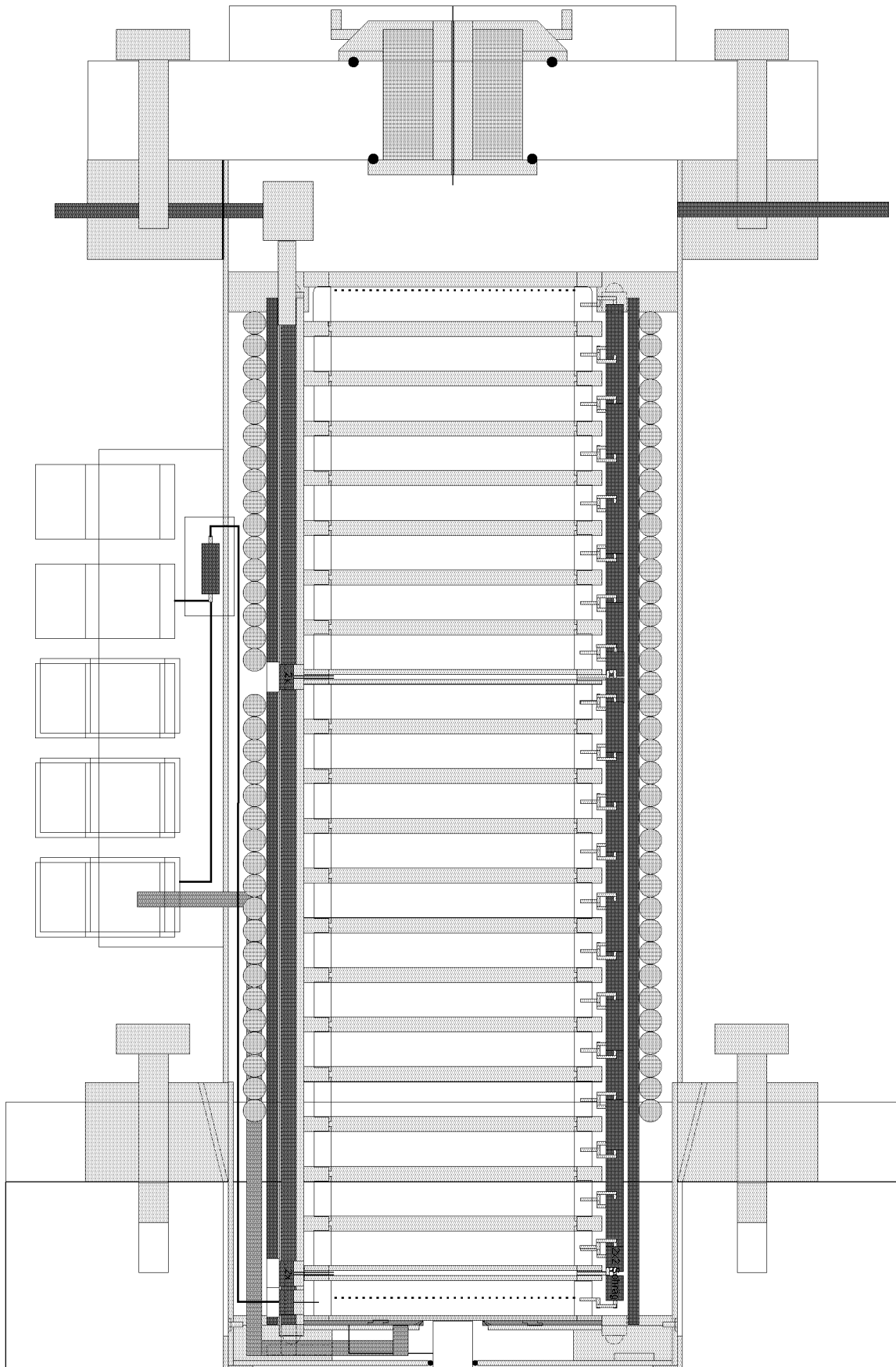
Scheme 4.9: The final design of the built high pressure ion mobility cell

4.3.1   Design and Evaluation of a Cooled Electrospray Source

The cooled electrospray source was designed together with Rudolf Hartmann for the first part.

For the first experiments the original TSQ 700 ESI source was taken. For the desired high temperatures of more than 100°C in the drift tube the electrospray process in direct contact with the heated gas room is disturbed or even stopped upon fast solvent evaporation. A solution was published using a cooled spray head.[90] The necessary voltages of 10-12 kV for the electrospray process out of a conventional ESI source against an entry grid at 6 kV is somehow complicated to produce, insulate and handle. Nanospray at a relative voltage of several 100 V to thee entry grid would simplify this a lot.

Evaluation experiments with an open frame source with free adjustability of the mounted tip were made to investigate distance and flow rate for 6 different solvents to obtain a minimal stable spray voltage using both tip types coupled to a TSQ 700. It turned out to be possible to spray with the steel capillary (80 μm i.d.) starting at 2.5 to 3 kV if a short distance of 3-5 mm to the interface was used. The nanospray started at 600 V with a distance of 1-2 mm.

Taking the two construction goals mentioned before a new cooled ESI source was designed with both nanospray and a slightly advanced conventional spray source capabilities with a thin steel needle. The robustness and the better cleaning possibilities of a fine steel needle makes the latter solution preferable.

The final design is shown in scheme 4.9 and figure 4.15 where the spray needle is pointing into a hollow PEEK jacket with a through-flow of cooled isopropanol at 0-25°C depending on the mobility cell temperature. The jacket was mounted through a 15 mm aluminium plate closed by a surrounding thread and sealed by O-rings on both sides of the aluminium plate. The tips were mounted by HPLC ferrules and teflon sleeves in a charged stainless steel LC "ground piece" connected to a fused silica inlet capillary. The inner diameter of the orifice was designed for commercially available coated glass nanospray tips (New Objective) with the coating contacted by a fine wire to the "ground piece". For the fine steel capillary (80 μm i.d.) option an aluminium lance with a cone at the outer end holding a stainless steel jacket needle with the inner diameter fitting to the outer diameter of the steel capillary was used to increase thermal
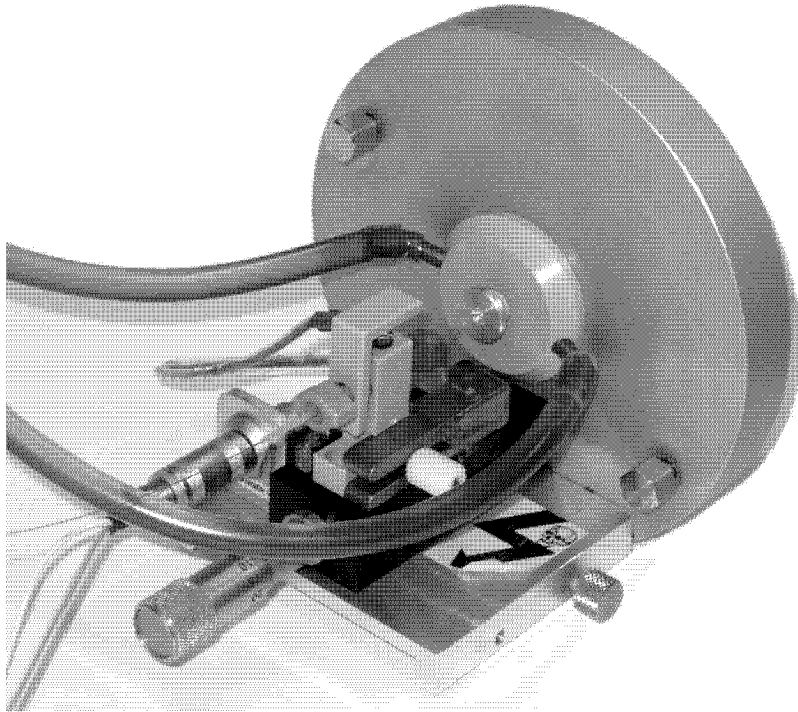
Figure 4.15: Picture of the cooled spray head.

contact to the cooled PEEK jacket. The spray tip position is longitudinally adjustable by micrometer threads.

4.3.2 Software and Driver Environment for the High Pressure Drift Tube

Hardware

All external connections to the mobility cell carrying high voltage were made over SHV connectors and cables.

The 0-6 kV high voltage for the mobility cell was delivered by a FUG HCN 35-12500 or HCN 35-6500 bipolar high voltage supply (FUG Elektronik GmbH, Rosenheim-Langenpfunzen, Germany) connected to the first aluminium ring while the ground was connected over a last 1 MΩ resistor to last ring keeping a uniform decrease in the field up to the end at near ground potential.

The spray voltage was delivered either by the larger FUG supply or by a small Emco E121 high voltage converter (0..+/-12 kV DC, 3 W, Emitec AG, Switzerland).

The two +/-40...50 V gate functions on floating ground which had to be raiseable up to 4 kV were produced in a in-house constructed pulsing device. Driven by two TTL pulses the differentiated signal was inductively coupled over separation transformers into the high voltage regime where amplification and again integration took place to form two times two hard mirrored rectangular signals of the desired reference voltages (taken from the reference outputs of the gate bridges).

For the detection plates a low current detector using a LMC6001 low current amplifier and a subsequent operational amplifier was built in-house. It was supplied by a stabilized dual power supply to lower the internal noise by reference.

Temperature control was made over a two point regulation with the two Pt100 using a Störk difference temperature regulator (ST 48-35.04, Störk-Tronic, Stuttgard, Germany) and an additional autotransformer to limit the heating current as additional overheating protection.

The gas flow was regulated over a mechanical flow meter with fine regulation needle valve (Porter F150-AV1, Hatfield PA, USA).

For the cooling of the spray head isopropanol was pumped through a Peltier element with backup cooling by an in-house cooling water supply regulating the temperature by another Pt100 temperature controller.

The ion detection signal of the TSQ 700 dynode was amplified by another operational amplifier connected directly to the electrometer board of the MS.

The necessary TTL signals and the A/D conversion of the readback of either the MS ion signal or the low current detector were made on a ADWIN Lite 16 USB box[6]. This is a standalone box with its own mulitasking operating system and programming language with fast access to the devices (25 ns delay). The Adwin card is connected to a 500 MHz Pentium II PC.

An overview sketch of the complete measurement hardware setup can be found in scheme 4.10.

---

[6]ADWIN Lite 16 USB box, Sharc ADSP21062 CPU 32 bit, 256 kB DSP-RAM, 8 MB SDRAM, Jäger Computergesteuerte Messtechnik GmbH, Lorsch, Germany
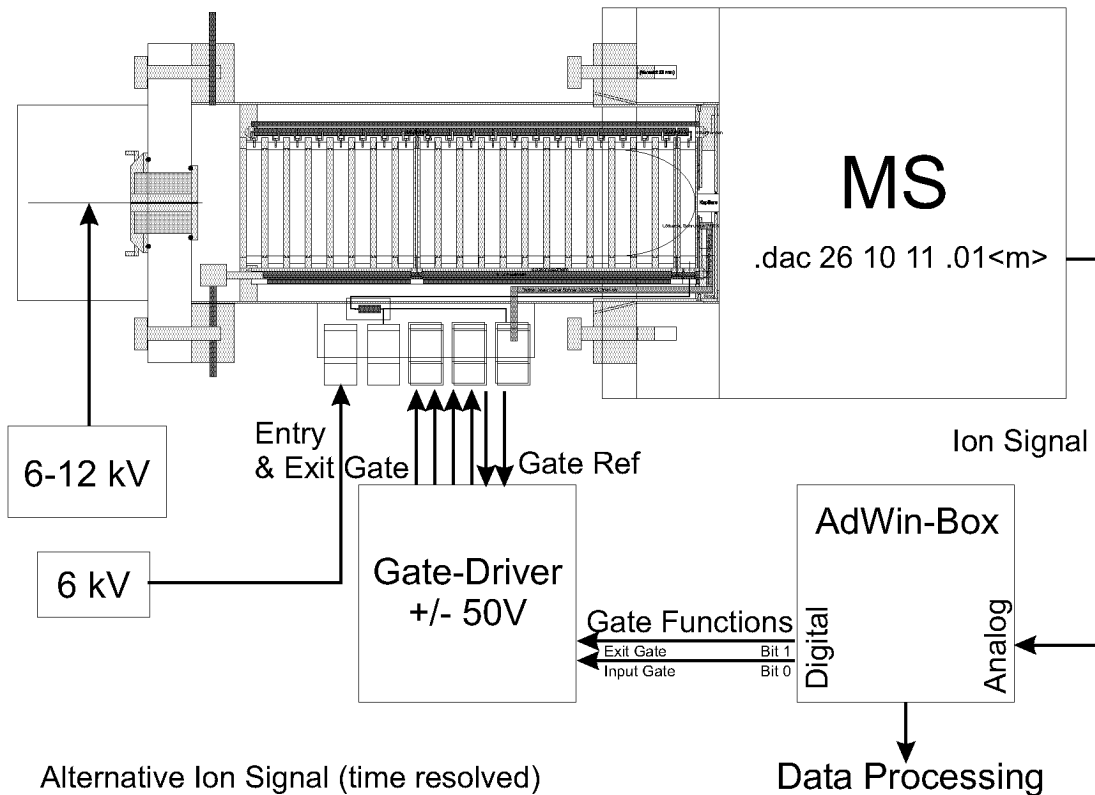
Scheme 4.10: The complete hardware setup of the high pressure mobility cell.

Software

The driver PC is running Windows 2000 SP4 and LabView 6.1[114] and a AdBasic 3.2[115] compiler/sender unit for the direct access to the Adwin card.

For the generation of the exactly timed TTL signals to drive the gates the LabView communication is too slow and not capable to form the regular gate functions in real time. Therefore three different pulsing programs for three different measurement modes described in section 4.1.3 were written in AdBasic which included data acquisition and first averaging were. During the development it pointed out that there is a maximal possible duration of an internal loop on the Adwin card of 400ms until the process is killed automatically by an undocumented watchdog function. Therefore the main loops had to be made with LabView only while making short measurement cycles on the Adwin card.

The program codes of the three AdBasic programs listed below can be found in the appendix:

- **Mobility_One_Gate** – for the one gate pulsing method

- **Mobility_Cut_Loop** – for the two gate cutting method

- **Mobility_FT** – for the two gate fourier transform method

For the Windows side the corresponding LabView programs were written. They host the main measurement loops and are sending the compiled program code, all the input parameters, the start and stop signals and read out the A/D converted data arrays supporting a file I/O and providing a graphical interface. A printout of these programs is also part of the Appendix:

- **Mobility_One_Gate001** – for the one gate pulsing method

- **Mobility_Cut_Loop001** – for the two gate method cutting one fixed mobility

- **Mobility_Cut_Sweep001** – for the two gate method sweeping the time diff

- **Mobility_FT_003_fil-v2** – for the two gate FT method

- **Mobility_FT_004_fil-v2** – for the FT method with additional averaging

- **Direct_Gate_Driv_002-v2** – for direct gate driving

- **Direct_Gate_Driv_uni-v2** – for direct gate driving – both gates simultaneous

For the mass resolved acquisition (all modes) usually a mass selection with the driver software (ICIS) of the coupled TSQ 700 was made using a DAC scan on a quasi intensity independent parameter as the capillary voltage within a one volt range on the desired mass.

The obtained data was stored as raw data in ASCII format for compatibility reasons. For the FT method both, the resulting time and the frequency domain answer signal were stored in a 2D array. The time domain contains the time dependent signal raise caused by the signal response delay of the mass spectrometer, the frequency domain the reference data of the frequency sweep needed for the spectrum generation. The resulting data array files of the FT measurements were subsequently worked up by MATLAB[111] selecting the processed data points of the 2D array by the time dependent response only in the constant part after the raise (s. figure 4.11).
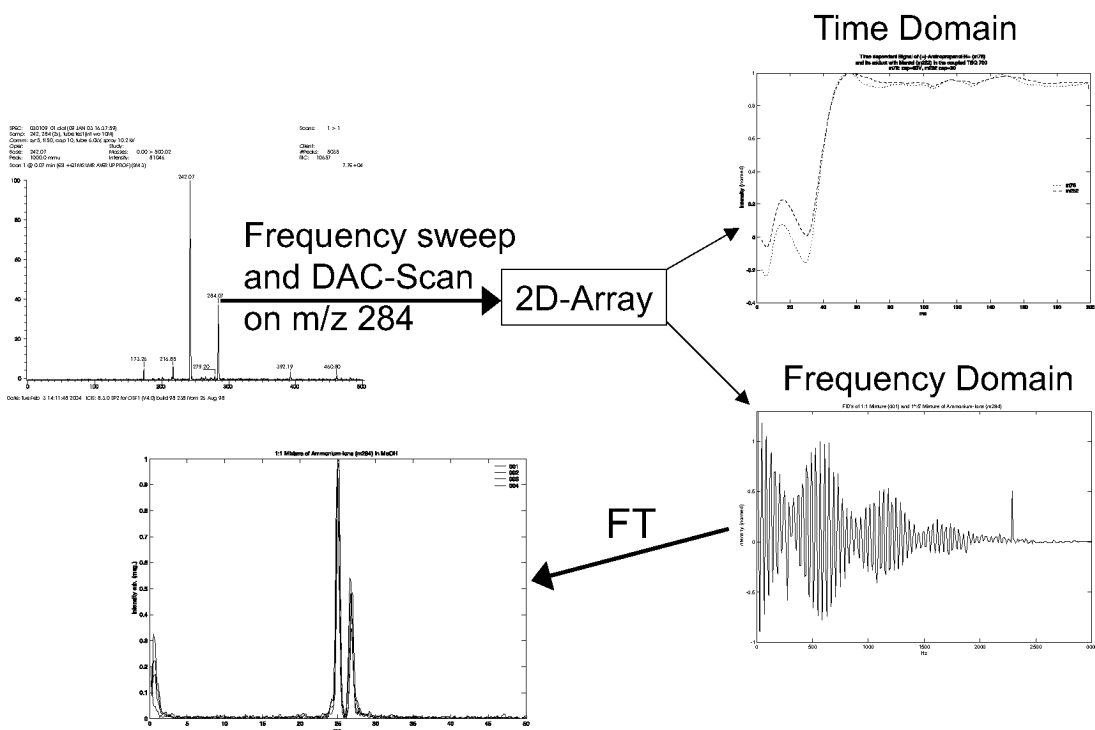
Scheme 4.11: Data processing map for the FT measurement mode.

4.4 Test Measurements With Different Model Compounds

4.4.1 One Gate Method

For the first timed experiments the *one gate pulse method* was chosen to measure the time response of the unmodified TSQ 700 and to determine if this method works for this MS setup. Therefore a 10^{-5} M solution of tributylheptylammonium bromide in methanol (MeOH) was electrosprayed with the cooled spray head into the heated (150°C) drift tube with 800 ml/min N_2 counterflow. Pulsing the first gate for 2ms resulted in a long decay curve delayed by around 30ms as shown in figure 4.16. Pulsing the second gate the same way resulted in the same curve shifted by 20 ms. The measured half–life $t_{1/2}$ was around 15-20 ms. An exchange of the drift gas to helium didn't change the result for the decay.
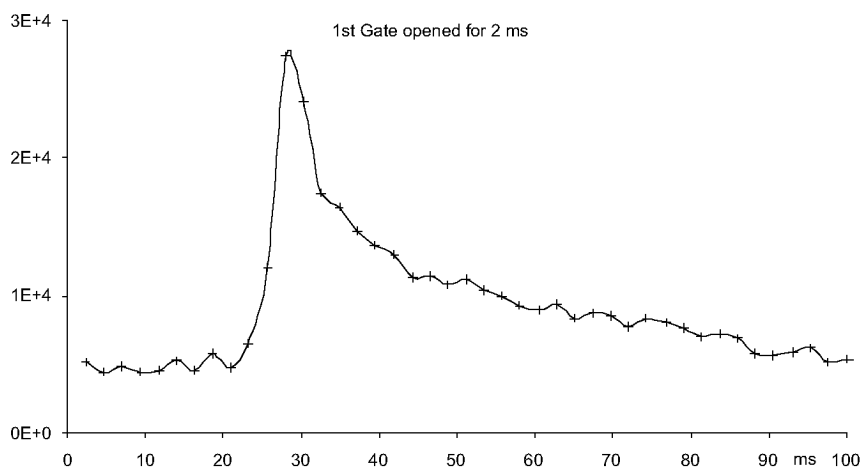

Figure 4.16: Ion signal decay on the unmodified TSQ 700,
one gate method, first gate opened for 2ms
test solution: $C_{19}H_{42}N^+$ in MeOH.

A similar test on the modified TSQ 700 (24–pole) gave a much longer decay with $t_{1/2}$ of around 300 ms. These measurement series negated the possibility of time resolved measurements with the desired resolution in the millisecond range on both tested mass spectrometers.

4.4.2 Two Gate Sweep Method

With the same test solution and helium as drift gas the two gate sweep method was tested successfully but with the expected low ion transmission and resulting signal intensity. The necessity of a constant gas exchange through a gas counterflow to keep the drift region in constant and defined conditions could be shown. Figure 4.17 shows the strong peak broadening if the helium counterflow is stopped, probably due to cluster formation with solvent molecules which can not be exhausted in this case.
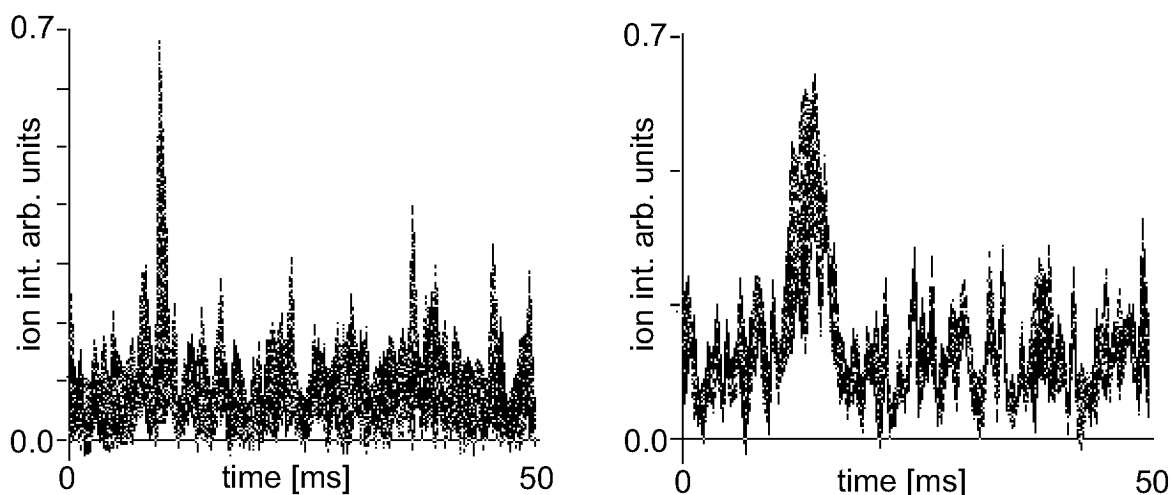
Figure 4.17: Ion signal using the two gate sweep method with 5ms gate opening time, left: He counterflow, right: no counterflow test solution: $C_{19}H_{42}N^+$ in MeOH.

Due to the real low signal intensity a good S/N is not reachable within a reasonable number of measurements. Ammonium ions are known to produce a high ion signal intensity compared to other analytes. Therefore for many other compounds a measurement with this method would become almost impossible.

4.4.3 Two Gate FT Method – Resolution and Separation

With the *two gate FT method* an excellent signal intensity using the same solutions and temperatures could be achieved compared to the two methods described before. Nevertheless a strong signal decrease of at least 10^2 compared to the direct measurement of the solution with the same spectrometer was observed.

For the determination of the resolving capabilities a solution of tetrabutylammonium tetrafluoroborate (**1**) (*m/z* 242) as well as a mixture of the bromides of two isomeric ammonium cations tetrabutylheptylammonium (**2**) and hexadecyltrimethylammonium (**3**) (both *m/z* 284) in MeOH were electrosprayed using N_2 as drift gas at 150°C.

The acquired FID like interference spectrum recorded at the selected mass and the resulting mobility spectrum by a direct FFT is shown in figure 4.18. The FID is asymmetric in relation to the zero–point which can be described with two components. A large mostly bi–exponential decay resulting in a large zero drift time component in the resulting spectrum and the modulating component resulting in the desired mobility spectrum. The modulating part of different runs is in phase and results in a large excess of the cosine part of the FT. The first component (zero frequency artefact) is already discussed in early theoretical FT mobility publications.[108]
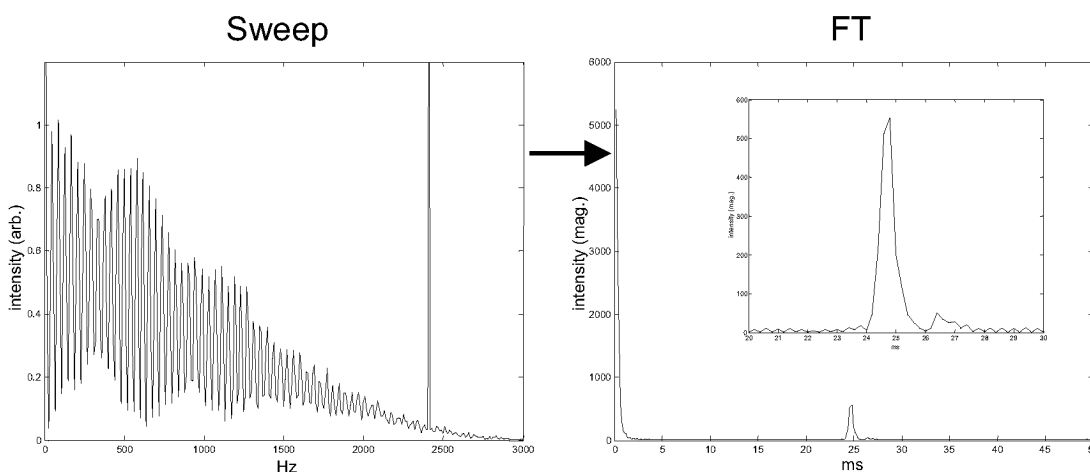

Figure 4.18: Ion signal using the two gate FT method and the resulting magnitude spectrum.

Additional treatment with MATLAB[111] lowers this FT artefact remarkably: Assuming a gaussian peak form for the "zero drift time" decay a base line correction can be made by fitting a quadratic polynomial to the logarithm of the whole interference spectrum. The subtraction results in a more or less symmetrical FID form whose FFT contains much less of the described artefact part (s. figure 4.19). A closer look at the resulting peak form showed two baseline separated peaks for the mixture. The visible ripple on the baseline is due to an uncorrected spike (s. left side) produced by the detector of the TSQ 700. It can principally be reduced by cosinus apodization.
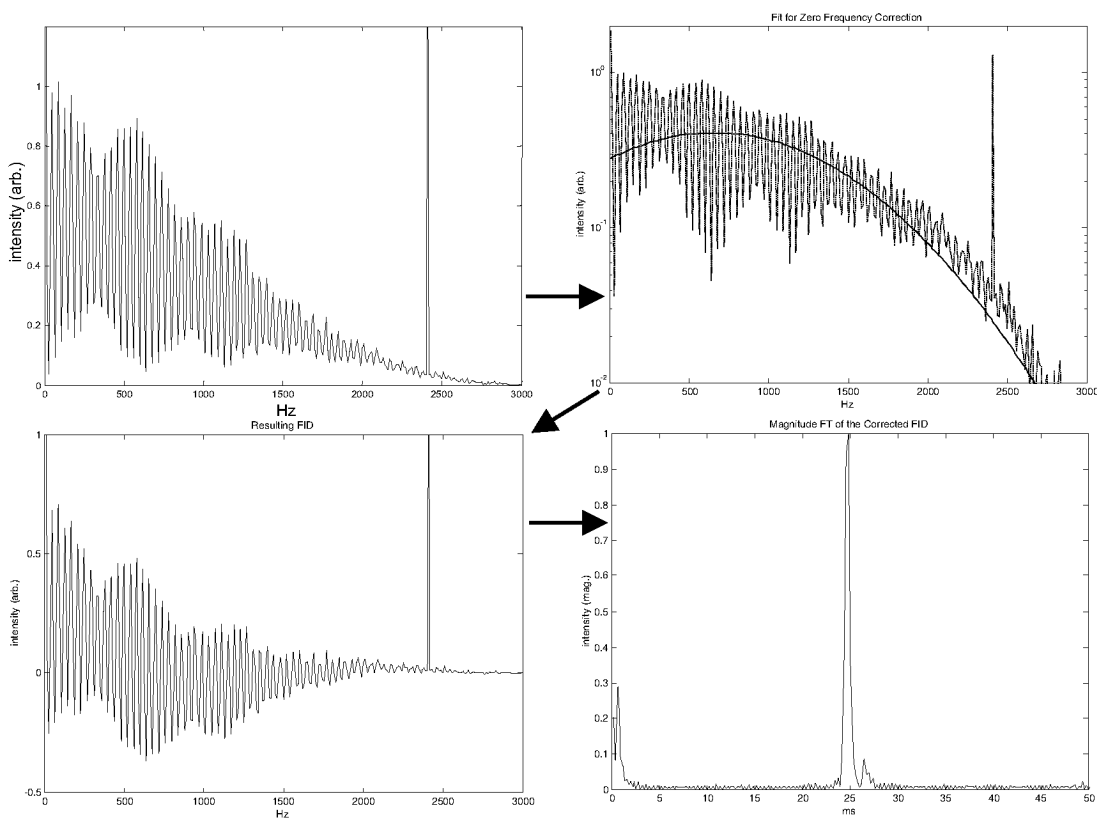
Figure 4.19: Gaussian base line correction using MATLAB.

Spraying the tetrabutylammonium solution under the same conditions resulted in a single peak spectrum as shown in 4.20 (single sweep). The peak width (FWHM) is about 0.45–0.55 ms with a peak position at 22 ms.

The calculated resolution factor ($t_d/\Delta t_{fwhm}$) for the current measurement setup is therefore between 45.5 and 49 which is in fact of the same quality or even slightly

better than for the high resolution mobility cell of Hill's group [11] used as base for the design.
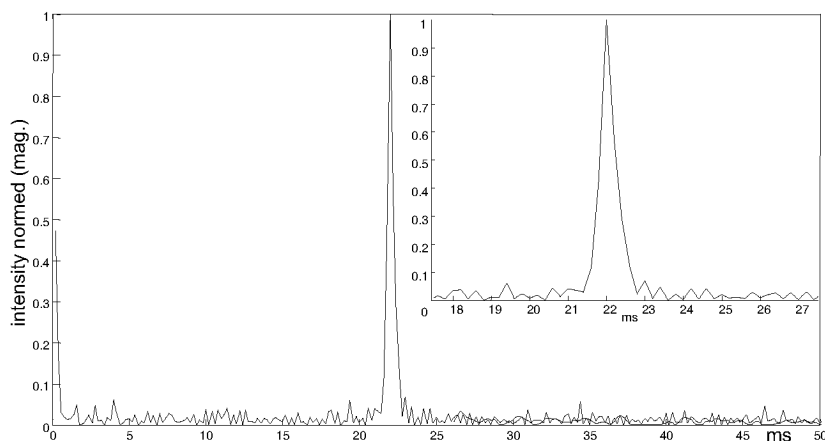

Figure 4.20: Magnitude spectrum of the tetrabutylammonium ion.

To perform a direct assignation of the two isomeric ammonia ions with a *m/z* of 284 two new mixtures with **2** and **3** at the mixing ratios of 1:1 and 1:5 were prepared and sprayed under the same conditions. In the resulting spectra shown in figure 4.21 the ratio change could be clearly observed and the two peaks where completely base line separated. The different colors show different single sweeps documenting the reproducibilty Therefore an assignation of the two isomers could be made without any doubt. The more ball like ammonium ion **2** was observed at a shorter drift time of 24.9 ms than the ion **3** with the more stretched structure at a drift time of 26.7 ms.
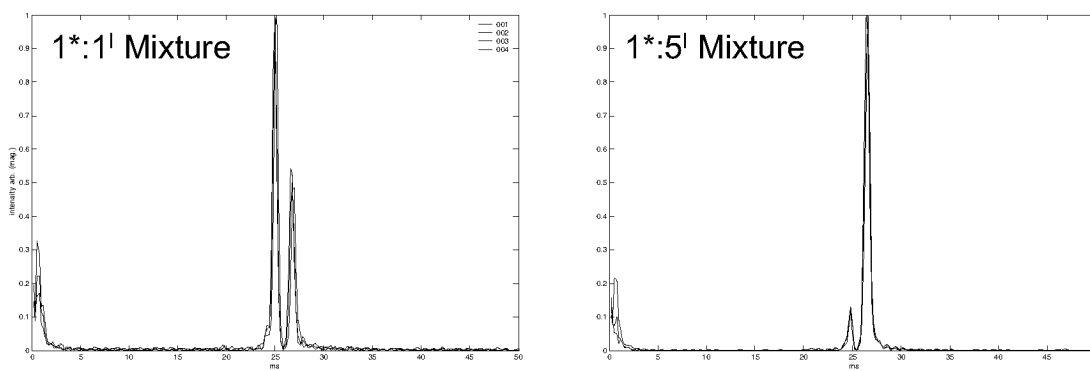

Figure 4.21: Magnitude spectrum of two mixtures of the two isomeric ammonia ions with a *m/z* of 284 in ratio 1:1 (left) and 1:5 (right) (⋆: **2**, I: **3** – 4 single sweeps each showing the reproducibility).

Calculations

For a proof of the correctness of assignment and also for the ability to model the drift behavior in the current setup the two structures were calculated and geometry optimized at force field (FF, PM3)[116] and density functional theory[117] (DFT, B3LYP)[118] level using Gaussian03[119].

Simple 3 Axis Projection

An initial, simple attempt the collision cross section was approximated relatively by a sum of the projections in three orthogonal main spatial directions. This was made by simply printing and cutting out the three projections followed by weighting for each compound. The weighted difference was 7% of the larger value with a confidence interval of 2% given by the cutting precision while the measured drift time difference was 6.6% which matches quite closely. Also the order of the two sizes matched.

Mobcal – PA, EHSS and TM

A calculation with mobcal on the two optimized DFT structures with electron distributions taken from the DFT calculations gave the following three differences for the inverse mobility:

method	difference
PA	9.4%
EHSS	7.3%
TM	6.6%

The PA and EHSS overestimated the difference while TM gave a surprisingly close result to the measured 6.5%

A measurement with a mixture of o-, m- and p-phthalic acid dimethylester (pdme) in methanol was made. For these molecules collision cross sections measured with the single compounds were already published.[92] The m- and p-isomer differ by less than 1.5% were not expected to be separated measuring the mixture. The measurement showed one broadened and a separated peak. Comparing the relative values for inverse K gives a good agreement to the published results.

pdme	Hagen[92]	this experiment
o-	93.25%	90.1%
p-	98.65%	100% (p+m)
m-	100%	100% (p+m)

In analogy to the measurements in chapter 3 Cs^+ and protonated glutaric acid (Glu-H^+) were sprayed separately in MeOH with 10% of AcOH. As shown in figure 4.22 a quite different result than under the low pressure conditions was achieved.

While protonated glutaric acid showed always a well resolved narrow peak, Cs^+ show a real broad peak form at a quite high mean drift time with a good reproducibility (s. single sweeps in figure 4.22 – left side). With helium as drift gas the picture remained the same just at different drift times due to the lower collision efficiency.
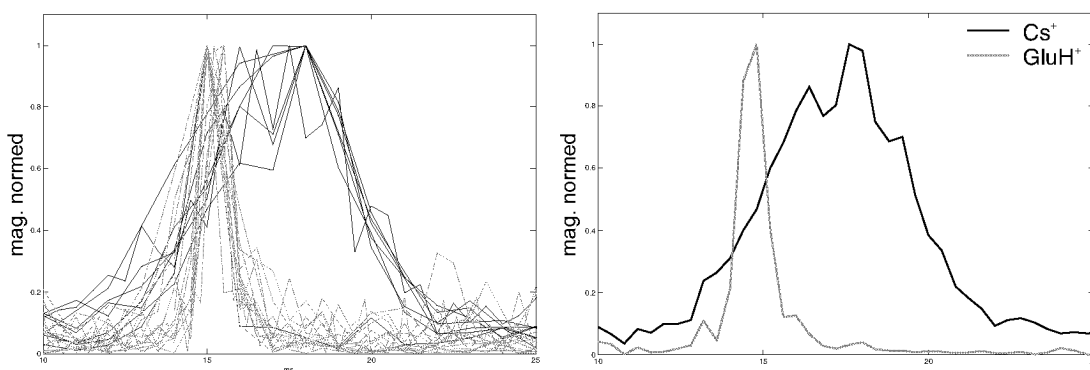

Figure 4.22: Magnitude spectrum of Cs^+ (black) and Glu-H^+ (grey)
left: single sweeps, right: averages of the sweeps showed on left
side

As source for this observation the drift gas can be excluded. As known for electrospray, small and hard ions would loose their closest solvent shell only under hard conditions.[120] In the low pressure experiments in chapter 3 ions passed the tube lens region and a high vacuum region optimized to see Cs^+ as naked ions prior to the mobility measurement. In this case their mobility is measured under soft conditions and high pressure where they keep this shell or loose it really slowly during the drift which would exactly show such a behavior.

Also test measurements with aniline and iodoaniline showed good results compared to literature results.

4.5   Conclusion and Remarks

In this chapter a successful design, development and deployment of a compact high pressure high field mobility cell fitting to the inlet of a standard FINNIGAN TSQ 700 was presented. The hardware allows measurements at field strengths up to 300 V/cm in both polarities and temperatures of up to 250°C with the help of a cooled electrospray source. A software environment for data acquisition in all important measurement modes was developed and tested.

The unavailability of timed measurement methods such as the *one gate method* on our triplequad spectrometers as well as the necessity of a constant gas counterflow in the mobility cell for usable mobility measurements was demonstrated.

The mobility measurement method of choice is the *two gate FT method* with which an excellent resolution factor of up to 50 and reasonable mobility results at good reproducibility was demonstrated using different analyte systems.

Chapter 5

First Attempts on "Real" Systems

Summary

First separation attempts on organometallic and organic compounds by collision cross section with the new ion mobility cell are presented here. A reasonable number of experimental ideas have been tried out. While mobility spectra have been measured successfully, the separation attempts did not work in many cases due to different reasons.

5.1   Introduction

As shown in the last chapter the construction of a new high pressure mobility cell and test measurements have been successful, resulting in a fully functional device with good resolution. As described in chapter 2, many application ideas for the new device existed. However most of them were completely new application fields for ion mobility cells.

Especially in the field of important organometallic catalysts several projects have been performed. The goal was mostly to separate diastereomeric complexes with multiple ligands or ligand substrate combinations by either building different packing sizes, configurations around the metal center or differently protruding side groups. For most of the prepared species a mobility spectrum could be measured but a separation was not possible due to many different reasons. General resolution issues, where the difference in collision cross section is below the separation limit ($<$ 5%) of the current setup as well as fast interconversion at the given measurement temperatures for successful desolvation were important key problems. Additionally the different spraying conditions[1] than directly on our mass spectrometers lead to decomposition of some sensitive complex types.

In the following sections two selected projects are described more in detail. On the following systems measurements were performed but a detailed discussion is omitted:

- Hoffmann type Ru–PP–complexes

- different Rh-PP hydrogenation catalysts

- Cu–BOX and PyBOX complexes

- asymmetric Mn–salen complexes

Additionally experiments on the topic of chiral separations by additives in gas phase were performed. Small organic compounds as 1-amino-2-propanol were measured with menthol as gas phase additive. A separation either by binding equilibrium or different packing size was not successful. A separation attempt of cis/trans configured organic acids and esters was unsuccessful due to low ion yield in the electrospray source.

---

[1] primarly higher temperatures of the gas room around the Taylor cone.

5.2 Mobility Measurements on Diastereomeric Pd–allyl Complexes – Separation Attempt of [Pd(PHOX)(allyl)]$^+$ Diastereomers

5.2.1 Introduction

An important application field of Pd–complexes is the stereoselective nucleophilic substitution of allylic compounds. They now belong to the so called standard repertoire of modern organic synthesis. Mild conditions and compatibility with many functional groups are additional attractive features of the system.[121] A large set of Pd–catalysts mainly with phosphine ligands was tested to give the control over reactivity and enantioselectivity.[122,123] While high levels of enantiocontrol have been achieved in many cases, regiocontrol remains often a problem.[124]

The key step is the binding of an olefinic substrate precursor to the Pd center building a π–allyl moiety by loss of a leaving group in β–position. This species can then subsequently be attacked by another nucleophile for the desired product formation.
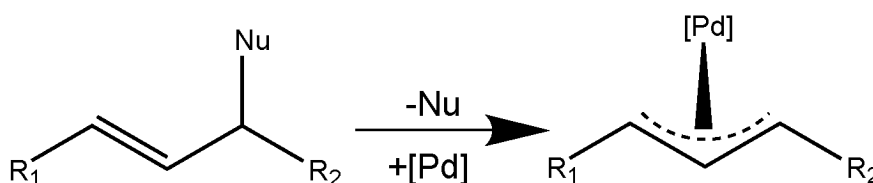

Figure 5.1: Building of the Pd-allyl species.

The nucleophile can attack at either end of the allyl system with most of the substrates. With achiral Pd–catalysts the regioselectivity is only determined by the steric and electronic effects of the allylic substituents. Chiral Pd–catalysts can sterically and electronically control the attack of the nucleophile. Principally the substrate can bind in 4 different ways using bidentate ligands each with different influences on the two positions for the nuclephilic attack.[122] Up to now the binding direction of the allyl moiety can only be controlled using enantiomerically pure educts and cold conditions to avoid interconversion. This is usually done by Sharpless epoxidation and is therefore one of the most important cost issues. An intensive search for also regioselective catalysts is in progress but was not successful yet.[124]

In the group of A. Pfaltz an important class of asymmetric [Pd(PHOX)]catalysts was developed, which reach extremely high ee's of up to 99.5%.[124] Usually the products are investigated by ^{1}H NMRfor the regioisomers and by HPLC for the ee's. Reactivity screening and direct mechanistic investigations with ESI–MS were performed recently in an elegant way using labeled pseudo–enantiomers.[8] But the preparation of the educts somehow remains quite time consuming.

With the goal to additionally resolve directly the different substrate binding directions without the need of the pseudo–enantiomers a ion mobility was started in collaboration with Pfalz's group.

5.2.2 Experimental Results

In analogy to the published procedure,[124] the [Pd(allyl)Cl]$_2$ precatalyst was reacted with PHOX and then subsequently treated with the substrate, a smaller amount BSA (N,O–bis(trimethylsilyl)acetamide) and dimethyl malonate in CH$_2$Cl$_2$to form the [Pd(PHOX)(allyl*)]$^+$species. (allyl*: substituted allyl formed by the substrate).
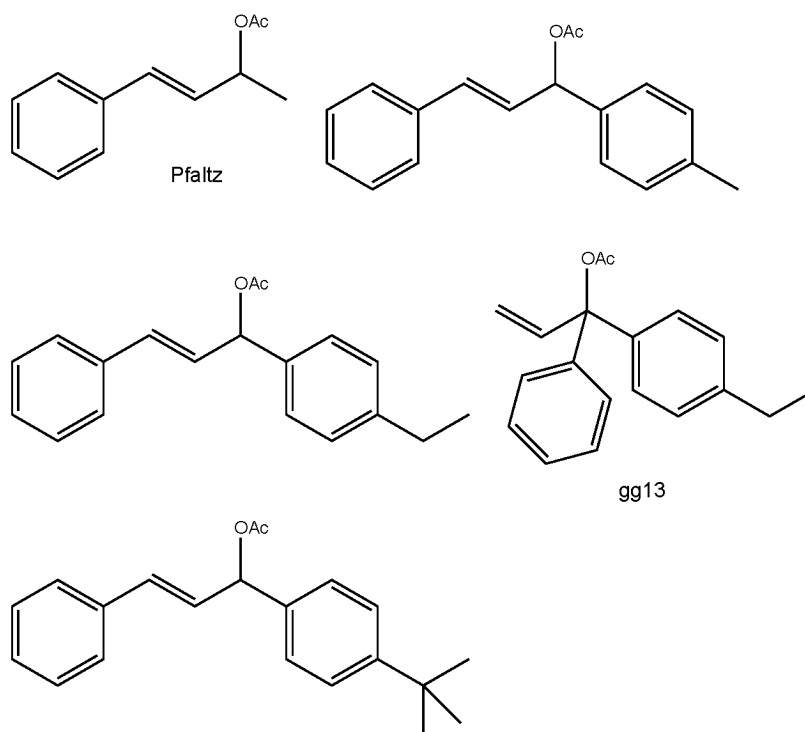

Figure 5.2: Tested set of Pd–substrates.

("gg13": synthesized by G. Gerdes[25], "Pfaltz": a gift from Pfaltz's group[124])

Due to the high *ee* for the [Pd(PHOX)(allyl*)]$^+$ type catalysts only the differentiation of two different binding directions at the given S/N was expected, namely the ones which would be responsible for the regioselectivity (almost no selectivity predicted). A set of different asymmetric substrates was tested with large substituents which were expected to stick out of the catalyst structure in a sufficient way for the different binding directions to be distinguished by collision cross section (s. figure 5.2). The measurements resulted in good S/N and signal intensity.

However the mobility measurements at 120 to 200°C only resulted in one single sharp ion mobility peak (FMHW $<$ 0.8 ms) for all tested complexes. Additionally measurements on a C2 symmetrical Pd–BINAP (BINAP = 2,2-bis(diphenylphosphino)-1,1'-binaphthyl) was performed with an expected *ee* of only around 30-70% with the given substrates.[122] Also these class of ligands resulted only in one single ion mobility peak. An example of such a spectrum is shown in 5.3.
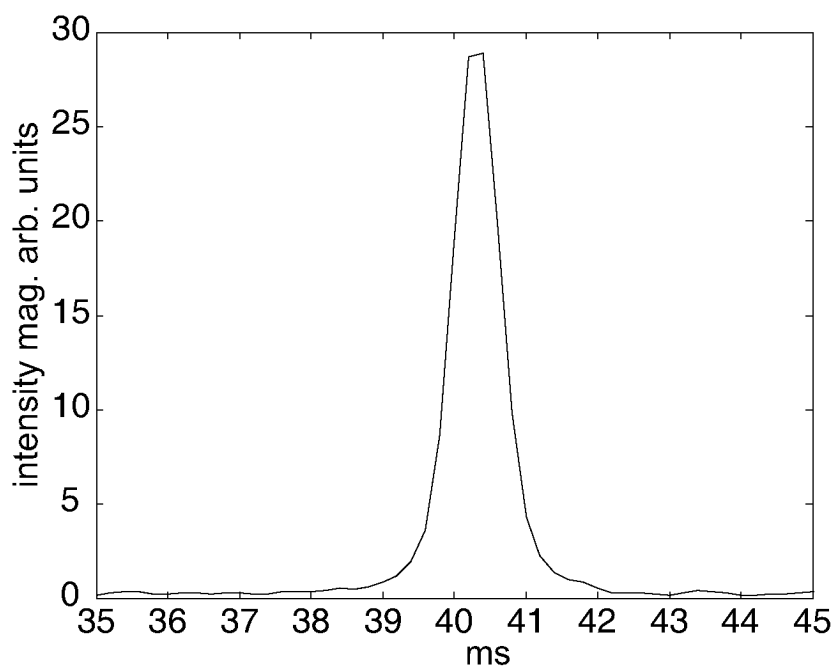

Figure 5.3: Ion mobility spectrum of the Pd–BINAP type allyl complex [Pd(BINAP)(gg13)] at 186°C and an *m/z* of 922 (5 sweeps averaged).

5.2.3 Conclusion

Ion mobility measurements on the Pd–allyl complexes of the the two classes Pd(BINAP) and Pd(PHOX) were performed with good S/N. A a set of asymmetric substrates for the nucleophilic allyl substitution was tested for separation of different binding directions to the metal center.

Unfortunately all measurements resulted in only one single sharp ion mobility peak. This result was achieved presumably due to interconversion of the different binding directions of the substrate in gas phase under the given temperatures in the ion mobility cell.

Several years ago only interconversions in solution by a bimolecular exchange reaction with another Pd–complex were discussed. Current investigations showed that they more likely also interconvert directly on one metal center by a $\eta^3-\eta^1-\eta^3$ rearrangement which is also important for gas phase chemistry.[122] The larger substrates are expected to have quite high reaction barriers but in gas phase under the necessary temperatures for successful desolvation in our mobility cell there is presumably enough internal energy is available.

Therefore for successful structural separations on this systems a redesign of the ion mobility cell which can perform the mobility measurements under low temperatures is presumably the solution. A completely separated desolvation has to be performed which would request a major redesign of the setup.

5.3   The Serine Octamer Project

The measurements for this section were performed together with Eva Zocher.

5.3.1   Introduction

In the last years the self assembly amino acids has become an important topic. It has been observed that serine shows especially a high affinity to itself building so called magic clusters with defined numbers (e.g. 2,4,8,16,18,24,32,...). Due to a quite close packing the affinity to molecules of the identical chiral form is much higher than to the other enantiomer. The most stable cluster for serine turned out to be the homochiral octamer observed by isotope labeling experiments on pure serine solutions.[125] Beside this a mixed packing with arginine, cysteine and threonine of the same chiral form is also made at favored exchanging positions in the same magic number clusters.[126, 127]

These structures and especially the exchange possibilities became important in the field of homochirogenesis, the process by which particular chiral forms of some molecules became favored in the course of chemical and biological evolution, which still remains poorly understood. The single most important aspect of homochirogenesis is symmetry breaking. This is variously proposed to be the result of external chiral factors (e.g., circularly polarized light, vortex motion, magnetic forces) operating on earth or extraterrestrially, or to be a result of statistical effects in small number events or the result of kinetic and thermodynamic effects operating on the small intrinsic energy differences between enantiomers, including those associated with avoided parity violation. Therefore enantiomeric aggregation and enrichments were discussed to be a key aspect of the origin of life.[125, 128]

For most investigations ESI- or the milder method of sonic spray ionization (SSI)[129] mass spectrometry was used to identify molecular clusters present in the solution phase, although the exact timing of cluster formation (e.g., in evaporating microdroplets vs. nascent solution) is generally not known. What is known is that the octamer is accompanied by larger clusters (metaclusters of the type $[\text{Ser}_{8n}+z\text{H}]^{z+}$, namely multiply protonated oligomers of the protonated octamer with exactly its mass over charge ratio) and that it dissociates mainly by loss of serine dimers.[130]
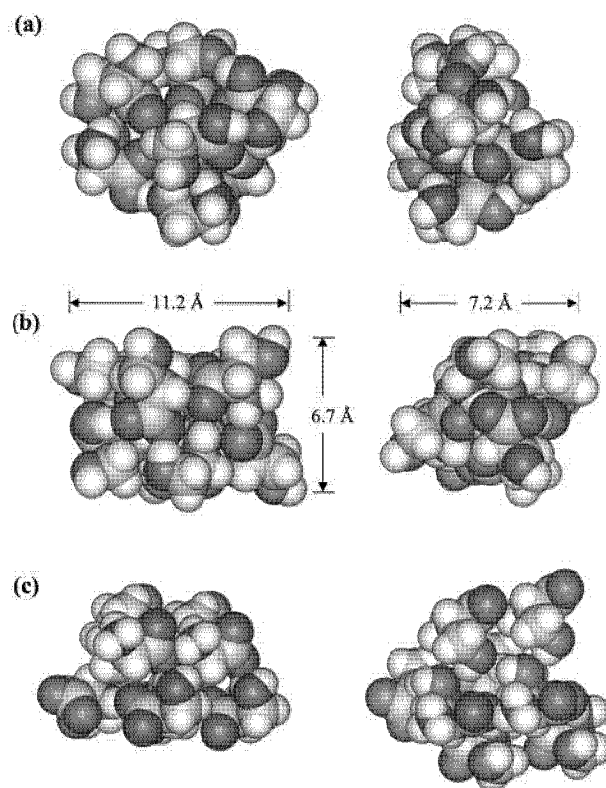
Figure 5.4: Calculated lowest energy structures of the serine octamer:[131]
(a) charge-solvated configuration
(b) cluster comprising zwitterionic units
(c) two unit cells from the crystal structure

Several structures have been suggested for the serine octamer to be stable, based on tandem mass spectrometry, ion mobility measurements, and quantum mechanical calculations (s. figures 5.4 and 5.5), but so far none of them could be considered to be fully established as the structure of the serine octamer. Nevertheless two main structures were discussed to be the most abundant ones:

- irregular clusters made up of zwitterionic monomers and

- regular 4 x 2 clusters of neutral serine.

In the only ion mobility paper about this serine packing topic Clemmer *et al.* reported that only one single form of the protonated octamer together with accompanying metaclusters, which have different collision cross sections but identical mass over charge ratios, was detected with mobility measurements.[131] The published spectra

were measured on a semi high pressure setup with a precoupled ion trap where additional equilibration under gas phase conditions could take place. The S/N presented in the paper was about 10 (in figure 5.5) which would disable the detection of minor species.
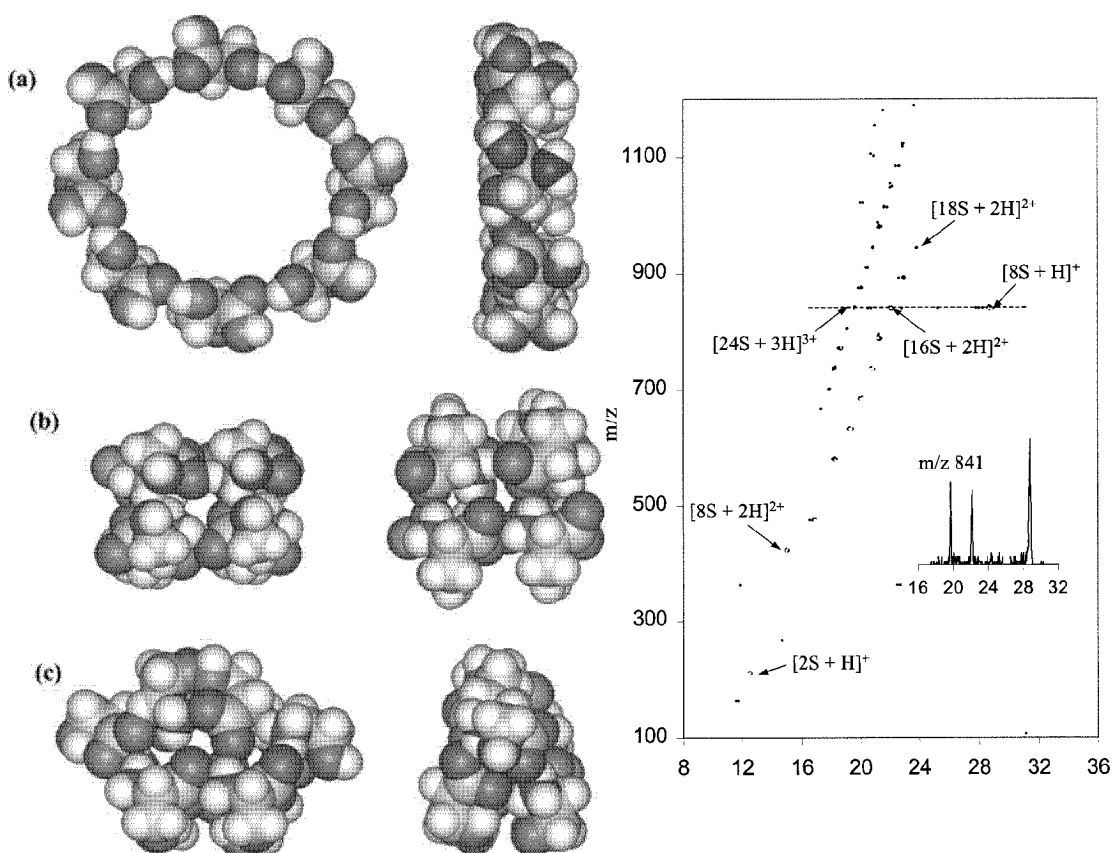

Figure 5.5: Less abundant calculated structures of the serine octamer and published mobility results.[131]

Cooks *et al.* in contrast reported experimental hydrogen/deuterium (H/D) exchange data, which demonstrated the existence of two different important structures for the serine octamer (zwitterionic and charge separated form, s. figure 5.6). These forms undergo exchange at significantly different rates. One form may correspond to solution-phase assembled clusters and the other to octamers formed during the ionization process. Only one type of serine octamer is responsible for the strong chiral effects associated with the formation of these magic number clusters.[125]
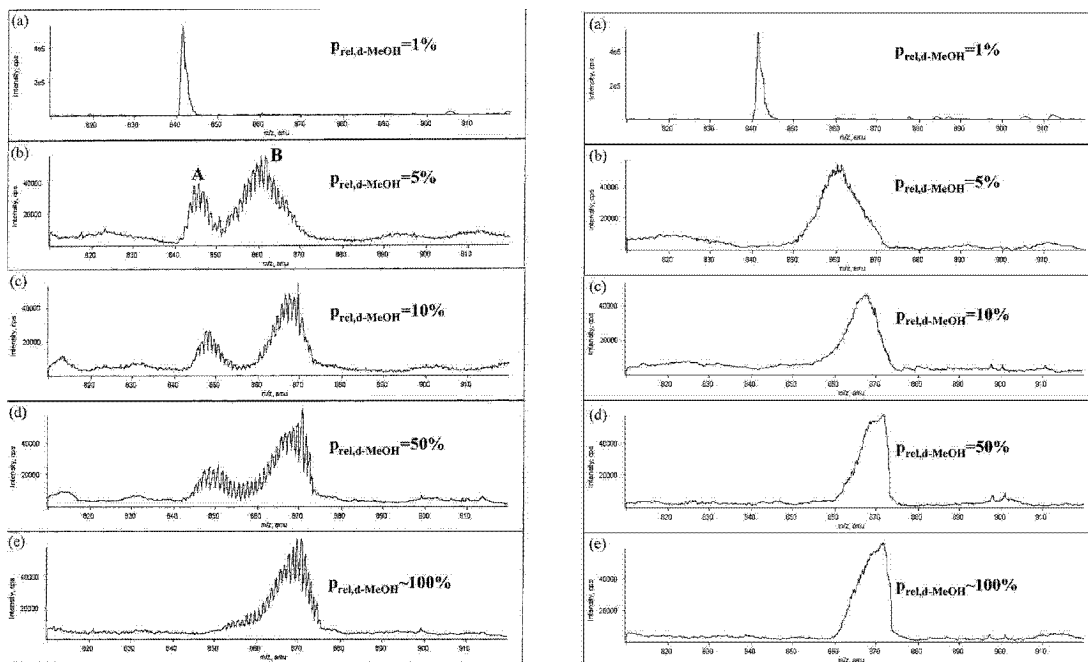
Figure 5.6: Hints for two main forms showed by H/D-exchang
(Zwitterionic and Charge separated form).[125]

Therefore ion mobility investigations on our setup under real soft conditions directly after the spray formation with an FT method to reach a high S/N were expected to give important results concerning the structure assignment or packing differences using different exchanged amino acids.

5.3.2   Cluster Formation Experiments under different Conditions

As discussed in literature[125,130] the main species formed by electrospray with MeOH or MeOH/H$_2$O/AcOH mixtures as solvent under soft conditions using Finnigan mass spectrometers with heated capillary technique are the serine monomer, dimer and octamer (s. figure 5.7). The concentrations used in these experiments was around 10^{-2} M which is a unusually high concentration for electrospray applications causing contamination of the MS machines over time.
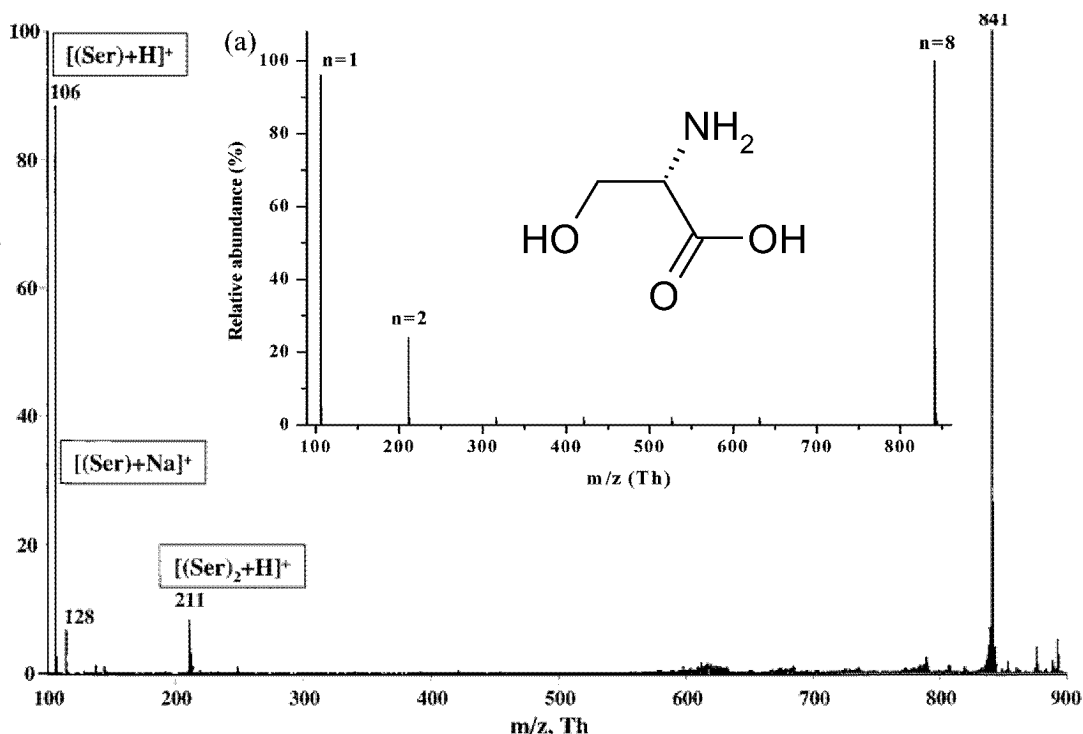

Figure 5.7: Serine octamer spectrum using ESI-MS on a finnigan LCQ.[125,130]

These cluster formation experiments were repeated on our LCQ and TSQ MS to reproduce the results and optimize the conditions for the later mobility measurements. Primary focus was to lower the applied concentration to reduce contamination. Spraying 10^{-5} M and 10^{-4} M solutions of l-serine in MeOH and MeOH/H$_2$O/AcOH mixtures lead only to monomer, dimer and MeOH adducts thereof under softest possible conditions but no octamer was formed. Raising the concentration to 2·10^{-2} M in MeOH/H$_2$O/AcOH (49:49:1) resulted in a similar spectrum as the published

ones.[125,130].

Another group described[131] serine cluster forming with a spray solution concentration of $5 \cdot 10^{-4}$ to $5 \cdot 10^{-3}$ M in $MeCN/H_2O/AcOH$ (49:49:2) which was successfully tested on both of our mass spectrometers types leading to a monomer free spectrum containing only dimer and octamer peaks.

While serine clusters are expected to be preformed in solution also in lower concentration[125,130] the reason for the absence of the octamer has to be a fragmentation during the spray process itself or in gas phase processes after. The observation of smaller methanol containing serine cluster fragments pointed to a possible disassembling of higher serine clusters by methanol coordination during the spray process or in gas phase. Repeating the experiments with solutions of 10^{-5} M l-serine in different mixtures of trifluoro acetic acid (TFA) and trifluoro ethanol (TFE) to avoid coordination and disassembling by solvent molecules, showed under soft conditions beside different smaller clusters below the pentamer a 30% abundant peak at m/z 859 which corresponds to the octamer plus one coordinated H_2O molecule but no "naked" octamer. This confirmed the coordination preference for small polar hydroxy group containing solvents like MeOH and H_2O.

Lower concentrations of l-serine in all described solvent systems failed to bring intact serine octamer clusters into the gas phase. Tests with different settings for the desolvation conditions showed that the formed octamer was quite instable existing only under the lowest possible tube lens settings and therefore softest conditions which was an important fact for the planned application to the mobility cell.

5.3.3   Mobility Measurements on Cluster Mixtures

Subsequent tests of two previously successful solvent systems on the mobility cell failed completely for the usual high drift field of 6 kV and temperatures between 120 and 200°C for N_2 as drift gas. Using He as drift gas (less available collision energy in the center of mass frame – less activation for subsequent dissociation) and 4–6 kV of drift field the octamer could be detected up to a maximum temperature of 150°C while the MeCN solvent mixture system showed cleaner spectra and higher signal yield. The He measurements could only be performed on the modified TSQ 700 (24–pole) due to its better ability to pump He because of the additional turbo pump with large blades.

The lower sensitivity and the longer signal decay times on this machine slowed down the measurement procedure drastically requiring long averaging loops.

With a lowered drift voltage of 2–4 kV and reduced temperatures of 50-80°C using N_2 as drift gas resulted finally also in the successful detection of the intact octamer. As shown in figure 5.8 even a slight rise of the temperature to 100°C which are still real soft conditions, started to fragment the octamer. The fragmentation occured more in loss of smaller fragments than of intact serine monomer units which could be a hint for strong interactions and a compact packing of the present octamer species. On the previous experiments with He as drift gas almost no fragmentation could be observed.
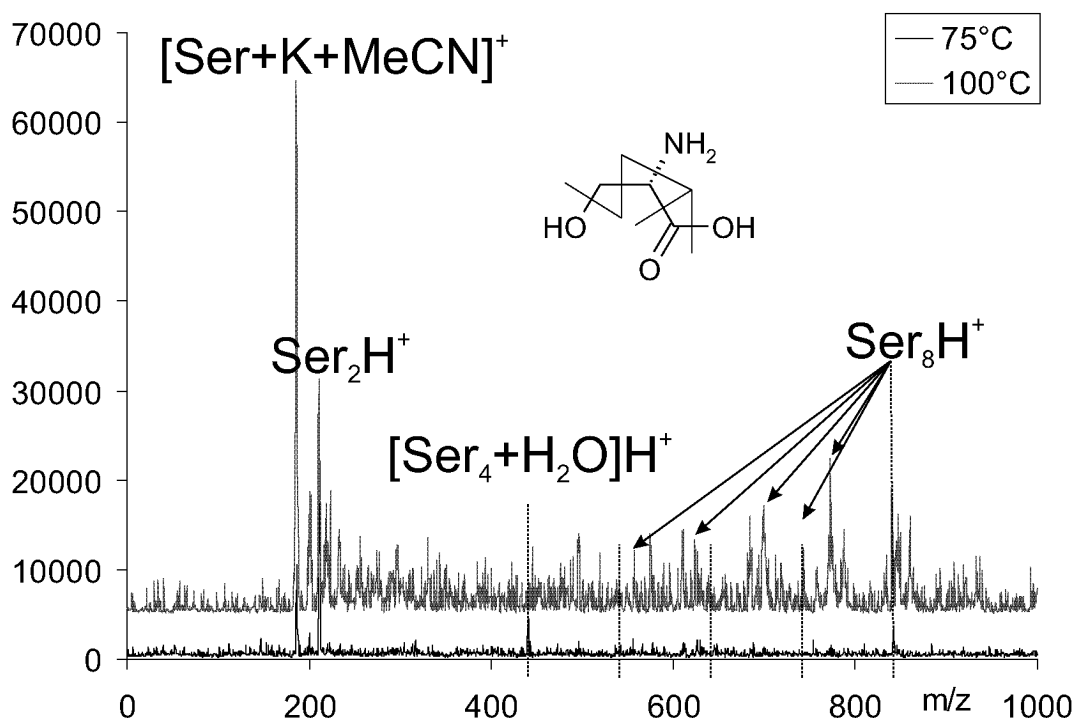

Figure 5.8: Fragmentation of the serine octamer at a slight temperature rise in the drift tube at 4 kV with N_2 as drift gas.

The soft conditions at low fields and temperatures in the drift cell lower the resolution and could not guarantee the complete desolvation of the analytes before entering the timed drift region which also effects the resolution quality. Nevertheless it remained the only solution to measure intact serine octamers. The low total signal intensity made the use of long averaging loops necessary to obtain the mobility spectra

in reasonable quality.

After optimization measurements with He as drift gas at 4 kV and 60°C and 75°C were performed on the modified TSQ 700 using long averaging loops of up to 20 cycles or 4s per sweep data point right at the border level of successful desolvation in the untimed drift region. The obtained spectra in figure 5.9 showed at least 8 different species at 60°C and 3–5 at 75°C. Unfortunately the spectra at 60°C already show clearly solvent tailing on the main species due to incomplete desolvation.
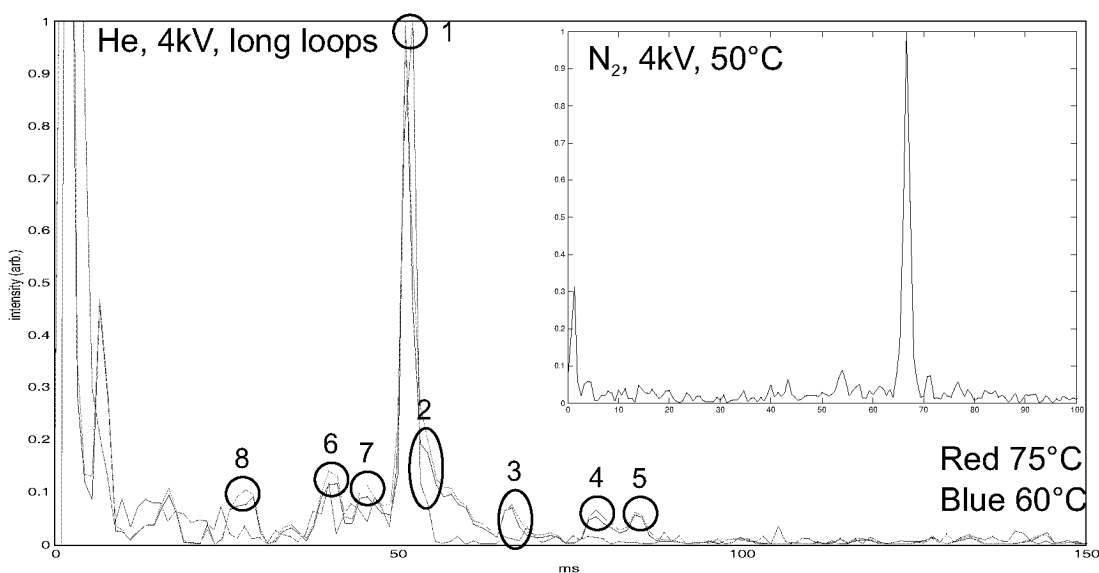

Figure 5.9: Measured FT mobility sprectra at the mass of the serine octamer (l-serine in MeCN/H 2 O/AcOH 49:49:2).

With the help of the already published calculated cross sections of different octamer structures (table 5.2[131]) a reasonable peak assignation could be made for the 8 detected serine $[n(\text{Ser})+z\text{H}]^{z+}$ clusters shown and numbered in figure 5.9:

1   8mer zwitterionic (5.4b, 51ms) - Clemmer's main species
2   8mer charge solvated (5.4a, 55ms)
3   8mer hexameric subunit (66ms)
4   8mer size analog to circle 5.5a
5   8mer 4. + Solvent
6   16mer-2H^{2+}
7   8mer forced packing (40ms)
8   24mer

Table 5.1: Assignment of the 8 detected serine $[n(\text{Ser})+z\text{H}]^{z+}$ clusters.

n^a	z^b	$\Omega_{expt}(\text{Å}^2)^c$	model geometry^d	$\Omega_{calc}(\text{Å}^2)^e$
8	1	191.4(0.2)	circle (5.5a)f	301.7
			cubelike (5.5b)^g	213.1
			hexameric subunit (5.5c)^g	250.9
			charge-solvated (5.4a)^h	204.6(5.1)
			zwitterionic (5.4b)^h	195.3(2.3)
			crystal structure (5.4c)^i	247.9
16	2	294.0(0.6)	forced packing^j	367.2
			forced packing^j	388.8
			compact ovoid^h	304.1(6.3)
24	3	392.4(0.8)		

Table 5.2: Experimental and theoretical collision cross sections for $[n(\text{Ser})+z\text{H}]^{z+}$ clusters presented by Clemmer *et al.*[131] (references to included figures in brackets)

a: Number of monomer units contained in the cluster.

b: Net charge state of the cluster.

c: Experimental collision cross sections. Uncertainties given in parentheses correspond to one standard deviation about the mean for replicate measurements.

d: Concise description of the model geometries. Numbers and letters in parentheses indicate the section of each figure in which the geometry is shown.

e: Collision cross section calculated for model geometries using the trajectory method (see ref. 14 for details). For geometries derived from molecular modelling simulations, uncertainties are reported as one standard deviation about the mean value for the twenty-five lowest energy conformers obtained.

f: Singly protonated geometry constructed based on the structure described in [127].

g: Neutral geometry constructed based on the structure described in [126]

h: Geometry generated by molecular dynamics simulations.

i: An octamer unit extracted from the L-serine crystal structure that has the lowest collision cross section of eight-serine unit slices taken from the crystal packing.

j: Geometries constructed by packing the $[8(\text{Ser})+\text{H}]^+$ block-like geometry (figure 5.4b) along the largest (11.2 x 7.2 Å) or smallest (6.7 x 7.2 AA) interface region.

Harder collision conditions than the ones for the spectra presented in figure 5.9 such as raising the temperature or the drift field result in the absence of solvent tailing and all other species than the main octamer (1) in the same time. The same result is obtained changing the drift gas from He to N_2 even at 50°C tube temperature.

Clemmer reports a general resolution power of approximately 1% for his mobility spectrometer and therefore the possibility to resolve the zwitterionic and charge solvated species with a cross section difference of 5% (framed in table 5.2).[131] But the resolution for this analyte system with the presented S/N and spectra quality shown in

figure 5.5 is questionable. Together with the previously discussed equilibration possibility in his setup a different result of our measurements could be explained.

5.3.4 Mobility Measurements on Mixed Serine Clusters

Singly or multiply substituted serine octamers at different exchange positions by other amino acids were expected to be separated by mobility measurements by protruding side groups. Such exchanges are known for alanine, arginine and threonine. The substitution by cysteine instead was expected to change the packing density of the octamer in analogy to the lower binding energy to cysteine which is known for dimers.[130]. Therefore mixing experiments with alanine (ala), cysteine (cys) and threonine (thr) of identical chirality and l-iso-propylserine (ips) and l-threo-tert-butylserine (tbs) with the same basic structure but a larger side group were performed.

The production of mixed clusters with up to 4 threonine molecules inserted in the serine octamer was successful from a 1:9 thr:ser mixture. Lower serine ratios resulted in the complete absence of octamers. The resulting ion signal yield was much lower as for the pure serine octamer under the same soft conditions. Measurements on the mass of thr_1ser_7 and thr_2ser_6 even with long acquisition loops showed only one peak at 55.0ms with a small side peak on the solvent tailing side (s. figure 5.10) which could not be assigned with confidence.

Cysteine did not show mixed octamers at all. With higher concentrations of serine only serine octamers were formed, while mixing more than 1:4 cys:ser all serine octamer disappeared at the given S/N and only ser-MeCN, cys-MeCN and cys_2 were visible in the MS.

Alanine showed almost the same picture than threonine. The unnatural amino acid l-iso-propylserine (ips) which was expected to give larger differences at the different packing positions didn't show high enough intensities on the mass of the octamer to perform mobility measurements at a usable S/N. Spectra of a 9:1 ser:tbs mixture showed even under harder desolvation conditions (peak 71.5 ms with N_2 as drift gas and 4 kV at 100°C) a broader part in the solvent tailing region than for the threonine but around 10% of noise which made an interpretation difficult. Longer averaging up to the limit which the signal stability and contamination degree allowed didn't increase the peak form resolution enough to gain more information. The obtained intensities
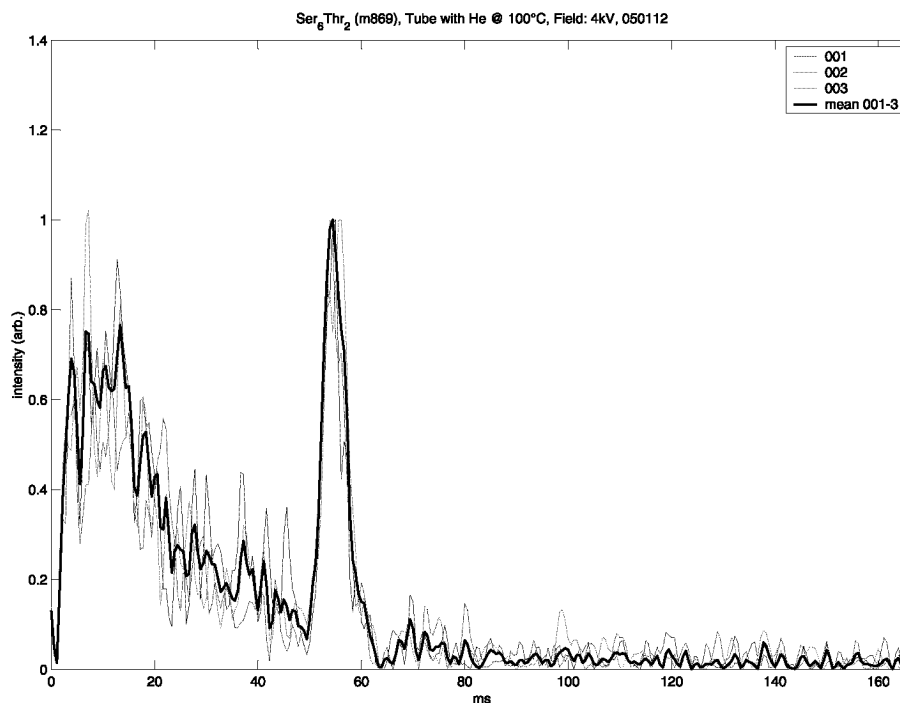
Figure 5.10: Measured FT mobility sprectra at the mass of the ser_6thr_2.
(single shots and average of 3 shots – bold line)

with the even larger l-tert-butylserine were again lower where a mobility measurement was not successful anymore.

The limit of signal intensity made further investigations in the necessary resolution difficult.

5.3.5 Conclusion

Investigations on serine octamer clusters with high resolution ion mobility on the selected octamer mass channel have been performed. With a lowered field and He as drift gas to produce soft conditions right at the border level of successful desolvation a detection of up to 8 different serine octamer species and a reasonable assignment using published collision cross sections of possible structures could be made. This differs clearly from the results of Clemmer *et al.*[131] who detected only one octamer (zwitterionic) and two higher cluster species in the octamer mass channel. The dif-

ferences could result out of possible reorganization in the ion trap storage prior to the measurement and the presented S/N in Clemmer's setup.

This agrees with the recently published flow tube and ICR stability measurement results of Lifshitz *et al.* where the gas phase stabilities of other structures than the zwitterionic are quite low, predicted to be not enough stable for high pressure high field mobility measurements due to the available collision energy even with light gases.[132] If stored in a small ion trap the clusters could undergo multiple collisions and exchange or fragment leaving only the most stable species.

Nevertheless the 8 detected species could not be proved additionally to exclude solvent clusters accidentally appearing at the same masses and cross sections as the successfully assigned serine species since they appear together with solvent tailing. Our observations agree with the published stability prediction in the range of additional solvent binding and clustering. Although an appearance of solvent clusters at several assigned serine cluster sizes is unlikely, without an additional proof the results are not fully convincing.

While the more regular zwitterionic cluster form seems to be more stable in gas phase, the higher importance in solution compared to the charge solvated like cluster type and therefore the natural role is still unclear regarding the results of Cooks *et al.*[125]

In the mixed cluster experiments the separation of clusters with one or two different exchange positions by their cross sections (outer/inner position or o-/m-/p-formation) was not successful due to low signal intensity and the concomittent resolution limits. The fact that unnatural amino acids of the same basic form with larger end groups (e.g. ips) show larger asymmetric tails at the same position under even harder conditions could be a hint for a reasonable difference in cross section which could not be separated because of either not high enough resolution or fast internal rearrangement in gas phase induced by collisions with the tempered drift gas. Probably an ion transmission increase of at least a factor of 10 due to changes on the setup could allow measurements (at several different temperatures) to exclude or verify the latter effect and probably also to enable the separation of the different species.

5.4   Conclusion – General Remarks

In the current chapter two selected partly successful measurement projects were discussed. Nevertheless many projects were performed which were not or only partly successful. Most of the negative results can be explained with chemical or technical issues fitting well to recent publications in the appropriate field.

The positive aspect on the negative results was the output of ideas for technical improvements on the current setup. Nevertheless it was not possible to practically implement them yet in the scope of this dissertation. A summary of these ideas is discussed in the general conclusion and outlook chapter 7 for the mobility part of this thesis.

Chapter 6

Structural investigations on DCC Quenched Zr-Ar Ethylene Polymerization Products – Direct Observation of Branching Ratios

Summary

In this chapter a successful application of the current ion mobility setup for the direct investigation of branching ratios on DCC quenched ethylene polymerization products is presented. The behavior of the collision cross section of the branched versus the linear products was determined by well agreeing calculations and measurements on model compounds. Additionally a direct determination of the chain walking or branching ratios by peak form analysis is described.

6.1   Introduction – Zr-Ar Ethylene Polimerization

The DCC quenched ethylene polymerization products were produced by Fabio Dilena with whom this work was done in collaboration on this chapter.

The direct oligomerization of the cheap source ethylene is nowadays the predominant route to higher α-olefins which are in chain lengths of C4-C18 of high importance for the chemical industry as they are highly valuable and versatile feedstocks and building blocks for a variety of refining processes. They are of wide interest as monomers, comonomers in catalytic olefin polymerization and many functionalized products. A variety of catalysts are known to actively promote the oligomerization of ethylene while the majority of them afford a mixture of linear α-olefins having different chain lengths usually in a Schulz-Flory distribution.[133] The selective oligomerization to yield a specific higher linear α-olefin is highly desirable, as it provides the wanted α-olefin in highest amount, while circumventing the separation. On the other hand selectively long chain or highly branched oligomers are also of interest for other applications.[134–137] Therefore, extensive research is underway using metals from across the periodic table. In particular, Ti and Zr, early in the transition series, and Ni and Pd, among the late transition metals, form complexes that show promise as cheap, selective catalysts. Nevertheless the detailed mechanisms and kinetic behavior of the processes is still unclear. This makes a rational selectivity development impossible. Beside the highly important alkylaluminium activated Ziegler–Natta type TiCl_3 and the Brookhart type Ni– or Pd– diimine catalysts a new class of promising highly active Zr–metallocene/MAO catalysts were discovered by several groups in 1994.[138] Just as with the Ti–based catalysts, they are prepared usually in the [(L)ZrCl$_2$] (L = cyclopentadienyl or substituted cyclopentadienyl) form and activated by MAO or another alkylaluminium expected to exchange chlorines by alkyl chains. These catalysts showed important non trivial temperature dependencies.[134]

Therefore a MS investigation project on the Zr-Ar catalysts was started recently in our group by Fabio Dilena and Esther Quintanilla where kinetic differential equations containing multiple parameters are fitted to the polymer distribution obtained in the MS spectrum and to the time dependent ethylene uptake at different temperatures and pressures.[139] Nevertheless the branching ratio as important parameter is not accessible with this method. The branching ratios are still difficult to ascertain reliably for

this type of catalysts. Branching is routinely determined by GPC investigations which requires very well characterized material standards which was done in the past for investigations on nickel catalysts in our group. More reliably, branching is determined by $^{13}C\{^1H\}$ NMR spectroscopy. Both methods, however, measure the aggregate branching over all oligomers or polymers. This was expected to be a good application for ion mobility which additionally has the advantage to be size-selective in the determination of branching, which is not the case for the current methods.

6.2 Quenching Experiments with DCC and ESI-MS

The polymerization reactions were carried out in a pressure tube similar to the one described for the iridium project with constant concentrations of 4 mg of the Zr–Ar catalyst in 6 ml of toluene and different defined temperatures. The toluene was preloaded by 12 eq of MAO in relation to the the catalyst and saturated at 1.5-2.0 bar of absolute ethylene pressure before the catalyst was added.

exo   endo   asym
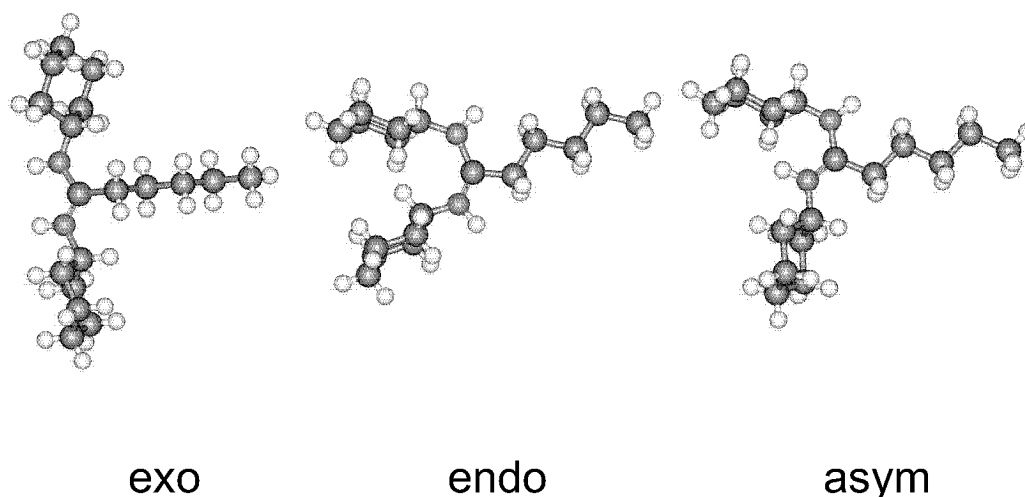
Figure 6.1: Three different isomers of the DCC bound chains.

After the catalytic ethylene oligomerization reaction at defined pressure, temperature and reaction time the reaction was quenched upon addition of 25 eq DCC (dicyclohexyl carbodiimine) trapping the oligomer chain from the catalytic side as a zirconium

amidate, which upon workup is protonated to the neutral amidine. To be observed in the ESI-MS it is further protonated to an amidinium cation which is facile due to the high basicity of the amidines. This methodology was recently published by Fabio Dilena and Ester Quintanilla.[139]

Principally three different isomers of the amidines exist (s. figure 6.1). Because of the equivalent of amide resonance, the three structures do not interconvert unimolecularly readily at ambient temperature:

- exo,exo – short label: exo

- exo,endo – short label: asym

- endo,endo – short label: endo

The quenching process is expected to form mainly the all exo structures shown in figure 6.2 if the geometry of the initially-formed zirconium amidate is preserved upon protonation. They should differ sufficiently by collision cross section due to the different bound chains, even with the large end group.
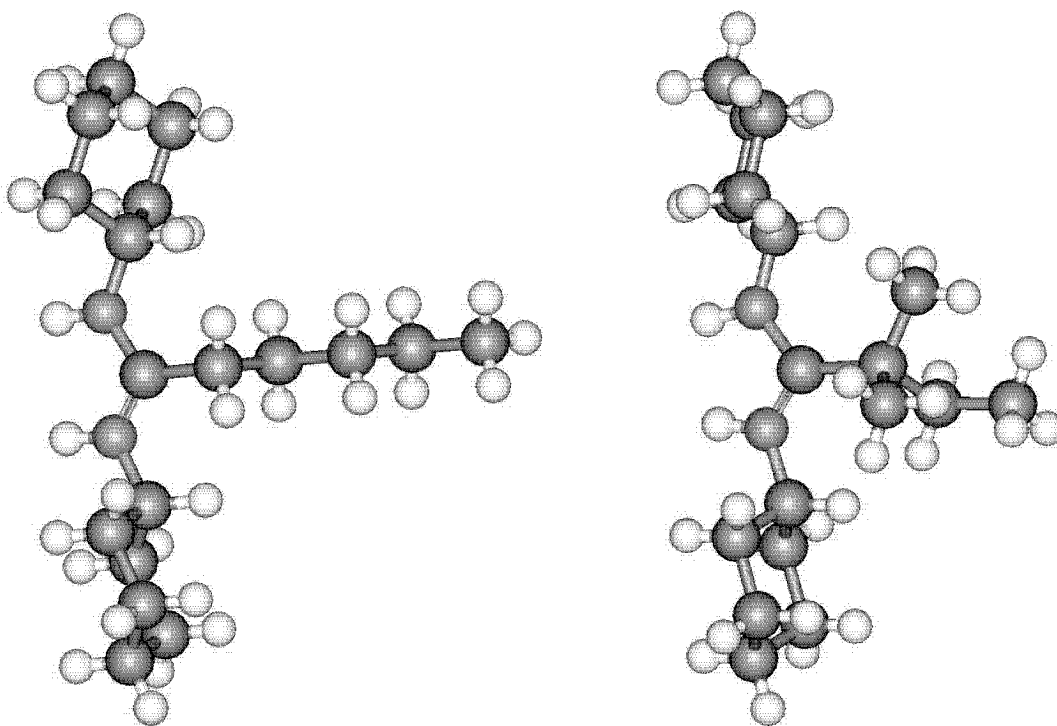
Figure 6.2: Branched and unbranched structures of the DCC–C5–chain.

The MS spectra showed a clear temperature dependence of the product species. While at 0°C only odd chains (C3,5,7,...) are observed higher temperatures yield in an increasing amount of even chains (C2,4,6,8,...). At a temperature of 60°C the amounts are comparable. Later measurements at 120°C showed a continuing trend of building only even chains (s. figure 6.3). The dominance of different possible mechanistic routes seem to drastically change temperature dependent.
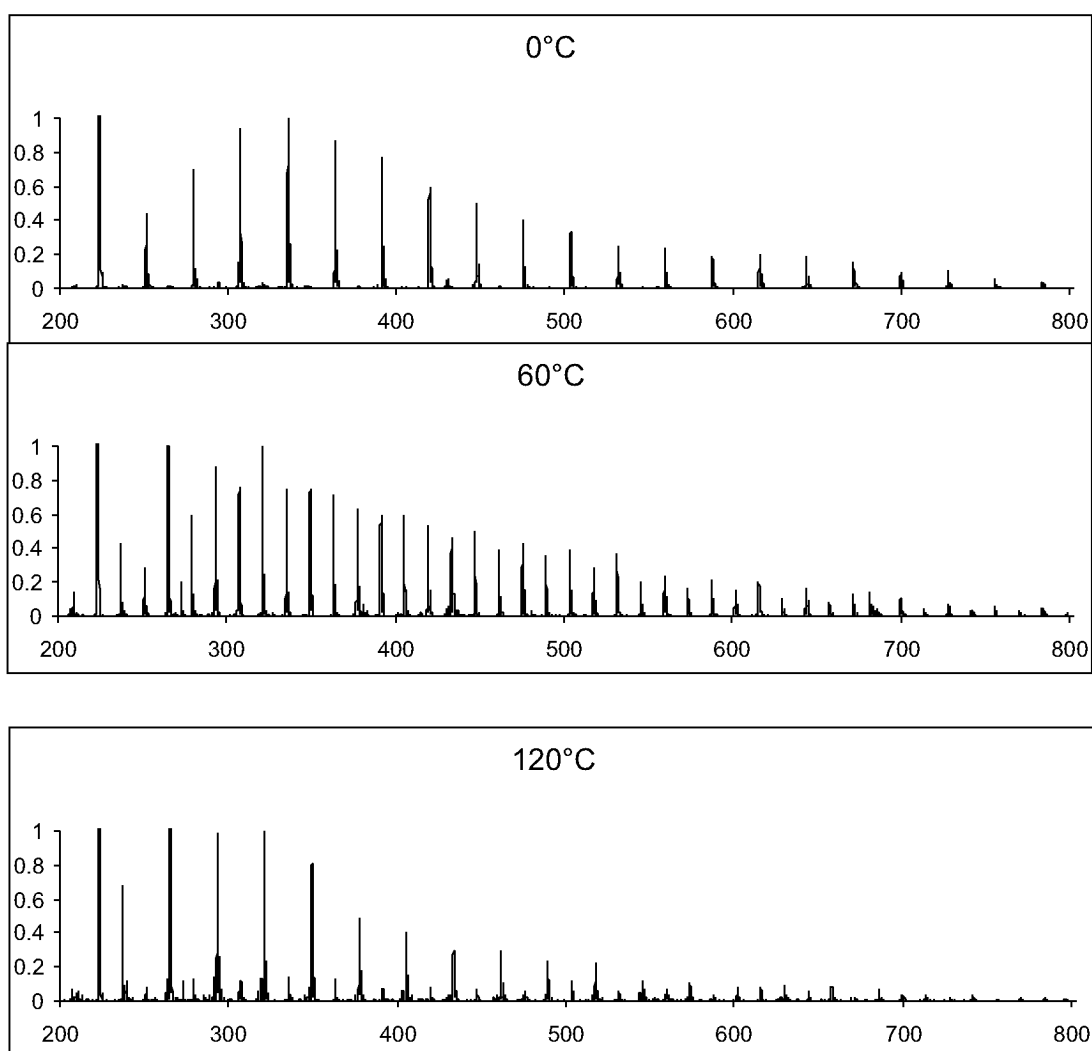

Figure 6.3: DCC quenched ethylene polimers in CH_2Cl_2 solution produced at different temperatures with a Zr-Ar complex.

6.3 Model Compounds

To simplify the access of a complete set of structures the focus was reduced to the C5 to C7 chains. Branched structures can principally appear due to chain walking of the catalytic center which occurs by a sequential 1,2-(beta hydride)-elimination followed by a 2,1-insertion. Because the zirconocenium hydride-olefin complex is also an intermediate in one of the possible chain transfer mechanisms, it is likely that the appearance of even chains is associated with branched chain products as well. However, there is more than one mechanism for chain transfer, so transfer and branching may not track completely in parallel.

While for the C5 chain 7 structures are possible the number for C6 chains increases to 18. If the chain walking can only occur after the first ethylene insertion building a C4 chain it can occur in total on only 2 steps but in multiple number which ends up in 7 relevant structures shown in figure 6.4. To evaluate the separation ability of our ion mobility setup a set of model compounds was created by quenching MgBr–Grignard solutions with DCC.
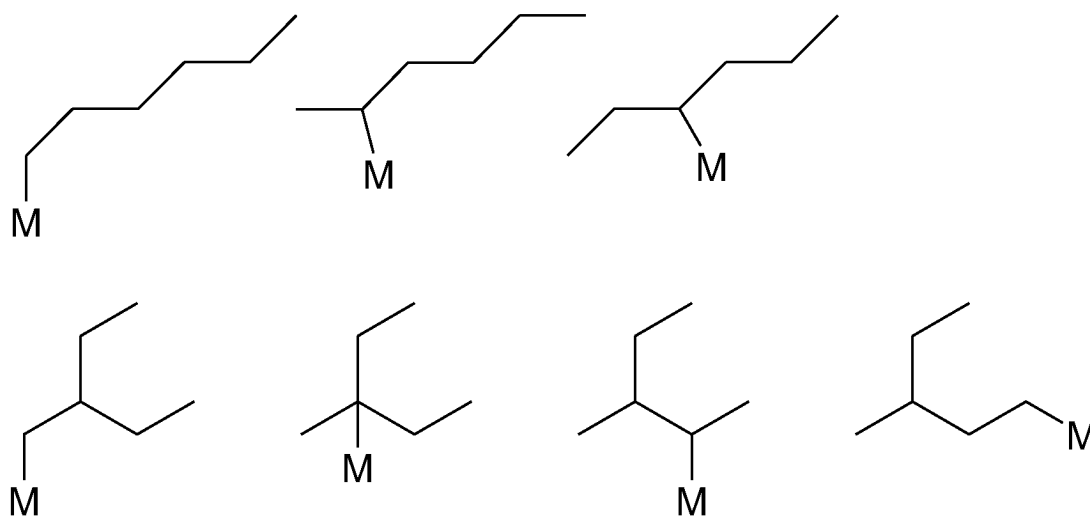

Figure 6.4: Possible structures of DCC quenched polymers: Branching and chain walking products.

6.4 Calculations with Mobcal

A complete set of all structures for the DCC coupled C5 and C6 chains in the all exo form was calculated using PM3[116] and as control calculations B3LYP/6-31G[118] DFT structure optimizations using Gaussian03[119]. Also 5 structures for the C7 chains were calculated to get investigate the trends for larger chains. For resulting structures (single structure) calculations with MOBCAL were made. The resulting mobilities were visualized relative to the linear chain species (s. figures 6.5, 6.6, 6.8 and 6.9).
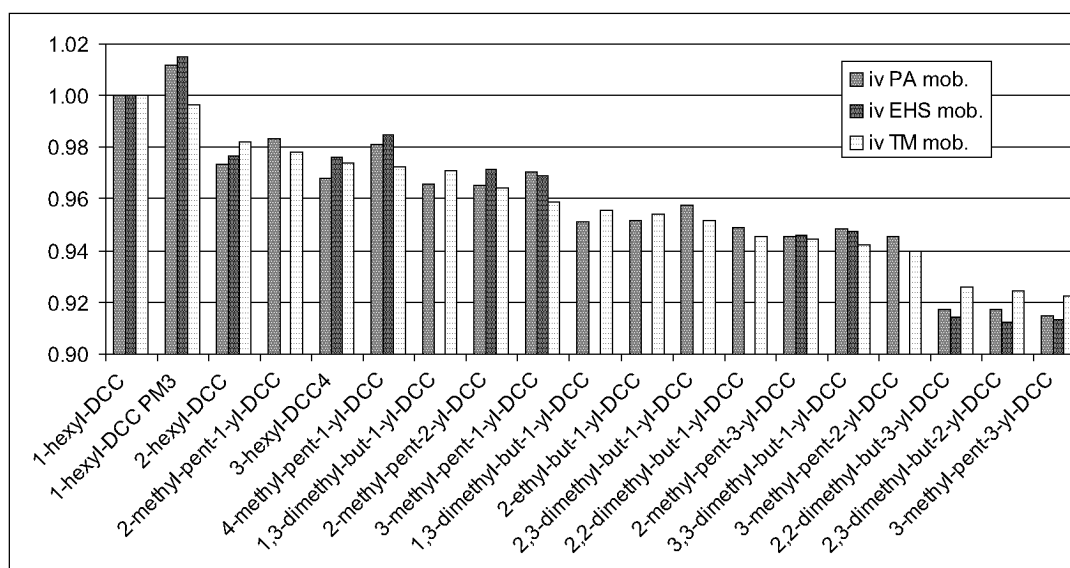
Figure 6.5: All possible C6 structures.

A clear trend for all the branched structures to have a smaller calculated collision cross section than the linear chain species in a range between 2 and 4% (8% in a specific C6 case) could be observed. The stability of the calculations and the difference of simple PM3 optimized structures versus the DFT results are shown in the figures 6.5 and 6.6 (PM3 result is marked) for the linear C6 chain resulting in about 1% of difference for the PA and EHSS model but almost none for the more reliable TM model.

The separation performance of our mobility cell allows to baseline separate ions with 6% of difference for the collision cross section as described in section 4.4. Nevertheless a mixture in the expected 2 to 4% range containing up to 7 species can be quantified by fitting to a convolution of peaks but was not expected to be well separated.
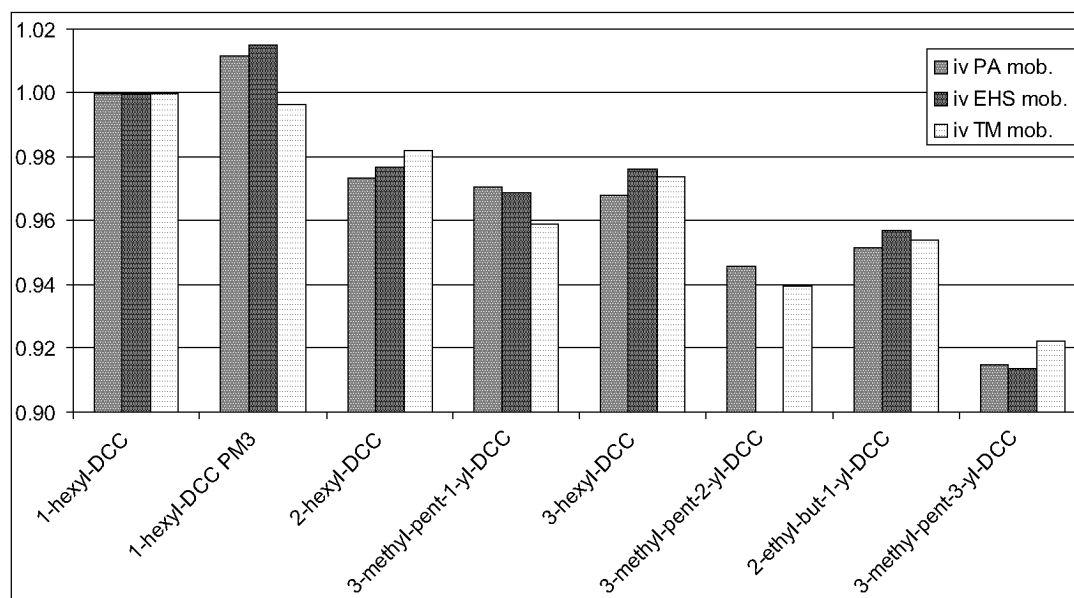

Figure 6.6: Selected C6 structures relevant for the Zr–Ar polymerization.

6.5 Experimental Results with Model Compounds

Initial mass selected mobility measurements on C5 Grignard model compound solutions of 10^{-5} M in CH_2Cl_2 resulted in spectra showing two peaks with different collision cross-sections. The larger, unexpected peak was the major species. Upon higher dilution ($< 2*10^{-6}$ M) the larger species disappeared for tube lens settings of below 30 V (s. figure 6.7). With the original 10^{-5} M solution and tube lens settings around 0 V an additional peak at an *m/z* of 593 with a broad chlorine indicating pattern appeared in the MS spectrum. A mobility measurement selecting that mass gave the same collision cross section than the larger species observed before.

This leads to the assumption that the major species in solutions up to 10^{-5} M dilution could be the chloro–bridged dimer of the desired chain which is fragmented at usual tube lens settings for the MS chain distribution experiments. In contrast the conditions in the drift tube are too soft to fragment the dimer while tube lenses above 20V form the monomer mass after the mobility detection which leads to the observed spectra.
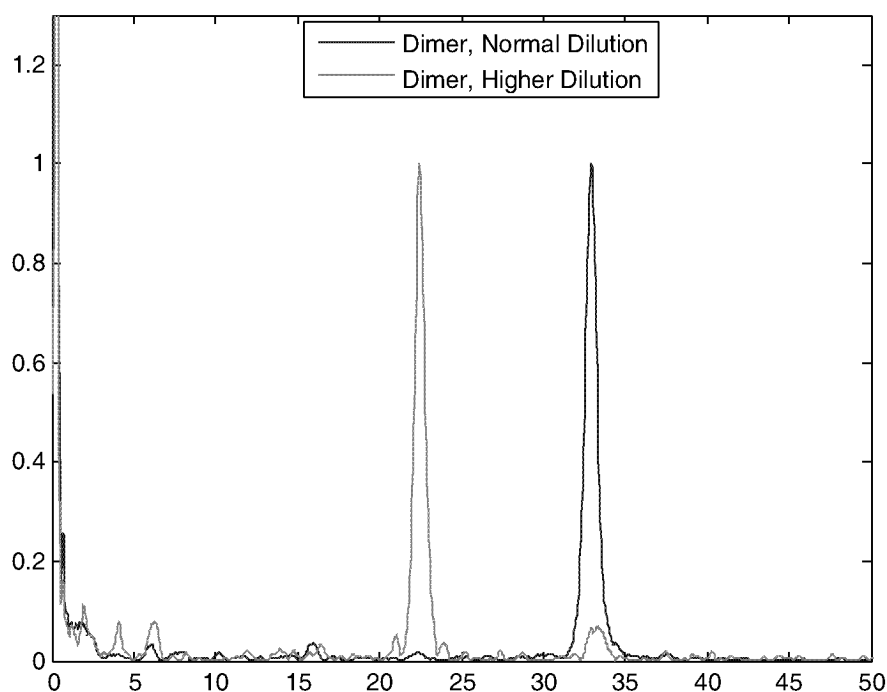

Figure 6.7: Mobility spectrum of DCC coupled C5 chains in solution: Dimer formation.

The a set of 6 C5 and 2 C7 model species were measured and the relative values compared to the calculated cross sections (s. figures 6.8 and 6.9). While the collision cross sections of the C5 species with a branching index of 1 to 2 fit the calculations well, the ones with higher indexes were systematically lower than the calculations by 3 to 4%. But the important trend of all species being smaller than the linear product was verified. For the C7 chain products the measurements fit the calculations better.
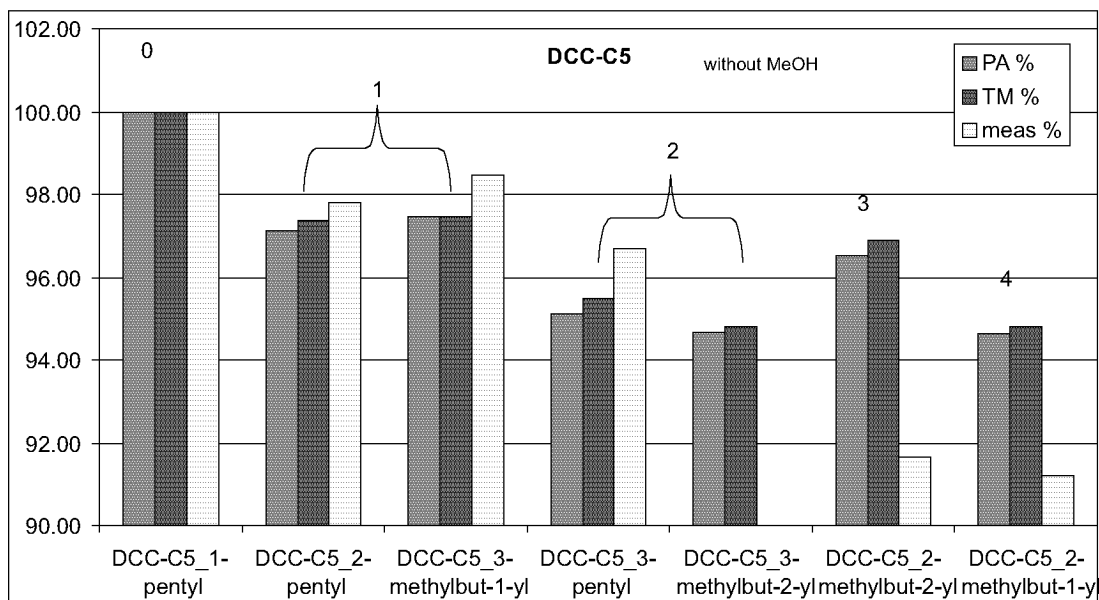
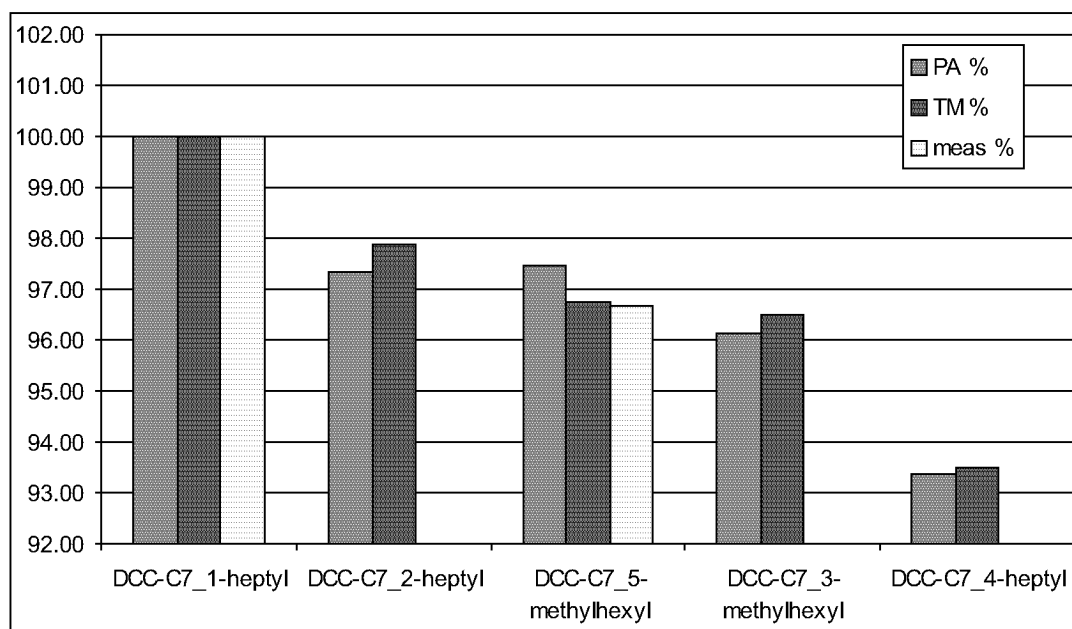**Figure 6.8:** Complete set of the C5 structures.

Figure 6.9: Several examples of the C7 structures.

6.6 Results on the Polymerization Products

6.6.1 Model Compounds vs. Polymerization Products

Measurements of the DCC quenched polymerization product solutions (0 and 60°C) at the mass of the C5 chain gave the same concentration and tube lens dependent monomer–dimer formation results than the model compounds in CH_2Cl_2. A closer look to the main peak of the monomeric species showed surprisingly a drift time of 22.00 ms instead of 22.75 ms which is about 3% smaller in collision cross section. Therefore either a different main isomer is built during the quenching of the Zr–Ar polymerization than during the quenching of the Grignard compounds or almost all polymerization product is branched which is presumably unlikely.

The calculated collision cross section of the asymmetrical isomer of the C5 chain by the expected 3% larger than the exo isomer for the most reliable TM method which fits perfectly with the measurement results. After several exchange tests with cyclohexylamine and polar nucleophilic solvents an addition of ca. 10% of MeOH to the 10^{-6} M CH_2Cl_2 solution of the model compounds resulted after a reaction time of 10 min to the desired shift of 3%. In figure 6.10 the relative collision cross sections of the original CH_2Cl_2 measurement of the linear product and 3 species treated with MeOH are compared to the assigned calculated isomers. The well fitting calculations and measurements showed that there is almost no difference in collision cross section of the different isomers of the highly branched products in contrast to the linear species. This corrects also the systematically too low relative cross sections of the highly branched species discussed before.

To validate the hypothesis that the differences in cross-section are caused by differences in isomer content, a time dependent measurement of the unbranched C5 model compound after addition of MeOH was made. The collision cross section showed the expected time dependent behavior switching to the desired product. As additional comparison the polymerization product at 60°C is shown, which has the same position but is substantially broader (s. figure 6.11).
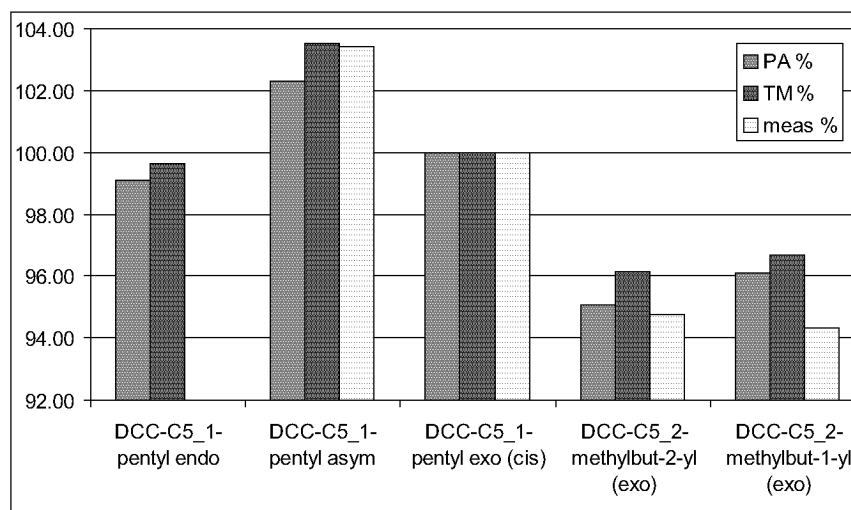
Figure 6.10: Calculations and measurements on the different conformers of the DCC bound chains.
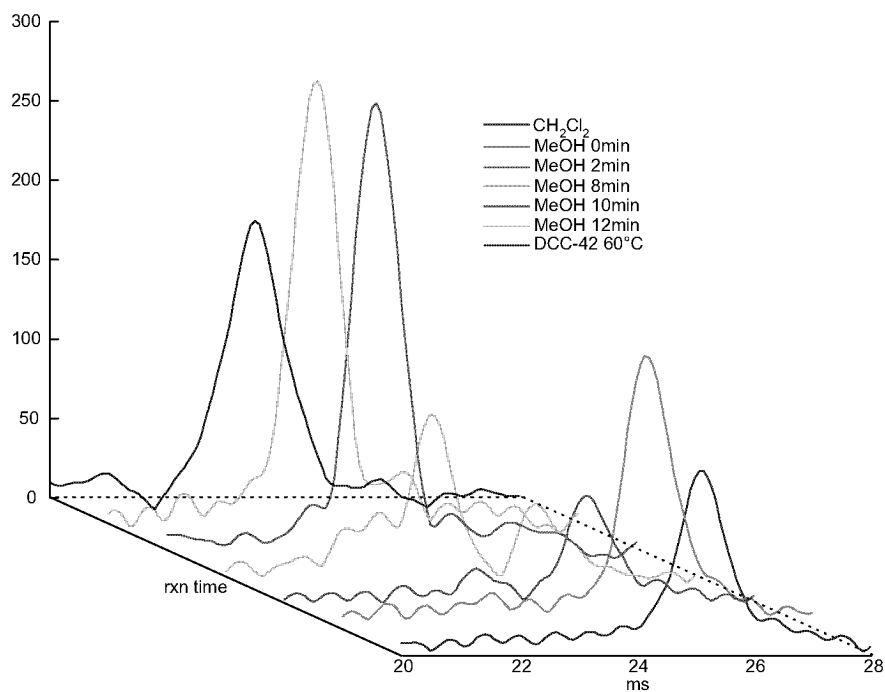

Figure 6.11: Time dependent mobility measurements before and 0, 2, 8, 10 and 12 min after the MeOH addition and comparison to the 60°C polymerization product (5.35kV drift field).

6.6.2 Peak Integration and Ratio Calculations

To calculate the branching ratios out of the peak form of the measured spectra on the polymerization products a reliable integration method for the different regions of the peak has to be taken. The simplest one of floating integration and measurement of the resulting steps like for NMR spectra has a reliability problem if the peaks are completely attached together as in the current measurements. A more advanced method fitting 2 to 3 gaussian peaks for the main groups of the present species should produce in a more adequate result (s. figure 6.12).
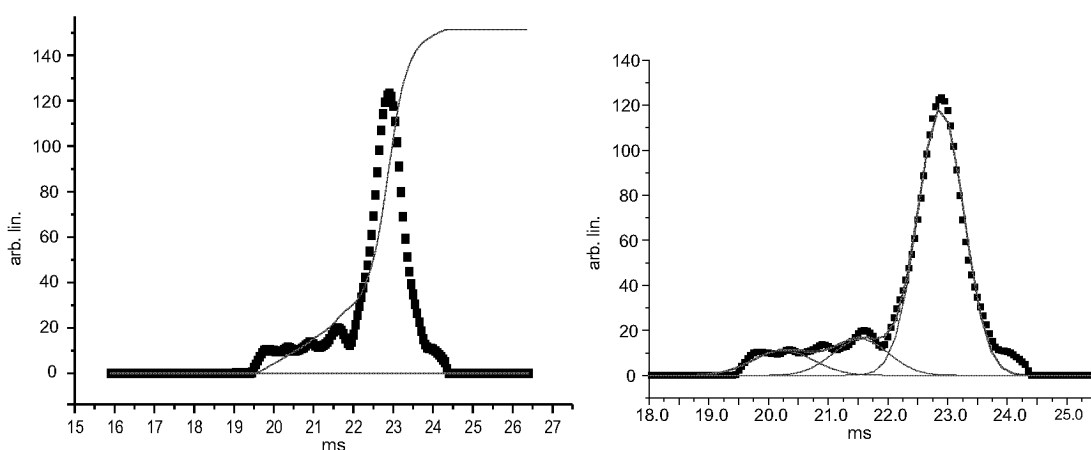

Figure 6.12: Integration – "NMR type" (right) vs. Fitting 3 Gaussians (left).

The complete measured set at standard settings and 6 kV of drift field voltage resulted for the three selected solutions (0, 60, 120°C) in reasonable peak forms for the C5 and C6 species with an increase of the branching ratio with increasing temperature. Due to an interference artefact appearing between 20 and 22 ms drift time (presumably power line interference) a reliable integration was not possible. Due to its appearance out of phase with the single sweeps it could principally be discarded during the spectra workup by weighted averaging of the different sweeps.

Additional measurements at 5.35 kV shifting the desired peaks to a higher drift time finally gave more reliable artefact–free spectra. The reaction temperature dependence (polymerization) of the species on the lower collision cross section side of the peak was also present in this data set (s. figure 6.13). A small solvent tailing on the opposite peak side appeared which can be explained by slightly softer collision condi-

tions due to the lowered field and therefore less desolvation at the same temperature. As expected the solvent tailing remained constant for the different samples.
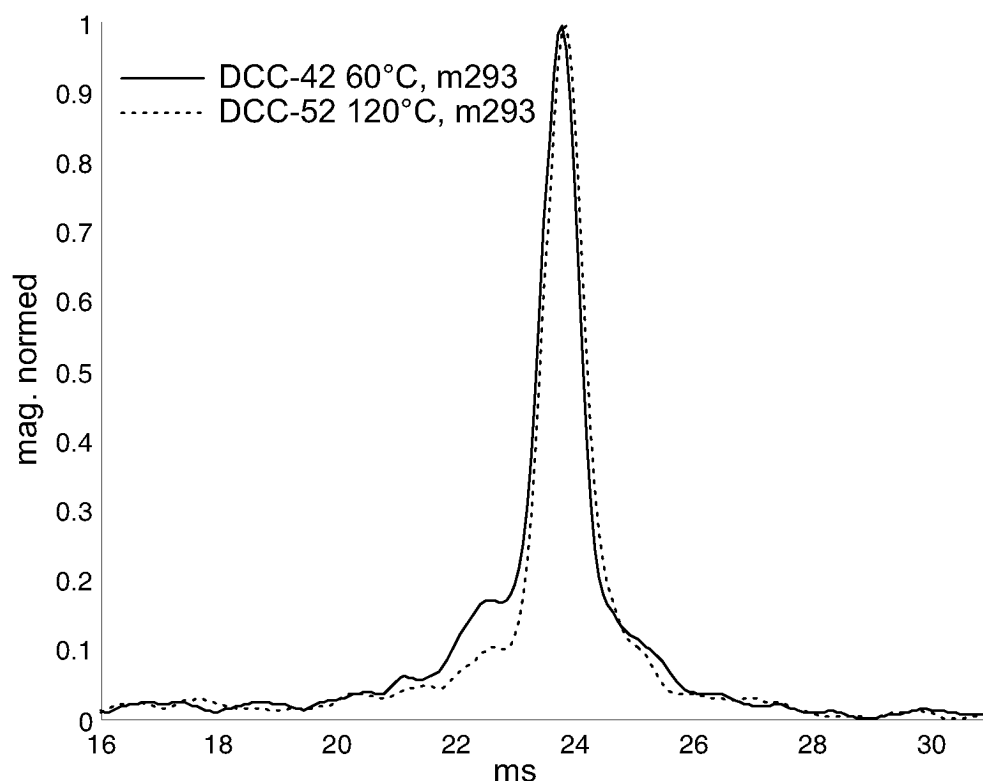

Figure 6.13: Polymerization samples at 60 (...) and 120°C (–)
average of multiple sweeps.

The peak forms were integrated with Origin[140] fitting 1 to 3 gaussians depending on the peak form resulting in a branching percentage. The branching can take place as chain walking process after the second insertion of ethylene which could be basically once for the C5 and twice for the C6 chains. The assumption that the back–reaction to the unbranched species has given the low extent of branching under these conditions was taken. The walking rate constant was presumed to be independent of extent of prior branching. Multiple chain walking steps were treated as a single branching step because any further branching subsequent to an initial one produces branched chains which are not further separated in the mobility spectrum. This results in the kinetic reaction scheme 6.1 and the rate formulations for the different reactands shown in equations 6.6.2 to 6.6.2.
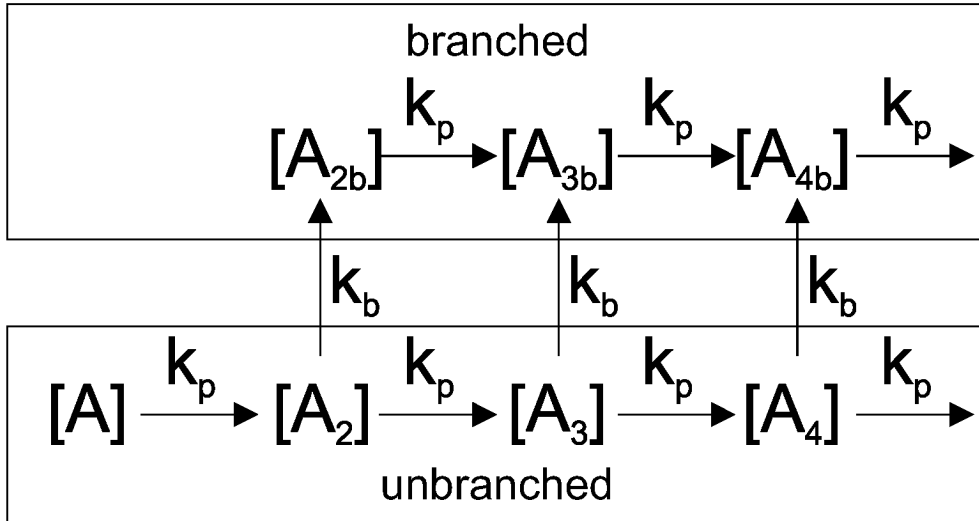
Scheme 6.1: Kinetic reaction scheme of the polymerization process.

$$\frac{d[A]}{dt} = -k_1[A] \tag{6.1}$$

$$\frac{d[A_2]}{dt} = k_1[A] - k_1[A_2] - k_2[A_2] \tag{6.2}$$

$$\frac{d[A_{2b}]}{dt} = k_2[A_2] - k_1[A_{2b}] \tag{6.3}$$

$$\frac{d[A_3]}{dt} = k_1[A_2] - k_1[A_3] - k_2[A_3] \tag{6.4}$$

$$\frac{d[A_{3b}]}{dt} = k_2[A_3] - k_1[A_{3b}] - k_1[A_{2b}] \tag{6.5}$$

k_1 is the propagation rate, k_2 the branching rate, A_n the nth chain polymerization product and Anb the related branched product. Assuming stationary concentrations for A_2, A_{2b}, A_3 and A_{3b}, the concentration ratio $b = A_3/A_{3b}$ results out of equations 6.6.2 to 6.6.2 as follows:

$$b = 2 \cdot \frac{k_2}{k_1} + \frac{k_2^2}{k_1^2} \tag{6.6}$$

Formulating a branching ratio $K = \frac{k_2}{k_1}$ equation 6.6.2 can be further reduced to:

$$b = 2 \cdot K + K^2 \tag{6.7}$$

Therefore the total branching or chain walking ratio K is defined by:

$$K = \sqrt{1 + b} - 1 = \sqrt{\frac{c_{total}}{c_{lin}}} - 1 \tag{6.8}$$

where c_{total} is the total amount of product and c_{lin} the remaining unbranched part.

This results in the values shown in table 6.1. For the C5 chain the mechanism is unknown. If the methyl group is inserted at the end of the mechanism it can be described as an insertion ratio at a so called branching position. If it is inserted at the beginning the chain walking step can appear one step earlier than described above which leads to one insertion step more. The result of this assumption is marked in table 6.1 with "ass. 2".

Fitting results

sample	rxn temp.	*m/z*	peak pos.	area	area [%]	K [%]
DCC-38	0	279	23.74	1.232	100	**0**
DCC-42	60	279	23.57	1.040	91.43	
			22.20	0.097	8.57	**8.57**
					(ass. 2	**4.20)**
DCC-42	60	293	23.85	0.916	92.69	
			22.44	0.072	7.00	**3.44**
DCC-52	120	293	23.79	1.228	76.76	
			22.29	0.151	9.45	
			21.25	0.221	13.79	**11.01**

Table 6.1: Fitting results of the 5.35kV data set using 1 to 3 gaussians.

The activation energy (E_a) for the branching step would be around -19.3 kJ/mol (Arrhenius–plot of DCC-42 and DCC-52). With this E_a x of the DCC-38 would be around 0.8% and therefore only 0.4% branched product could be detected which is obviously too less to be treated with peak form integration.

6.7 Conclusion and Outlook

The current ion mobility cell was applied successfully to structural investigations on Zr–Ar/MAO ethylene polymerization products. Branching ratios could be determined for the DCC quenched polymerization products for three main conditions of the reaction. The method could principally be coupled directly to MS polymer distribution measurements.

All branched products turned out to have smaller collision cross sections than the linear product which are therefore simple to distinguish. A large set of model compounds were measured which showed a good agreement to ion mobility calculations with MOBCAL especially for the TM method.

A clear temperature dependency of the branching or chain walking ratio was observed qualitatively and quantitatively. A simplified formulation of the branching ratio was formulated for the even chains while for odd chains the number of branching steps possibly requires additional investigations.

Due to the collision cross section difference of the branched product species to the linear species of only 2 to 4% the resolution was not sufficient for complete separation of the complex mixture. But the branched part could be determined by peak form analysis using gaussian peak forms for the different product type groups.

A structural difference between products formed by DCC quenched Grignard and Zr metallocene polymerization intermediates was observed. Therefore a simple workup method with MeOH was found which allowed the isomerization of the Grignard based products to the same form than the metallocene based ones. Additionally the products present in CH_2Cl_2 solution were determined to be more likely weakly bound chloro bridged dimers than monomers of the DCC ended oligomer chains. The dimers are usually fragmented by the tube lens in MS investigations.

Outlook

Based on this results further investigations on the Zr–Ar polymerization could be done. A numerical modelling of the branching ratio coupled to results of polymer distribution measurements by MS and ethylene uptake measurements could be done to provide a more complete picture of the reaction mechanism and to gain absolute branching ratios instead of the discussed relative ones. The method possibly also allows similar

polymerization systems to be investigated.

To improve the separation the quenching could also be made with DMC (dimethyl carbodiimine) and DEC (diethyl carbodiimine). The resulting smaller end groups could possibly increase the relative differences in collision cross section by the different oligomer chains.

Chapter 7

General Conclusion and Outlook for Ion Mobility Projects

A successful application of ion mobility measurements for a large number of different chemical investigations have been presented in this work. Nevertheless the result of many project ideas was not spectacular enough to be published or negative in the meaning of additional separation abilities or detection of multiple species. There are still numerous ion mobility project ideas which can be investigated in advance with the current setup. Especially direct measurements of geometrical differences as cis/trans configurations or o/m/p binding positions on organometallic compounds have still a lot of potential for future projects.

As also demonstrated in this work the current setup can be used for further investigations on important projects in the group (e.g. branching ratios,...). A change to our SSQ710 could increase the spectra quality and possibly make also the fast one gate method available.

A possible application to an ion trap was shown recently by Hill *et al.*[113] disabling the auto gain correction. This could also be an interesting feature needing only small changes on the drift tube back plate.

Redesign of the Mobility Cell

Some projects like the Pd–allyl project showed the need for mobility measurements at reduced temperatures which is only possible with a decoupled desolvation region. This would allow a much wider range of temperatures for the mobility measurements to be accessed.

For other projects better resolution could increase the reliability of the measurements. Recently several groups reported an increase in resolution by more than a factor of 4 applying voltages of up to 12.5 kV instead of the originally 4-6 kV to the main drift region, while Jarrold[12] discussed already 1997 a high resolution at 14 kV:

pressure	tube voltage	lenght	V/cm	td/Δt	lit.
150 Torr	10.0 kV	58 cm	170 V/cm	120-150	[51]
760 Torr	12.5 kV	30 cm	417 V/cm	156	[113]
500 Torr	14.0 kV	63 cm	222 V/cm	190	[12]

**Table 7.1:** Different high resolution setups discussed in literature.

Also the lowering of the temperature has been discussed theoretically to increase the resolution as well as the length of the drift field.[141] The reported resolutions of up to 190 ($t_d/\Delta t_{fwhm}$), which is about 160'000 theoretical plates, are coming close to the range of GC and HPLC methods (200-300'000 plates).[113] Important advantages over these methods are still the accessibility of drift time prediction and the lower needed time per measurement run. This underlines the possibility of future applications for ion mobility.

The pre–selection or storage of ions to increase the available ion signal or to make more advanced investigations would need a quadrupole ion trap or linear quadrupole at the entry of the mobility cell. An additional ion signal intensity improvement could also be achieved using an ion funnel at the exit of the drift tube.

The higher voltages shown in table 7.1 could principally applied to the current ring stack of our setup but the insulation of the housing and the electronic setup have to improved. The simple elongation of the drift region seems not to be one the most important key issues as shown in table 7.1 It would bring no more than a modest improvement in resolution but nevertheless cost signal intensity.

A temperature decrease requires the discussed separation of desolvation, possibly by advanced techniques as the *heated capillary technique*. This is only applicable if differential pumping is applied which is also needed for additional ion processing devices. An important issue in this case is, that the operation pressure of the drift tube for high resolution should still to be in the 100-300 mbar range.

A major redesign of the mobility cell is needed for almost all of the discussed improvements above. This was not possible within the limits of a dissertation project of one person but could be a good project for future dissertations. For a proposed redesign the main ring stack, the gates, the entry and exit grid, the resistors and and the heating cord can be reused. A sketch of a processable new setup can be found in scheme 7.1 using a mid pressure range of 100–300 mbar. It can be pumped by an additional rotary vane pump using an additional skimmer for a second differential pumping step entering the TSQ or SSQ (both have identical entries). The interfaces can be built with standard tube fittings as the 24–pole is added to our modified TSQ 700. Additional improvements are only two remaining holes in the glass insulation with all high voltage wires connected through the front entry. This turned out to be one of the most important practical issues during the past years of application.
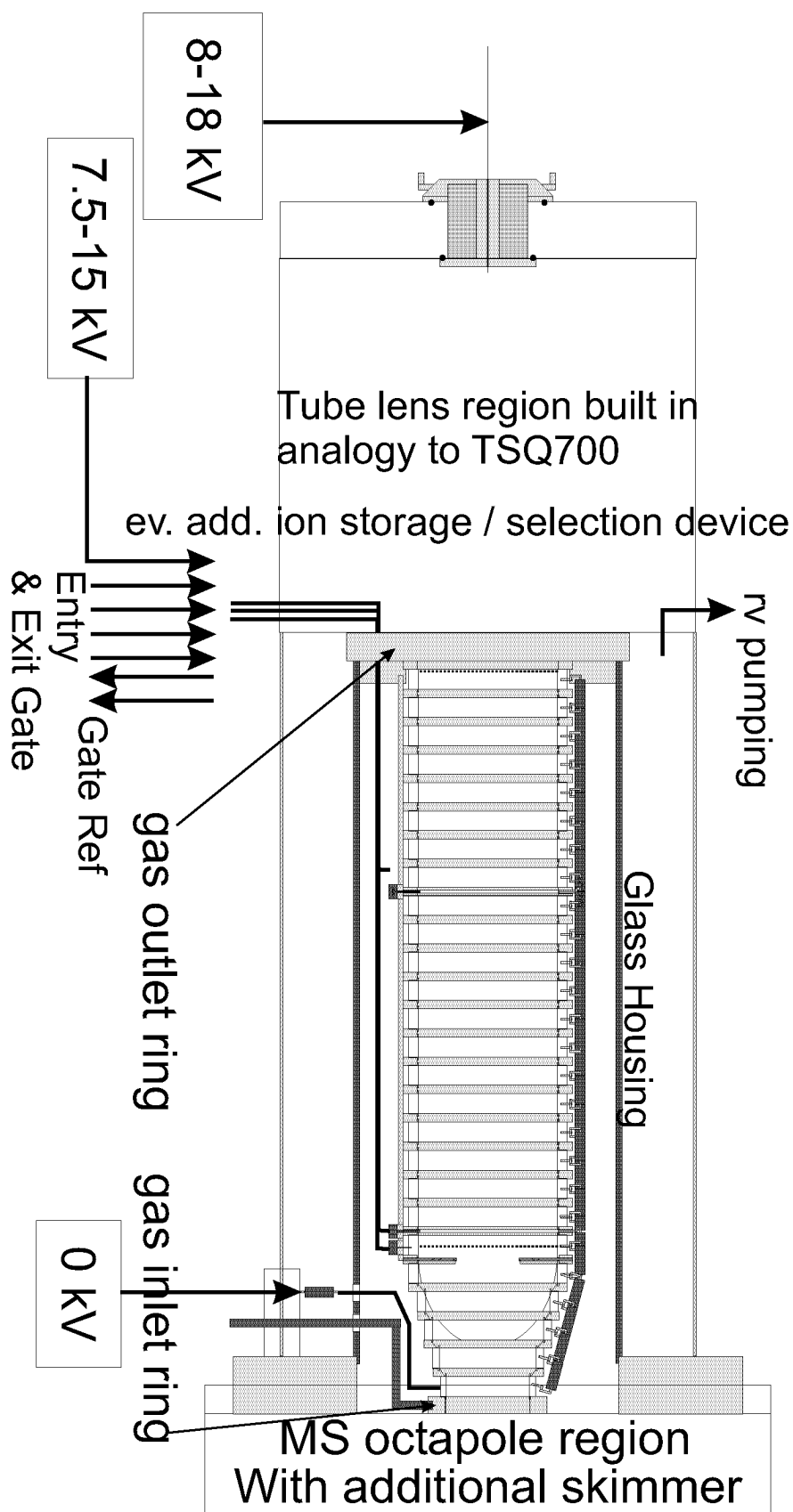
Scheme 7.1: Presumed major redesign of the drift tube keeping the main ring stack, gate and ring design.
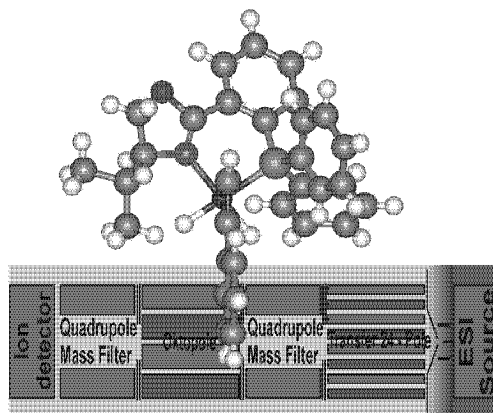
Part II

Mechanistic Studies within an ESI-MS Spectrometer

Chapter 8

Gas Phase Reactions of the

$[Ir(PHOX)L_2]^+$ Ion

Olefin-Hydrogenation Catalyst

Support an Ir^I/Ir^{III} Cycle [30]

Summary

Weighing up mechanisms: Using mass spectrometry (see scheme) gas-phase reactions of ions containing the Ir(PHOX) fragment are used to explore mechanistic pathways in the catalytic hydrogenation by related complexes. The reaction indicate that the hydrogenation proceeds by an $Ir^I/$ Ir^{III} rather than by the previously proposed $Ir^{III}/$ Ir^V polyhydride route. (Published 2004 in Angew. Chem. Int. Ed.[30])

8.1 Introduction

Since the introduction and elaboration of homogeneous catalytic hydrogenation, much work has been devoted to asymmetric hydrogenation by well-defined organometallic complexes. A particularly efficient example is the $[Ir(PHOX)(COD)]^+$ X$^-$(PHOX = chiral phosphinooxazoline ligand,[142] COD = 1,5-cyclooctadiene, X = weakly coordinating anion), complex, e.g. 1–BArF (BArF = tetrakis-(3,5-di(trifluoromethyl)phenyl)-borate), from Pfaltz and coworkers.[143–146]
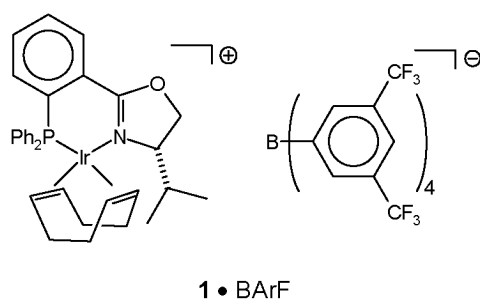

1 • BArF

Figure 8.1: $[(PHOX)Ir(COD)]^+$ X$^-$: **8–BArF**

This class of catalysts, developed from Crabtree's achiral Ir(phosphine)(pyridine) complexes,[147] (s. figure 8.2) shows exemplary properties in the asymmetric catalytic hydrogenation of unfunctionalized olefins under mild conditions. Turnover numbers (TON) and turnover frequencies (TOF) of > 5'000 and 5'000 hr^{-1} with enantiomeric excesses (*ee*) > 95% have been reported for olefinic substrates lacking the usual secondary binding moities. Given this background, the paucity of mechanistic information on the catalytic cycle and reactive intermediates is surprising. Recently, a computational study of a truncated model complex by Brandt, Hedberg, and Andersson[148] has suggested a catalytic cycle in which Ir^{III} and Ir^V intermediates play the decisive roles.
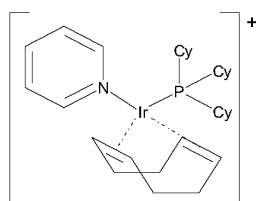

Figure 8.2: Original Crabtree catalyst.

8.2 Experimental Results

We report here an experimental investigation of the hydrogenation of styrene by the **8–BArF** by means of electrospray ionization tandem mass spectrometry which strongly suggests that, contrary to the computational study, the catalytic cycle proceeds by way of Ir^{I} and Ir^{III} intermediates, presumably via a "dihydride" catalytic cycle indicated in scheme 8.1. Buriak *et al.*[149] reported *para*-hydrogen-induced polarization (PHIP) NMR spectroscopic evidence that the "dihydride" mechanism through Ir^{I}/ Ir^{III} is in fact operative for catalysts related to **8–BArF** but the experiment does not prove that an alternative mechanism is not also running in parallel.
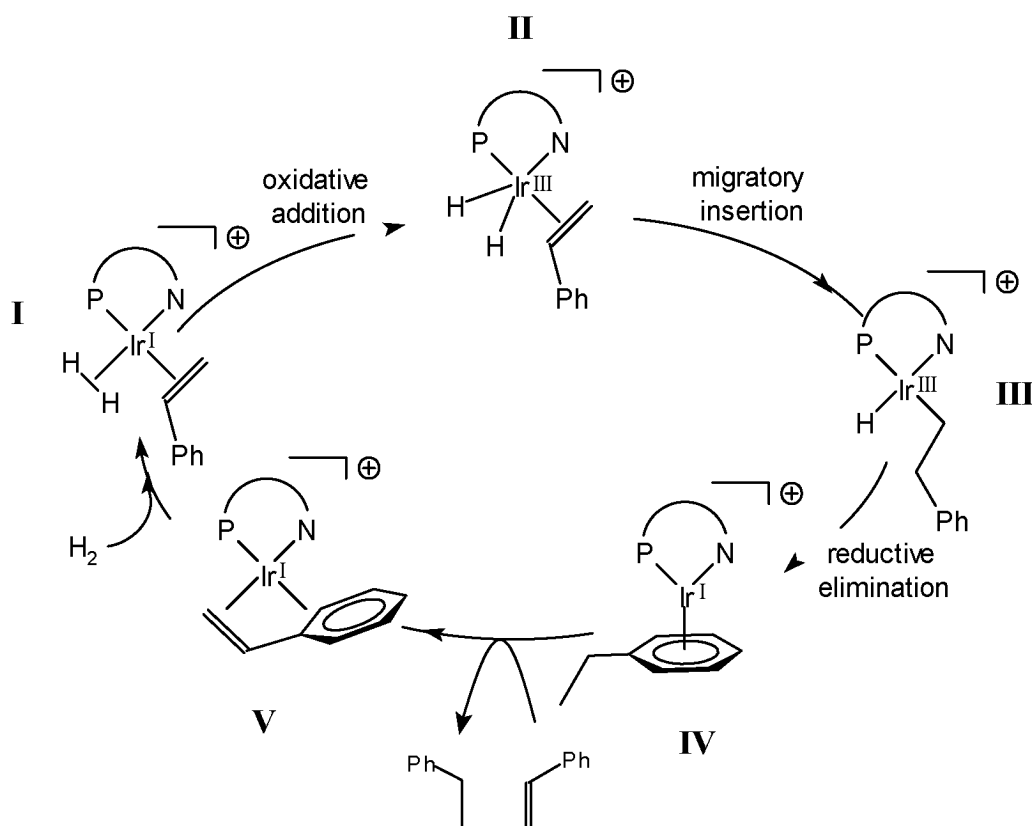
Scheme 8.1: Presumed catalytic cycle via the dihydride intermediate.

The modified FINNIGAN TSQ-700 tandem mass spectrometer has been previously described.[3–5,7,24–42] Sample introduction from pressurized glass reactors to the electro-

spray source requires a short description because previous experience in hydrogenation and hydroformylation catalysts has shown that the expected dihydrogen complexes or dihydrides rapidly lose dihydrogen once they are removed from a dihydrogen-saturated solution. In the present work, the active catalytic solution was introduced directly into the electrospray source via a fused silica capillary (150 μm x 100 cm) dipped into the solution in a pressurized reaction with the apparatus shown in scheme 8.2. The process pressure, 6 bar H_2, suffices to pump the solution ($< 10^{-5}$ M **8** and 0.17-0.26 M styrene in 5ml CH_2Cl_2, 28°C) directly into the spray tip with a flow rate of 20 μl/min. A final section of narrow-bore capillary (80μm x 17cm) ensures that there is no pressure drop with consequent bubble formation prior to the spray tip. Unless otherwise specified, reactions of selected ions are performed with close to zero collision energy with neutral reagents in the octapole collision cell at a nominal pressure of 2.5 mTorr. Previous work has shown that these conditions mean on the order of 10^4 collisions of the ion with collision/reaction gas molecules within a transit time of a few milliseconds up to 100 ms.[3–5,7,24–42]
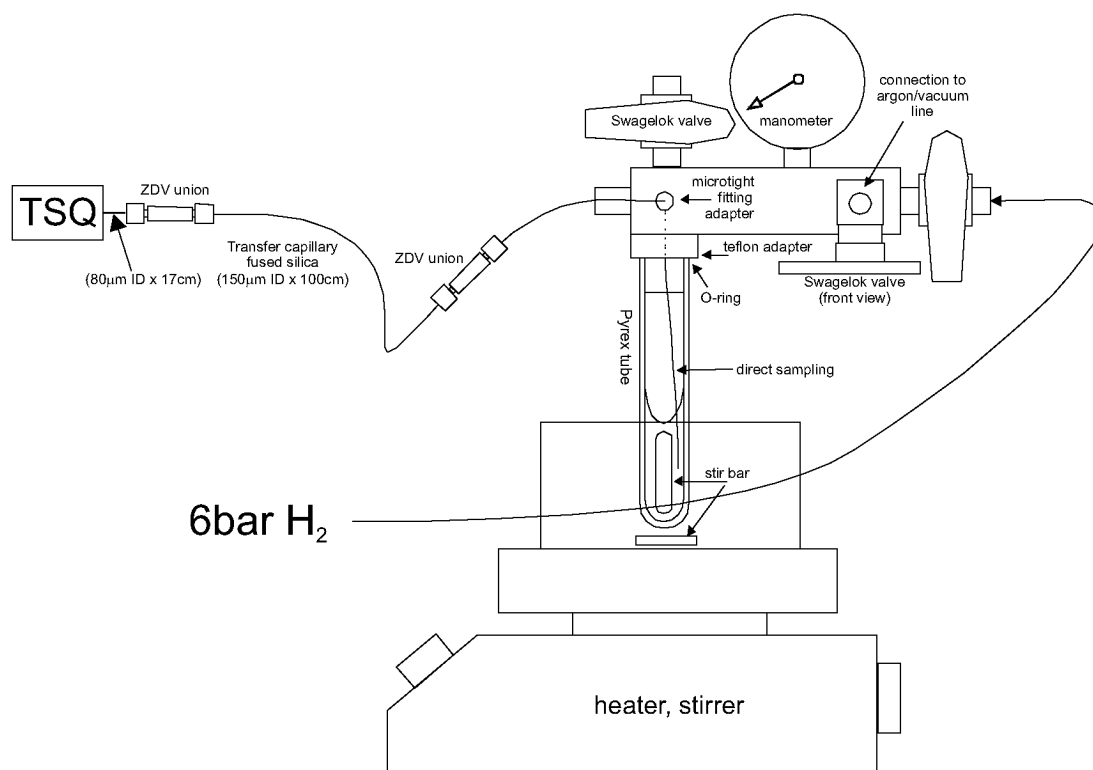
Scheme 8.2: The used pressure tube directly coupled to the ESI

Catalytically active solutions (confirmed by product monitoring) were prepared from **8**–BArF according to the literature procedure.[143–146] Sampling of the reactor when it is pressurized with inert gas produces in the electrospray mass spectrometer a clean signal for **8**, which upon addition of the approximately 20'000-fold molar excess of styrene[150] and H_2 pressure shows three new peaks (after 15 minutes), whose masses correspond to the the the compositions $[(PHOX)Ir(styrene)(H_2)_2]+$, $[(PHOX)Ir(styrene)(H_2)]+$ (species **I-IV** in scheme 8.1) and $[(PHOX)Ir(styrene)]+$ (species **V** in scheme 8.1). The mass alone, especially for the first two species, does not provide an unambiguous structural assignment, but mechanistic information can nevertheless be extracted from the experiment. The same two peaks are also very labile, with even small increases in the tube lens potential, i.e. more rigorous "desolvation" conditions, leading to loss of dihydrogen. At shorter times, i.e. < 5 minutes, other species are visible in the mass spectrum in which the cyclooctadiene moiety is not yet completely reduced. Control experiments in which the cyclooctadiene in **8**–BArF, is replaced with 3-methyl-1,5-cyclooctadiene (to shift the mass of the diene complexes) confirm that all of the initial diene complex is reduced within the first 5 minutes and therefore does not contribute to the mass spectrum 15 minutes after initiation of the reaction. Interestingly, if the H_2 pressure in a reactor containing the catalyst, **8**–BArF, styrene, and H_2 is released, a sample taken immediately afterwards shows principally $[(PHOX)Ir(styrene)_2]+$, underlining the importance of the in situ sampling technique described above.

We found two gas-phase reactions that are instructive with regard to the catalytic cycle. Bearing in mind that the present apparatus (with only two stages of MS/MS) does not allow more than two consecutive reactions, i.e. we cannot do controlled turnover in the gas phase, we examined the reactions of selectively prepared intermediates. $[(PHOX)Ir(H_2)]+$, produced by "hard" desolvation conditions applied to electrosprayed ions from a solution of **8**–BArF and H_2, was then subjected to multiple collisions with ethylbenzene, producing, among other species, an ion with the composition $[(PHOX)Ir(ethylbenzene)]+$. (The rigor of desolvation is controlled by the tube lens potential in the TSQ 700 mass spectrometer. There is a qualitative range from soft to hard, corresponding to tube lens potentials of 10–150 V.) The ion, assumed to be species **IV**, was isolated in the gas phase by selection according to its *m/z* ratio. Collision-induced dissociation (CID) of **IV** with argon leads to exceedingly

facile loss of dihydrogen, producing the styrene complex **V**. If 1,3-diethylbenzene or 1,3,5-triethylbenzene are used instead of ethylbenzene, multiple dehydrogenations are observed. (1,5-Cyclooctadiene in **8**–BArF can be readily replaced by equilibrating **8**–BArF in a large excess of by 3-methyl-1,5-cyclooctadiene and then pumping off all volatile components. The control experiment was necessary because the cyclooctadiene complex has a mass very similar to that of styrene or ethylbenzene.) Because the selectively prepared gas-phase species **IV** has no opportunity to go "foward" in scheme 8.1 – the substrate-for-product ligand exchange is shut off, it traverses the catalytic cycle backwards until it undergoes the irreversible (in the gas-phase) step in which dihydrogen dissociates and leaves. One should note that the facile production of **V** does not mean that complex **V** is the most stable species in the catalytic cycle, but merely that **V** is the product of a step that is irreversible under the experimental conditions. In the second instructive MS/MS experiment, a single isotopomer of **V** is prepared and isolated by its *m/z* ratio, and then reacted under soft conditions (initial collision energy of 6.9 kcal/mol or less in the center-of-mass frame) with D_2 gas. The sole observable products are **V**, **V[D$_1$]**, and **V[D$_2$]** as can be seen in Figure 8.3.

The absence of even an adduct mass in the gas-phase reaction of **V** with H_2 would mean either that there is no reaction at all-only coordination followed by a fast dissociation-or that none of the species **I-IV** lies in such a deep well that it would be long-lived enough to be observed before the irreversible loss of H_2 regenerated **V**. The D_2 experiment indicates unambiguously that the latter case is operative. In other words, isotopic exchange in **V** confirms the intermediacy of at least species **I-III** even if they are not directly observed in the mass spectrum.

Mere observation of a species formed in situ during a catalyzed reaction does not prove its participation in the catalytic cycle. It could be reservoir species, an unreactive spectator, or even a catalyst deactivation product. Moreover, the inability to observe a particular species does not prove that it is absent in the catalytic cycle because those species in the catalytic cycle with the highest rate constants for subsequent reaction will occur with the lowest concentration at steady-state. An observed species can, however, assigned as an intermediate in the cycle with reasonable certainty if it can be shown that the species is competent in the subsequent elementary reaction steps needed for turnover. The mass spectrum of a catalytically-active solution of **8**–BArF suggests that **II**, or a species of the mass of **II**, could be the resting state species. The
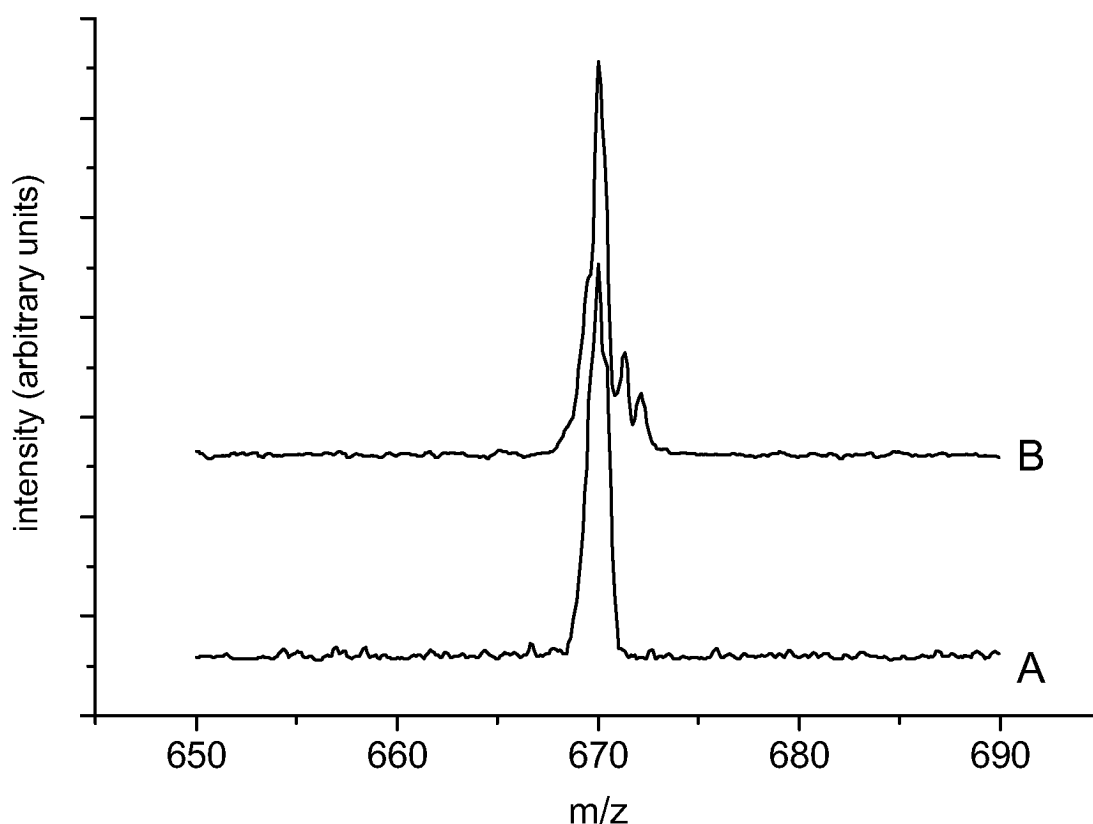
Figure 8.3: Daughter ion mass spectrum generated by mass-selection of one
isotopomer of **V** at m/z = 670 (Trace A), and reaction of the
mass-selected ion with D_2 (Trace B) at a collision energy set to
6.9 kcal/mol in the center-of-mass frame. Under comparable con-
ditions, the reaction of **V** with H_2 does not form an adduct mass,
but rather returns only **V** back. Mono- and dideuteration is clearly
visible in the experiment with D_2.

competence of the putative **II** to enter into the elementary reactions in Scheme 8.1 is
supported by the two gas-phase reactions. In the absence of either H_2 or excess olefin,
IV dehydrogenates to **V**, connecting the hydrogenation product mechanistically to the
substrate olefin complex. In the other direction, production of **V**[D_1], and **V**[D_2] from
the reaction of **V** and D_2, shows that both dihydrogen cleavage and the insertion of the
substrate olefin into the Ir-H bond are facile and reversible when turnover is blocked.
The gas-phase experiments by themselves do not identify unambiguously which of
the isobaric ions **I-IV** is the actual resting state in catalytic cycle, but they do show
that the overall cycle with the species **I-V** is mechanistically plausible. Auxiliary ev-

idence, e.g. ^{1}H NMRresults by Drago, Pregosin, and Pfaltz,[151] can be interpreted to suggest that a dihydride like **II** is more stable than a dihydrogen complex like **I**, which leads one to presume that the resting state is in fact **II**. Lastly, the experiments strongly suggest that trihydrides, e.g. Ir^V species, play no significant role in the hydrogenation reaction. Given the computations by Brandt, Hedberg, and Andersson,[148] the demonstrated catalytic activity by well-characterized iridium polyhydrides, as well as experimental evidence for a minor route through polyhydrides[152, 153] from Crabtree's catalyst by Brown and coworkers,[154] we have looked for the Ir^{III} hydrido dihydrogen/ Ir^V trihydrido complexes. ESI-MS analysis of the activated catalyst solution under H$_2$ pressure does show ions with the compositions [(PHOX)Ir(styrene)(H$_2$)]+ and [(PHOX)Ir(styrene)(H$_2$)$_2$]+. The former corresponds to species **I-IV** in scheme 8.1. The latter possesses the mass and the composition of the Ir^{III} hydrido dihydrogen complex or the Ir^V trihydrido species predicted in the calculation where we have no definitive experimental evidence and where we believe that this ion is actually [Ir(PHOX)(ethylbenzene)(H$_2$)]$^+$. Although a species of that composition appears to be present in solution under active catalytic conditions, the gas-phase experiment suggests that it plays no major role in the catalytic cycle. Given that the ion isolated as **V** was reacted with D$_2$ under conditions where it underwent ca. 10^4 collisions with D$_2$ in the timeframe of a few to 100ms, we estimate a gas-phase collision frequency on the order of 10^6 sec^{-1}. Interestingly, if one were to characterize the diffusion-controlled encounter rate of a catalyst molecule in solution with dissolved H$_2$ using k$_{2ndorder}$ $\approx$ 10^9-10^{10} l·mol^{-1}·sec^{-1} and [H$_2$] in the millimolar range,[155] then one concludes that the gas-phase and solution-phase encounter rates are similar and that a species of the composition [(PHOX)Ir(styrene)(D$_2$)$_2$]+ had the opportunity to form in the gasphase (and subsequently dissociate again) if it were an important species in solution. Burgess *et al.*[154, 156, 157] report an alternate mechanism for the incorporation of more than two deuteriums via reversible formation of p-allyl intermediates. This mechanism cannot operate in the present case with styrene as the substrate because there are no allylic positions for the exchange. If there were a favorable mechanism for hydrogenation for species of this composition, then one would expect to see trideuterated [(PHOX)Ir(styrene)]+ products in the **V** + D$_2$ reaction because, given the reversibility of elementary steps in the gas-phase reaction, even a transient Ir^V intermediate with three chemically equivalent deuterides (and an alkyl with one deuterium) would

produce at least partial incorporation of more than two deuteriums into the styrene substrate.

A solution-phase control experiment in which 0.1 ml styrene and 0.1 mg **8**–BArF (S/C 15'000) are degassed (5 min freeze-pump-thaw) in 5ml CH2Cl2 and then treated at 28°C with 6 bar D_2 was checked at 2, 5, 10, 20, 40, and 85 minutes by GC-MS, showing up to 50% conversion to ethylbenzene (at 85 minutes) with no deuterium incorporation in the unreacted styrene at any time (s. figure 8.4). The ethylbenzene product was cleanly dideuterated.
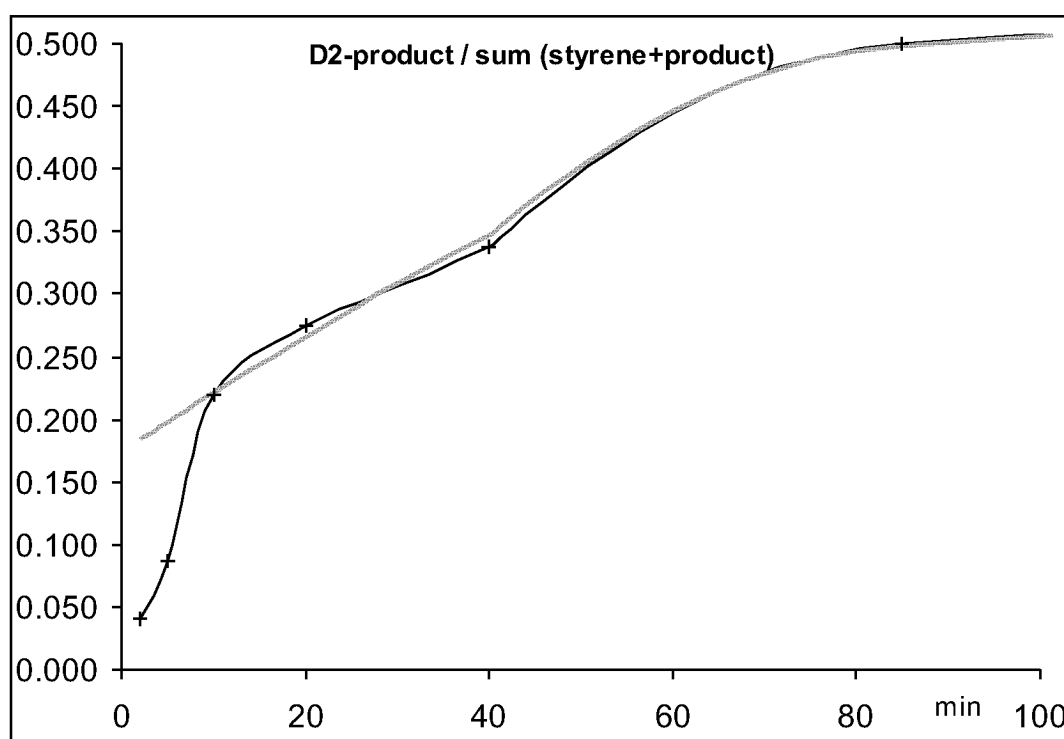
Figure 8.4: Regression with first order kinetics in product, k = $5.86 \cdot 10^{-3}$

This is consistent with the gas-phase results if one considers that 1. the high D_2 pressure selectively lowers those intermediates and transition states in which the elements of D_2 are included, and 2. turnover is not blocked because ligand exchange of styrene for ethylbenzene is now possible. While the solution-phase experiment alone is not completely definitive, it is consistent with the conclusion from the gas-phase studies that Ir^V polyhydrides play no significant role in the catalytic cycle.

Examination of Figure 8.3 shows that the trideuterated styrene complexes are absent. We believe that the observed mechanism differs from the computationally predicted one because the computation employed a markedly truncated substrate and complex with much less steric constraints and different electronic properties in the search for the minimum-energy reaction path.

8.3   Conclusion

In conclusion we report gas-phase reactions of selected organometallic ions that reveal a plausible mechanism for the catalytic hydrogenation of olefins by the $[Ir(PHOX)(COD)]^+$ X^- family of catalysts. In contrast to the results of a computational study, the most likely mechanism is found to involve the more expected cycle with Ir^I and Ir^{III} species. There is no evidence for the participation of Ir^V complexes. In contrast to in situ spectroscopic studies which rely primarily on identification of species in solution whose role in the reaction must be subsequently ascertained by independent means, the preference for the Ir^I/ Ir^{III} cycle over the alternative Ir^{III}/ Ir^V mechanism is supported by gas-phase reactivity data which are diagnostic even if the purported intermediates are present in such low steady-state concentration so as not to be directly observable.

The content of this chapter was published 2004 in Angew. Chem. Int. Ed.[30]

Chapter 9

Improving the CID Threshold Measurement Techniques on a FINNIGAN TSQ 700

Summary

This chapter introduces a new method for CID threshold measurements using the DAC scan feature to improve the performance, data quality and time consumption of the measurements. Additionally important parameter settings and optimizations for good energy distributions and suitable measurement results are described. It is currently applied to the investigation of $Cu^{I}(BOX)_2$ and $Cu^{I}(AzaBOX)_2$ binding energies and several other projects. This chapter should give a short overview about the method and point out the most important technical issues for accurate future experiments. Most of the measurements were performed in cowork with Eva Zocher.

9.1   Introduction

To obtain thermodynamic and kinetic information about a gas phase reactions such as noncovalent binding energies carried out for example directly in a mass spectrometer either the Cooks kinetic method[158], which is based on the competitive dissociations of mass-selected cluster ions using known reference compounds or CID (collision induced dissociation) threshold measurements for the direct investigation of binding constants can be used.[159]

The thermodynamic information is obtained from gas phase collision experiments of an ion beam of the mass selected charged molecules of interest with an chemically inert collision gas as Ar, Kr or Xe. The energy threshold for the dissociation processes of interest is determined by scanning the kinetic energy of the ion beam and therefore the available collision energy. The resulting ion signal at the mass of the charged fragments is measured energy dependent at different defined pressures. For heavier inert gases more energy is available in the center–of–mass frame.

The resulting energy-dependent reactive cross-sections $\sigma(E)$ can then be subsequently modeled using a RRKM (Rice–Ramsperger–Kassel–Marcus)[160] model as in Armentrout's CRUNCH[161] program to obtain absolute energies. For this method the frequencies of the given parent molecule and all fragments are needed usually calculated at DFT level which is time consuming especially for large molecules. A new program based on an effective frequency approximation as QRRK (quantum version of the RiceRamspergerKassel)[162] without the need of all the frequencies is in development in our group.

On our TSQ 700 machines the measurement is performed as follows:
The ions of interest are either formed in solution and directly electrosprayed or formed through the additional recombination of the electrosprayed ions with a volatile neutral reactant in the first octapole or 24–pole. At the exit of this region the ions are quasi thermalized and in equilibrium at the given DC offset even if there was no additional gas pressure present. At this stage a mass selection using RFD or daughter mode can be performed by the first quadrupole. The next step is the collision with the inert gas in the second (CID–) octapole with the inert gas. The kinetic energy of the ions is defined by the relative offset of the octapole versus the offset of the mentioned equilibrium. The formed charged products can be analyzed by the second quadrupole and detected

by the electron multiplier.

9.2 CID Threshold – Energy Distribution Issues

The measured energy dependent CID threshold curve is the theoretical threshold curve convoluted with the energy distribution of the ions at the entry of the CID collision cell. To obtain accurate results by fitting the theoretical threshold curve a well defined and narrowest possible energy distribution is required. Therefore all applied potentials in the MS should be optimized for a minimal energy distribution.

The first multipole ion guide is one of the most important sources of the energy broadening and the form thereof. The widely used quadrupoles produce significant high energy tailing by heating up the ions during the oscillation through the guiding field especially approaching the field borders. Multipoles of higher order reduce this effect by steeper "walls" of the enclosing field. Therefore the original octapole of one machine was exchanged to a 24–pole by Christian Hinderling which described in his Ph.D. thesis[41] based on an idea of D. Gerlich.[163] This resulted in a narrow and nicely gaussian shaped energy distribution. In earlier attempts a advanced thermalization with additional Ar or He gas in this multipole region was performed which turned out to have no detectable effect on the energy distribution of most analytes.

A second important source for additional heat–up is the mass selection in the first quadrupole. For simple systems with only one product channel the RFD mode is available which gives a much narrower energy distribution than the daughter mode. For complicated systems the daughter mode can be used in the lowest possible selection resolution which still baseline–separates the species in the parent spectrum to obtain narrower energy distributions. A sharper selection results in more heat–up of the ions and therefore to a broader energy distribution up to the double width.

The TSQ 700 has a large number of built in focusing lenses in the ion processing path which have also an influence on the energy distribution of several percent each. The best setting turned out to be the flattest possible potential settings of the devices before the CID cell with almost no ion focussing or other acceleration than the CID offset keeping more than 50% of the total ion transmission of the original transmission optimized standard settings. These settings are put together in table 9.1.

Special settings for positive mode:

TSQ parameter	settings
ll2(p11), *poff*(p2), *l2l*(p14), *l23*(p15)	are set to constantly -5V.
lll(p10)	is set to constantly -10V.
tubel(tubelens, p25)	is set to the lowest possible value to obtain good intensities for the parent ion.
pres(parent resolution, p4)	is set to the highest possible value to still baseline separate all species in the parent spectrum.
dres(daughter resolution, p5)	is set to the same value than *pres*.
For all other parameters the transmission optimized standard settings were preloaded.	

Table 9.1: Optimized settings for CID-threshold measurements on a TSQ.

While the energy distribution is dependent on many fine–tuneable parameters and additionally on the molecule properties itself an energy distribution curve has to be measured for every CID threshold data set.

9.3   The "Old" CID Measurement Method

To obtain a energy dependent CID threshold curve with a TSQ 700 a basic method was established several years ago in this group. In daughter mode for every data point on the energy scale a CID collision offset (*coff*, p9) was set and a full spectra scan was performed with the second quadrupole, even with averaging of several scans. For the RFD mode two spectra per data point had to be taken for every parent mass, one cutting above one below the selected *m/z*. A subtraction gives the desired intensity value. ICL scripts (integrated command line of the ICIS software) helped to automate the measurement procedure. The product peaks in the numerous spectra then were integrated using the in house built c-program TSQReader (*tsqr*)[164] written by Derek Feichtinger. The integrals were then assembled to the energy dependent curves and worked up with CRUNCH[161] (s. figure 9.1).
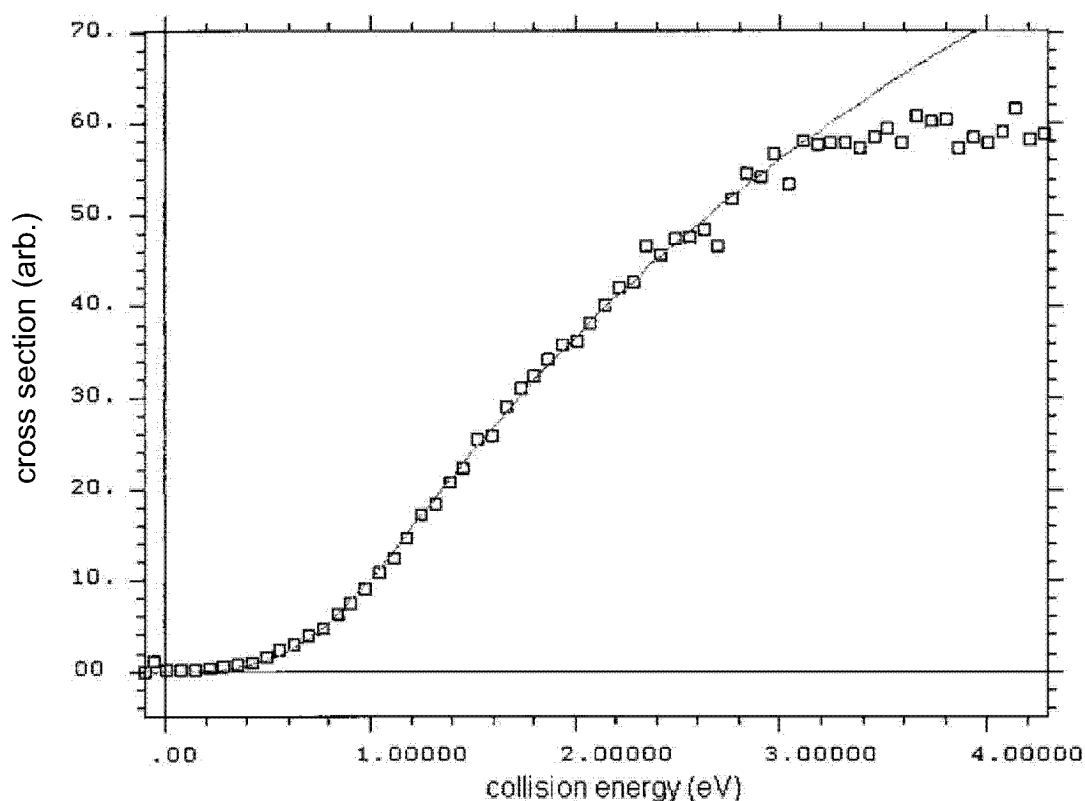
Figure 9.1: CID threshold measurement and CRUNCH[161] fit of [(Me₃P)Ir^{III}(NCCH₃)(CH₃)]$^+$ measured by Ch. Hinderling using the old integration method.[6,41]

The described method was used for all CID measurements and publications in our group before the year 2000.[6,41,42] The time consumption for the measurement with a reasonable number of points is quite high. It requires really stable signal intensities and pressures during the whole measurement series which is quite hard to obtain.

The idea to use the DAC optimization scan feature of the TSQ spectrometer on the collision offset parameter to have shorter and more reliable measurements appeared already then but first tests gave curves with shapes differing from expectation based on reference measurements. Therefore the idea was discarded as reliable. For 2-3 years no CID threshold measurements were performed then.

9.4 The "New" DAC Scan Method

The successful mobility experiments in the CID chamber of a TSQ 700 described in chapter 3 with extended usage of DAC scans resurrected the idea of threshold measurements using a DAC scan again. The faster acquisition, the lower dependence of the curve form of changes in the spray intensity on a long time scale and the larger number of acquired data points could lead to much more accurate data sets.

If the scan speed is selected taking care of the ion decay in the MS the manual setting of the *coff* parameter (p9) or scanning it with a DAC scan is principally not expected to remarkably differ if the machine is applying it in the same way. As measured in the chapter 4.4 the complete machine decay half life was about 300 ms for the modified TSQ 700. In the region after the first quadrupole, where the measurement takes place only 30-60 μs were expected. Measurements at different scanning speeds showed no more change of the shape or shifting of the resulting curve above 1-3 s per scan.

For the re–introduction of CID threshold measurements in our group in 2004 test measurements on $[Cs(18\text{-}crown\text{-}6)]^+$ were performed together with Loubna Hammad applying directly the DAC method. Subsequent workup with CRUNCH agreed well with the published results of Armentrout *et al.*[165]

While the scanning speed could not be the only source of the different curve forms obtained by former group members another difference had to be present. By applying manually the collision offset all voltages after this region are also changed automatically by the MS in the same amount to keep constant conditions at the exit of the CID octapole. The behavior of the DAC scan in this point was not known. Therefore DAC measurements with a $[Cu^I(BOX)_2]$ complex were made at different manual presets of the *coff* parameter which resulted in the curves in figure 9.2 showing changing cutoff ramps for a partage of the ions. This clearly showed that the automatic shift does not take place in the DAC scan mode.

For the fitting with CRUNCH usually the normed curves as shown in the lower part of figure 9.2 are taken. The most important part for the modeling is the rising part near threshold. If the manual offset differs more than 10-20 V of the minimal scanned voltage (resp. the maximal applied collision energy) this part changes drastically. It contains only the ions of the high energy tail of the total distribution curve. This

leads obviously to a wrong E_0 as fitting result by CRUNCH. A careful evaluation and selection of this parameter has to be done prior to any measurement. The preloaded standard setting of the machine at -28.5 V is only suitable for weakly bound molecules.
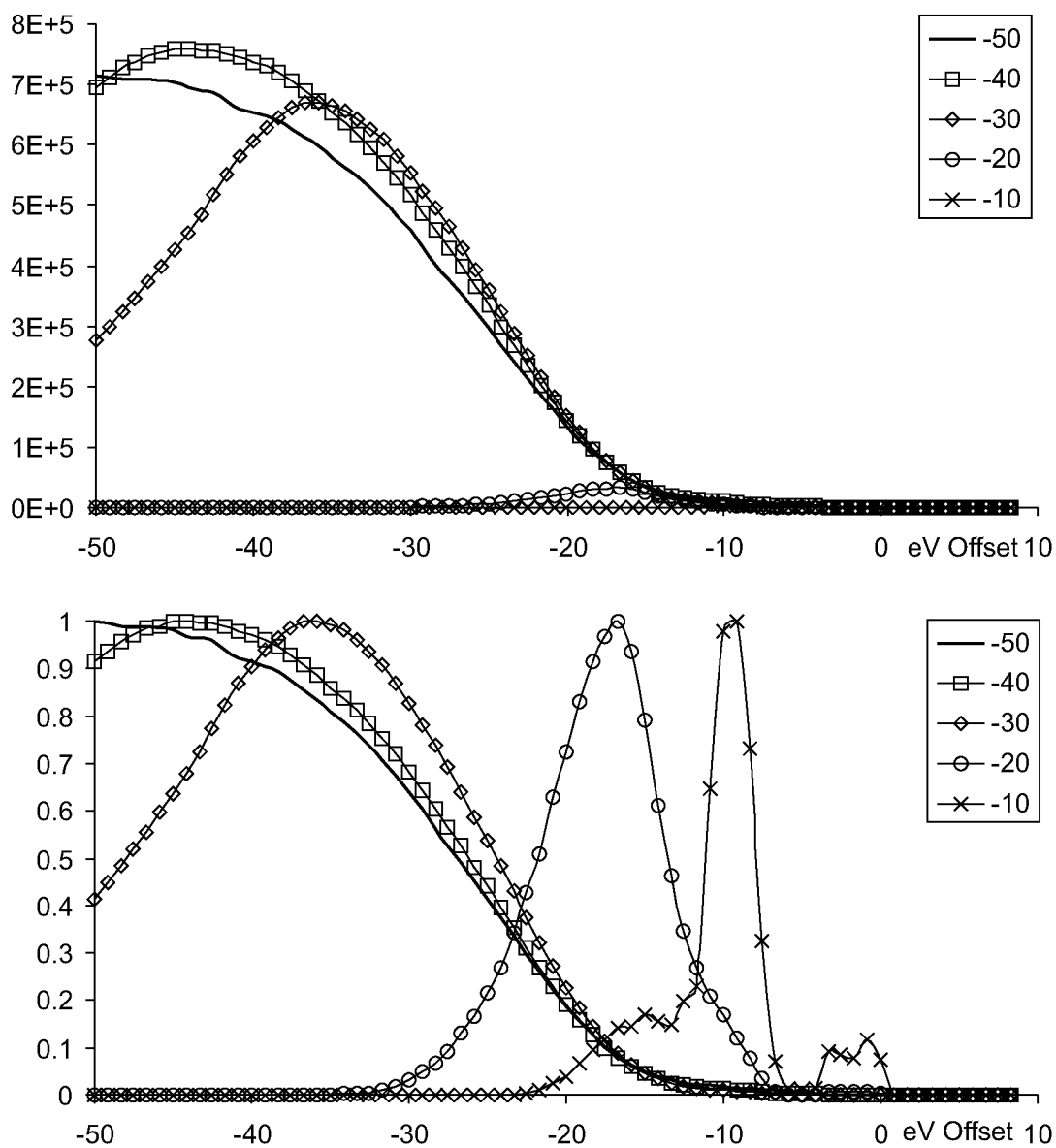

Figure 9.2: CID threshold measurements at different preset collision offsets using the new DAC method on a [Cu^I(BOX)$_2$] complex.
upper: absolute intensity
lower: normed as usually used in crunch

Although the main problems of the DAC method were figured out a comparison of the results of this method and the "trusted" old method had still to be performed to ensure the accuracy of the method. Measurements with $[Cu^I(BOX)_2]$ showed good agreement of the resulting points of the integration method and the DAC method taking care about the discussed settings (s. figure 9.3).
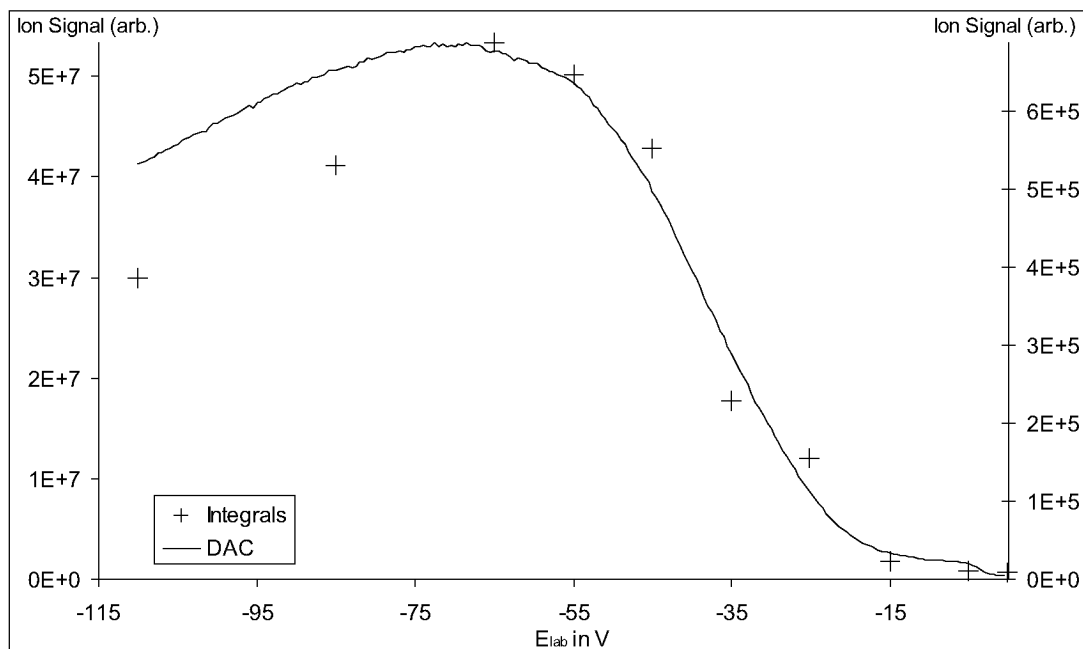
Figure 9.3: Comparison of CID threshold measurements with the old (+, Integrals) and new (-, DAC) method on a $[Cu^I(BOX)_2]$ complex.

Another important factor for the data workup with CRUNCH is the average pass-through time of the ions through the CID octapole which is equal to the available reaction time. This time is dependent on the applied gas pressure and the collision cross section (e.g. ion mobility) of the ion of interest at fixed drift cell length of 18.5 cm. Therefore to raise the accuracy of the modelling a measurement of the average residence time for at least every new analyte group is recommended.

This could be done using the ion mobility method described in chapter 3 for the total ion current. With the inflection point of the resulting curve the exit velocity can be calculated. While the entry velocity for a given collision offset is known the average velocity and therefore the average residence time can be calculated.

Another possibility is with a (too) fast neutral loss scan of only several mass units where an additional artificial mass shift of the parent ion can be observed which is due to the residence time. Both methods gave a residence time of about 30-40 μs for small ions of the size of aniline or also $[Cs(18\text{-crown-}6)]^+$ in the CID region.

9.5   Conclusion and Improved Experimental Procedure

The successful introduction of the faster DAC method for CID threshold methods was shown. It promises a lower dependence of the curve form of changes in the spray intensity on a long time scale and the larger number of acquired data points which could lead to much more accurate data sets. The major sources of the former negative results were found.

All new CID publications of our group within the last year[166–168] were performed using this new method.

Best results can be achieved using the settings presented in table 9.1 and the discussed offset presets discussed herein. For accurate measurements it turned out to be also important to manually control the *zero* cutoff parameter of the TSQ to ensure that the curve really starts rising from the true baseline. Otherwise a slight shift of the threshold could result.

In collaboration with Eva Zocher a project on the binding energies of the second ligand of $[Cu^I(BOX)_2]$ and $[Cu^I(Aza\text{-}BOX)_2]$ complexes with phenyl and isopropyl substituents is currently in progress were unexpectedly high accuracy and reproducibility of the CID threshold measurements in the range of several kcal/mol was reached applying all the discussed features in this chapter. It is expected to be a main part of her PHD thesis.

Part III

Experimental Section

Chapter 10

Experimental Section

10.1 General Remarks

GC/MS: FISONS INSTRUMENTS GC 8000 coupled to a FISONS INSTRUMENTS MD 800 MS, column: DB-5 MS capillary GC-column from J&W Scientific (12 m length, 0.25 mm internal diam., 0.25 μm layer, stat. phase: 95% dimethyl-5-diphenylpolysiloxane), carrier gas: He (flow rate: 1.0 ml/min, rel. pressure 30 kPa (300 mbar)), temperature programs: [50°C, 2 min, 10°C/min, 250°C, 20 min] or [35°C, 5 min, 10°C/min, 250°C, 20 min], injector temp. 200°C, solvent delay: 3 min for liquid (l) 0 min for gas phase samples (g), EI 70 eV detector temp. 250°C.

NMR: BRUKER *AMX–300* (^{1}H: 300 MHz, ^{13}C: 75 MHz, ^{31}P: 121 MHz), VARIAN MERCURY *XL 300* (^{1}H: 300 MHz, ^{13}C: 75 MHz, ^{31}P: 121 MHz) spectrometer, chemical shifts (δ values) are reported in ppm with respect to Me$_4$Si ($\delta = 0$ ppm) used as an internal standard for ^{13}C and ^{1}H NMR and a to 85% aqueous H$_3$PO$_4$ solution used as an external standard for ^{31}P NMR, respectively; coupling constants (J) are given in Hz. ^{13}C NMR and ^{31}P NMR spectra were proton broad-band-decoupled. The multiplicities of peaks are denoted by the following abbreviations: s: singlet, d: doublet, t: triplet, m: multiplet, dd: doublet of doublet, ddd: doublet of dd, dt: doublet of triplet, se: septet, br: broad.

TLC: MERCK silica gel 60 F_{254} plates; visualization by UV_{254} light.

10.2   Synthesis of Compounds

All reactions were carried out under argon or dry nitrogen using a schlenk–line or for the small ($<$ 2 ml solvent and mg range of compounds) reactions as well as the preparation of spraying solutions of air sensitive compounds inside a M-BRAUN labmaster100 or labmaster130 dry box. The solvents for organometallic compounds were dried by distillation from the following drying agents prior to use and were transferred under N_2: diethyl ether (Na/K), n–hexane (Na/K), toluene (Na), MeCN (CaH_2), THF (K), CH_2Cl_2 (CaH_2), ethanol (Mg), methanol (Mg), isopropanol (CaH_2). All other solvents were used as purchased. For the investigations on the amino acid clusters and for the spray solutions of the DCC branching ration project the spraying solutions with quenched compounds were prepared with commercially available dry P.A. quality solvents. Flash chromatography: FLUKA silica gel 60, type 60752 (230–400 mesh).

The $[Ir(PHOX)(COD)]^+$ X^-–BArF (**8**–BArF) precatalyst for the Ir–PHOX project was a gift from Prof. Dr. Andreas Pfaltz[143]. The sensitive active species $[Ir(PHOX)L_2]^+$ was prepared in situ by direct hydrogenation and loss of the COD in CH_2Cl_2. It is only stable under relative hydrogen pressures above 4 bar protected by at least one H_2– or two H– ligands.

Also the needed compounds for the synthesis of the [Pd(PHOX)]catalyst as well as one substrate (marked in figure 5.2 on page 84) was a gift from Pfaltz's group. The exact preparation was performed right before the use in a one pot reaction as described in literature[124] and diluted to 10^-5 M in CH_2Cl_2. The alcoholic form of other substrates was prepared by a Br–Grignard addition within 1.5 h at 0°C to *trans*-cinnamic aldehyde and cleaned by column chromatography. The products were then checked by GC and NMR. A subsequent reaction with acethyl chloride with a catalytic amount of 4-(dimethylamino)pyridine for 8 h at 0°C gave the needed acetyl leaving group. After this step the substances were cleaned again by column chromatography and checked by GC and NMR.

10.2.1 Synthesis of DCC-C$_5$, DCC-C$_6$ and DCC-C$_7$ Model compounds

The branched and unbranched DCC model compounds with chain lengths of 5 to 8 were prepared using the following grignard procedure:

In a 10 ml Schlenk tube with evaporation cooled upper half a solution of 1 mmol of the bromo alkane in 1 ml Et$_2$O was slowly added within 10–15 min to a suspension 24 mg (1 mmol) Mg cuttings and 1 ml of Et$_2$O. After relaxation it was stirred further for 30 min at RT. For some of the grignards starting help by a heat gun or small iodine cristals was necessary after addition of 10–20% of the bromo alkane addition. Then a solution of 206 mg (1 mmol) DCC in 0.5 ml Et2O was added within 10 min at 0°C to the gold–brown solution producing a white fall out of MgBr$_2$ and stirred for another 30 min. After quenching with H$_2$O and extraction with CH$_2$Cl$_2$ it was dried by MgSO$_4$ filtrated and the solvent removed obtaining a colorless or slightly yellow oil or solid in some cases.

MS: (ESI, CH$_2$Cl$_2$and CH$_2$Cl$_2$/MeOH 1:10) [M+H] and a small amount of [M+Na]. Several products were also checked by ^{1}H NMR showing a pureness of at least 80% without further purification.

10.3 Electrospray Ionization Mass Spectrometry

The mass spectra were acquired on FINNIGAN MAT TSQ 700 and LCQ Classic mass spectrometers equipped with an electrospray ionization (ESI) source. The following section gives an overview as given in[42] over the instrument source and operational performance features. Detailed information is given in the instrument manuals. The physical background for the operation of the quadrupole as mass selection device and the (still not completely understood) transformation of charged solutes into the gas phase by electrospray ionization have been reviewed in former Ph.D. theses[25, 27, 37, 41, 42] and several textbooks (e. g. [77, 169, 170]).
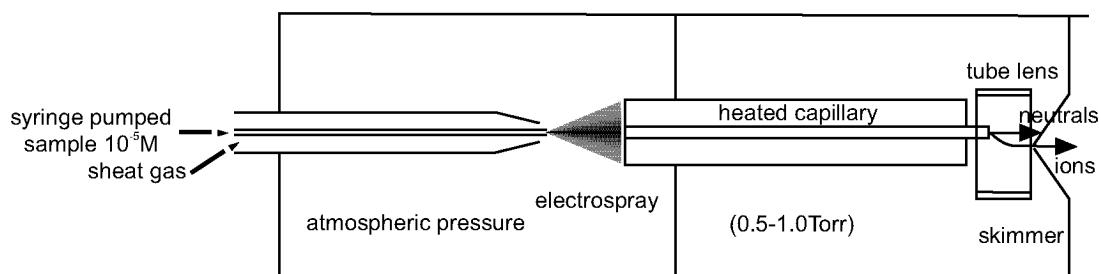
Figure 10.1: The API ion source.

10.3.1 The Original Instrument Source and Heated Capillary

Without the precoupled mobility cell the original source of the machines works as follows:

The sample solution is delivered by a syringe pump through two successive fused silica capillaries to the source region as indicated in Figure 10.1. A spray voltage of 3.5-5.0 kV is applied on the tip and therefore the spray forms at the interface between the incoming capillary and the solid heated capillary. In the case of the LCQ classic the spray tip is formed out of a fine stainless steel capillary which allows lower flow rates and slightly lower voltages (3.0-4.5 kV). Nitrogen is used as a sheath gas at a pressure of 20 to 40 psi to assist the formation of the spray and the first desolvation of the formed charged droplets containing analyte – atmospheric pressure ionization (API).

Further desolvation takes place in the heated capillary with the help of heating (150-250°C) and differential puming (1bar to around 1mbar). In the following skimmer region the charged and uncharged particles are separated by a slight offset of the heated capillary to the skimmer orifice. With the help of the tube lens the charged species are electrostatically directed through the skimmer (0 V). Volatile uncharged species are pumped off by the API–forepump non volatile ones collected by the skimmer plate. By changing the tube lens potential the rigor of the conditions can be driven through activation of the charged species by collisions, which can lead to fragmentation of the sample prior entering the high vacuum region of the manifold.

10.3.2   The Analyzer Assembly of The TSQ 700

Behind the skimmer the multipole rods are located which serve as ion guides and mass analyzers. The FINNIGAN TSQ mass spectrometers possess a tandem octapole–quadrupole assembly (Figure 3.2 on page 22).

A first octapole (or 24–pole in the case of the modified TSQ 700) is present directly after the skimmer. This region is called CI region by the machine manufacturer. In some experiments where ions had to undergo two subsequent ion–molecule reactions, this region was used to perform the first reaction by introducing a gaseous reagent to it (e.g iridium-project, section 8 on page 125). The octapole is followed by a quadrupole which can be operated as a mass analyzer (parent mode), as a mass filter (daughter mode), or as an ion guide (RF only mode).

A longer, slightly curved octapole is mounted next to the quadrupole. The non–linearity allows ions to pass through with virtually no loss, while fast neutrals which do not follow the curve leave the rod assembly and are pumped away. The octapole is always used as a transmission device with transmission efficiencies close to 100 % if no collision gas is present. A collision cell is surrounding the octapole which can be pressurized up to 10 mTorr. This is the CID region, the site where collision induced dissociation (CID) takes place. A second quadrupole is located behind the octapole and acts as a mass analyzer in daughter mode and as a transmission device in RF only mode.

10.3.3   The Analyzer Assembly of the LCQ Classic

The LCQ ion trap has principally the same source and skimmer design as the TSQ spectrometers. After the skimmer also a octapole is guiding the ions to the mass analyzer. In this region coordination with reaction gases at low pressure can also be performed after a slight modification on the gas inlet pipe system.

Then the ions enter the quadrupole ion trap which is a cylindrical symmetric closed quadrupole having two parabolic end caps and a ring electrode with parabolic section applying the field instead of the linear quadrupoles. It can principally store the ions, selectively keep only a small mass range of them or selectively eject them in a given mass range to be detected. Sweeping the latter will result in a mass spectrum. In the same region activation by a RF and therefore collisions with the background gas

He can fragment the previously stored ions. There can be multiple selection–storage–
activation cycles which allows MS^n instead of only one fragmentation step like in the
TSQ machines (MS/MS).

Nevertheless the activation energy can not be defined and described as well as
in the TSQ machines which makes them the method of choice if a reliable energy
dependence for the fragmentation has to be measured (CID threshold or Cooks kinetic
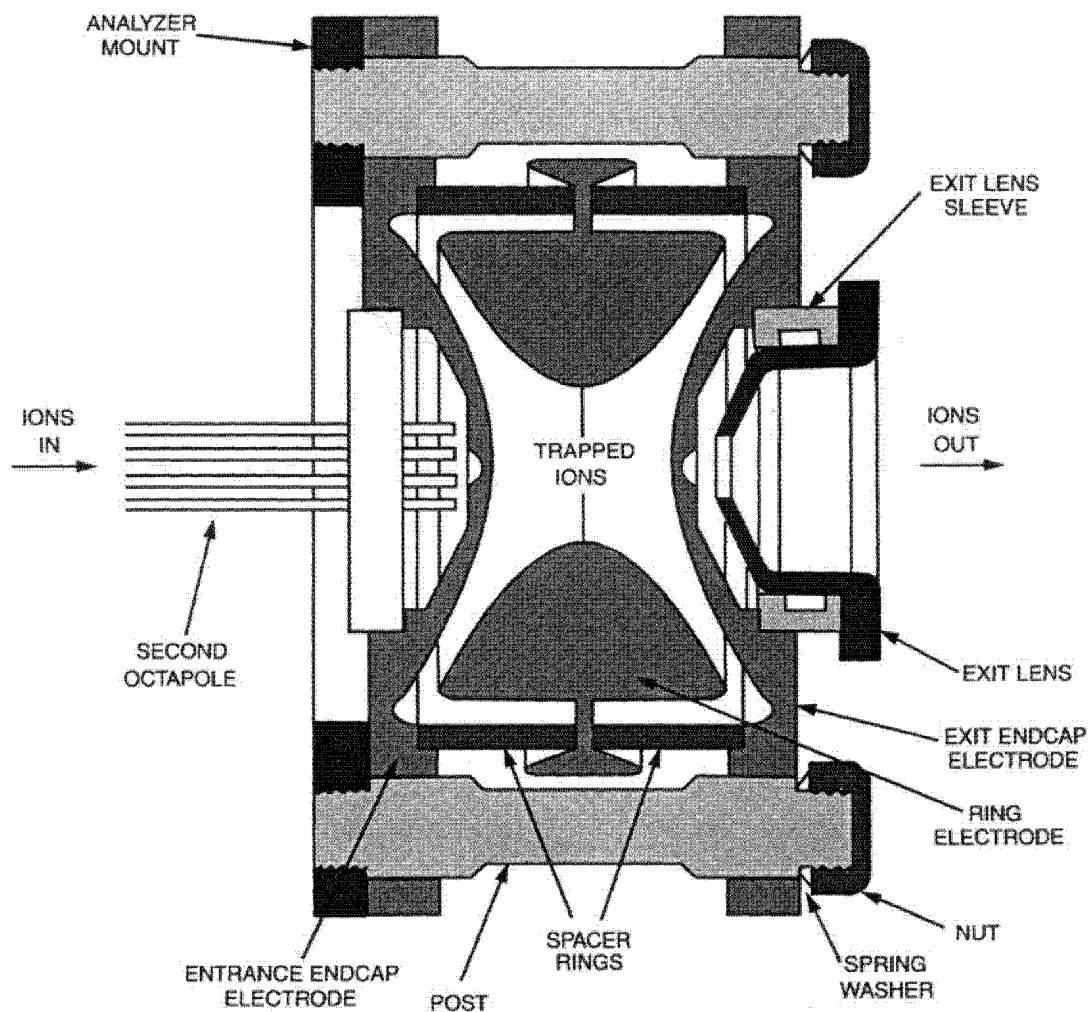method measurements).

Figure 10.2: Section of a quadrupole ion trap of a FINNIGAN LCQ.

10.3.4 Ion Detection

The detection system basically consists of a conversion dynode and a continuous dynode electron multiplier (s. figure 10.3) in all the FINNIGAN MS types. The conversion dynode is located perpendicular to the ion-current axis and is operated at 15 kV.

The secondary particles produced upon impact of the analyte ions are focused and accelerated by the voltage gradient of the continuous dynode electron multiplier. Collision of these particles with the cathode starts a cascade of electrons, leading to a measurable current when the electrons hit the anode which, together with the end of the cathode, is at ground potential.
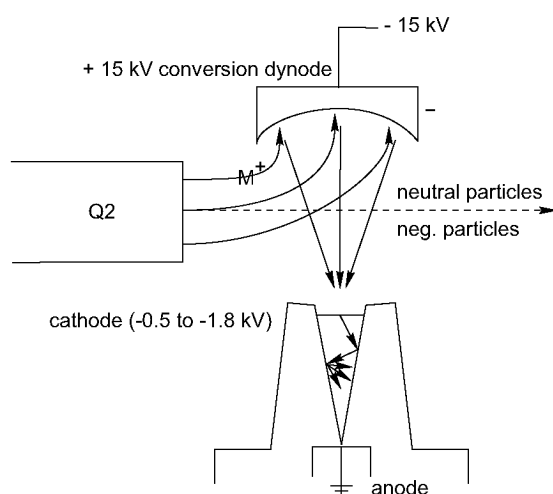
Figure 10.3: The ion detection system.

10.3.5 Vacuum and Gas Inlet System

The vacuum system in the manifold is maintained by two Varian V250 turbopumps, backed by two mechanical forepumps. A separate mechanical pump serves as the forepump to API region.

Two original separate inlet lines exist, leading to the CI octapole (or 24–pole) and CID octapole. Additional needle valves allow the gases to flow into the respective regions of the vacuum manifold.

All pressures in the various regions of the instrument are measured by gauges in place and can be read directly into the workstation.

10.3.6   Modes of Operation

In the simplest case, the first quadrupole is used as a mass analyzer and the following octapole and quadrupole are used as pure transmission devices.

The applied collision energy can be controlled as an offset value to the CID octapole and all devices after.

10.3.6.1   Daughter Scan Mode

In this mode, ions of a given mass to charge ration (parent ions) are selected in the first quadrupole. The selected ions can be collided with an inert gas, typically argon, whereupon collision–induced dissociation (CID) occurs. The resulting fragments and the native parent ions are analyzed in the second quadrupole. In the same operation mode a reaction of mass selected ions with a neutral reagent gas can be performed using lower collision energies.

10.3.6.2   Parent Scan Mode

Ions from the source are transmitted sequentially in the first quadrupole. They pass through the collision cell and can fragment by CID. The second quadrupole is set to transmit only ions of a given mass to charge ratio. Thus, only those parent ions producing the desired daughter ion lead to a detectable signal. In this mode, the data for the mass to charge ratio is provided by the first quadrupole whereas the second quadrupole acts as mass selective detector.

10.3.6.3   Neutral Loss Scan Mode

In the neutral loss scan mode, both quadrupoles are scanned over mass ranges of the same width at the same rate but an applied offset of a given mass. The resulting spectrum shows all parent ions which lose a neutral species of a selected mass by CID in the collision cell.

10.3.6.4   RF-Daughter Mode

In the radio frequency only daughter mode (RFD) the first quadrupole acts as a transmission device. However, only ions with mass to charge ratios above a selected value

are allowed to pass. In this way, the quadrupole acts as high pass filter. The RFD mode leads to higher signal intensities. In the regular daughter mode, where the quadrupole is used as a mass analyzer, only about 6% to 20% of the ions pass through, depending on the mass to charge ratio [42]. In RF only mode, the quadrupole transmits between 50% and 100% of the ions over the entire mass range. In addition, a quadrupole transmitting ions in RF only mode leaves them with a narrower kinetic energy distribution than in mass selection mode. In analogy to the other modes the transmitted ions can be collided with a gas present in the collision cell while the products are analyzed in the second quadrupole.

10.3.6.5 DAC Scan Mode

In addition to the scan modes described above, the ion intensity can be recorded depending on varying values of a selected parameter while the others remain constant. For instance, a specific mass signal can be scanned as a function of the collision cell offset voltage. This can be applied to all the parameters which are adjustable in the tuning process and has been used intensively in Chapter 3 on page 17.

10.3.7 Modifications to the TSQ 700 Mass Spectrometers

On the older TSQ 700 (a upgraded TSQ 70), the first octapole was replaced by a 24–pole and the rod length was increased to 38 cm. This required the introduction of an additional chamber to fit the new dimensions of the multipole. A large turbo pump (Leybold Turbovac 361 C) was mounted on top of the 24–pole backed by a mechanical forepump in order to work at higher collision gas pressures up to the mTorr range. An external power supply and radio–frequency generator supplied the 24–pole with the required AC/DC voltages. This modification and the description and parameters of the needed external supplies are part of C. Hinderling's PHD thesis [41] and are described therein. Two additional direct gas inlets with shorter tubing enter both CI and CID region allowing less volatile neutral reagent molecules to be entered in the two regions.

On the newer TSQ 700, a PEEK housing was built around the first octapole to allow a located of reaction gas higher pressure in that region. (Modified in cowork with G. Gerdes)

10.4 High Pressure Reactor for Hydrogenation and Direct Investigation by ESI-MS

10.4.1 Description

For the MS experiments on labile species as the Ir–PHOX complexes a special pressure reactor with a threaded pyrex tube containing a large perpendicular stirring bar was used. The tube was rated up to 10 bar. The holder was equipped with three entry tubes with shut–off valves and a manometer. A rotary vane pump high vacuum pump and argon was connected trough a glass line to one of the shut off valves. Additionally a fused silica HPLC capillary entered directly into the pressure tube through a MICROTIGHT fitting adapter, adjustable in height position. The capillary can directly be coupled to the transfer capillary of the ESI source of the mass spectrometer (s. figure 8.2 on page 128). This setup was first introduced by Rudolf Hartmann and is also described in his dissertation.[27]

10.4.2 Pressures and Procedures for The Iridium–PHOX Project

For the Iridium–PHOX project the solutions were prepared directly in the high pressure reactor under argon including. The solid precatalyst and substrates were stored, weighted and added in the dry box. The liquid substrates were freshly distilled using Na as drying agent. All solutions were freeze–pumped at least 5 times and then pressurized by 6bar of H_2 or D_2. The reactions were carried out at RT.

The exit openings of the ESI sources were closed by a silicon oil bubbler to avoid contact of the spraying solution with air.

For the GC experiments aliquots were taken by the glass capillary without dropping the pressure of the main reaction mixture.

The substrates for the gas phase reactions were also freeze–pumped at least 5 times before application.

10.5 Ion Mobility Measurements

10.5.1 General Procedures and Settings

In the ion mobility measurements parameters ar shown with shortened labels. The following table shows a legend for the shortening of the parameters in the setting tables.

TSQ:

tf	loaded tunefile (name if special)
tl	tubelens, par 25
cap	capillary, par 26 (DAC)

Tube:

sfl	solvent flow
dist	spray needle tip outpointing dist. (of cooling shield)
tv	drift tube voltage
sp	spray voltage
gfl	drift gas flow
tt	drift gas and tube temperature

If not mentioned differently the ion mobility measurements were carried out with standard settings as follows:

For the FT mobility measurements the frequency sweep range on the synchronous gate functions was always chosen empirically based on the highest frequency with observable modulation adding about 10%. The frequency steps were chosen by pre–measuring at different steps to have the highest peak in the middle or maximally at 75% of the spectra scale while also checking for prevention from Nyquist frequency artefacts.

The ion signal was detected on a single mass using a DAC scan of the heated capillary between 5 and 6 where no observable change the ion intensity appeared (".dac 26 5 6 .1 *mass*"). The standard drift gas was N_2 with additional parameters as shown in the following table.

standard settings for N_2:

tf	*stdtune*
tl	10-100 (optimized on signal intensity)
cap	DAC 5–6
sfl	5–10 μl/min
dist	+3 mm
tv	6.0 kV
sp	9.5-11.0 kV
gfl	800-1000 ml/min
tt	180°C

Measurement of Temperatures of the Drift Tube

The two provided temperatures of the Pt100 sensors in the drift tube were calibrated against a mercury thermometer to check their nonlinearity and error. In figure 10.4 the measured values for a calibration test of the two sensors housed by an glass NMR tube in a water bath are shown.
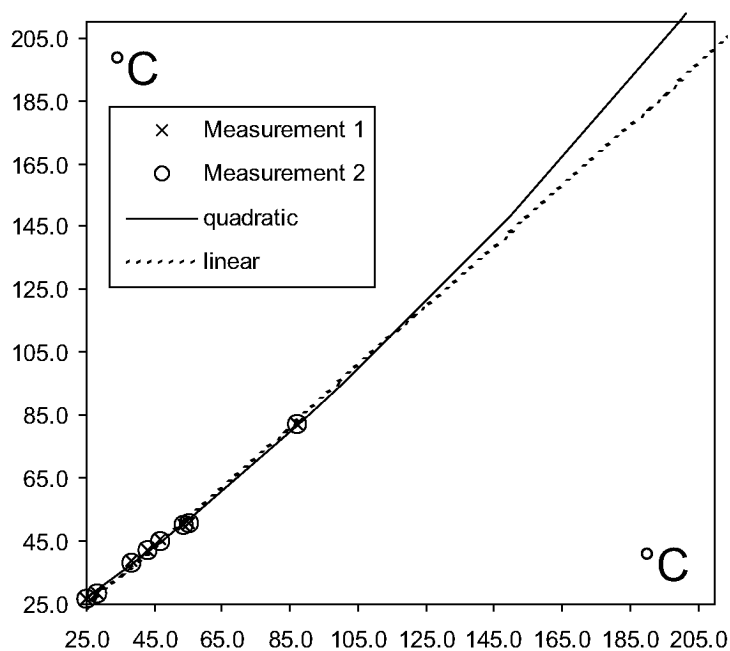
Figure 10.4: Temperature calibration of the two Pt100 sensors in the drift tube.
x: mercury thermometer, y: Pt100 1 resp. 2

For every data point a equilibration time of at least 5min after showing the constant target temperature was taken. A linear and a quadratic fit was performed to describe the dependence curve. All the absolute values of the temperatures and the fitting curves between 20 and 200°C showed a difference of less than 5%. Therefore the temperatures in the parameter tables in this work are presented uncorrected as the readout of the sensor sitting on the gas preheating tubes.

The 2D FT mobility data was visualized and worked up by MATLAB as described in section 4.3.2. For the single sweeps the time dependent signal was used as selection criteria for the data points averaging only the points in the plateau (s. figure 4.11 on page 71). For the multiple sweeps all points in the direction of time dependent domain were averaged.

To improve the spectra quality for the measurements with observable remaining signal at the end of the FID trace, especially the ones with lower S/N, a cosinus apodization was made.

For spectra with less than 500 data points beside the direct work up of the raw data points an additional trace work up with zero filling of up to 2000 points was made.

10.5.2   Serine Project

Substances

L-Serine	99%, FLUKA BioChemika Buchs CH
L-Threonine	99%, FLUKA BioChemika Buchs CH
L-Alanine	99%, FLUKA BioChemika Buchs CH
L-Isopropylserine	[(2S,3R)-(+)-2-Amino-3-hydroxy-4-methylpentanoic acid] 99%, Acros Organics NJ USA
L-Tert-butylserine	[L-Threo-tert-butylserine] 99%, Acros Organics NJ USA

L-Serine Solutions

Used solutions if not mentioned differently:

10^{-2}M l-serine in 49:49:2 MeOH/H$_2$O/AcOH

10^{-2}M l-serine in 49:49:2 MeCN/H$_2$O/AcOH

If not mentioned differently the machine settings were made as follows
(ranges optimized daily to obtain max. signal):

He experiments – TSQ1 (24–pole):		N$_2$ experiments – TSQ2 (8–pole):	
tf	*stdtune*	tf	*stdtune*
tl	100 V	tl	20–100 V (sig. opt.)
cap	DAC 5–6	cap	DAC 5–6
sfl	5–10 μl/min	sfl	4–7 μl/min
dist	+5 mm	dist	+3–5 mm
tv	4.0 kV	tv	4.0 kV
sp	8.6 kV	sp	9.5-9.8 kV
gfl	500 ml/min	gfl	1000 ml/min
tt	75°C	tt	50°C

Serine: Mixtures With Other Amino Acids

The measurements for the treonine mixtures were done with He as drift gas with settings and concentrations analog to l-serine settings.

Mixture: 9:1 ser:thr

tt raised 100°C instead of 75°C – try to increase resolution

The measurements for the unnatural amino acids were done with He and N_2 up to 100°C with settings and concentrations analog to l-serine settings.

For the unsuccessful mixtures the tl was scanned using a DAC scan while the other machine settings were made analog to the serine experiments. Mixing ratios between 50:1 and 1:50 were and temperatures between 50 and 100°C tested using He and N_2 as drift gas.

10.5.3   The Ethylene Polymerization Project

The DCC quenched ethylene polymerization products were produced by Fabio Dilena. The polymerizations were carried out in a glass pressure tube reactor similar to the described one for the iridium projectt with a coupled baratron for pressure and a flow meter for the ethylene uptake monitoring. Reactions at constant concentrations of 4 mg of the Zr–Ar catalyst in 6 ml of toluene and different defined temperatures were carried out. The toluene was preloaded by 12 eq of MAO in relation to the the catalyst and saturated at 2.0 bar of absolute ethylene pressure (saturation checked by the baratron). Then the catalyst was added and reacted at defined temperatures, pressures and reaction times. After the catalytic ethyl oligomerization reaction at defined pressure, temperature and reaction time the reaction was quenched upon addition of 25 eq DCC (dicyclohexyl carbodiimine) catching up the oligomer chain from the catalytic side to form stable species. For the mobility project three different experiments were selected to represent the three possble cases of product distributions (only odd, odd and even, only even chains) with the following conditions:

Nr	t [°C]	abs. pres. [bar]	rxn time [s]	monomer [M]
DCC-38	0	2.0	300	0.4
DCC-42	60	1.6	90	0.25
DCC-52	120	1.6	90	0.16

The quenching reaction forms usually the charged cis configured DCC-CnHm species of the catalyst bound chains in the living polymerization. The obtained product solution was then diluted by CH_2Cl_2 to obtain a 10^{-4}-10^{-5} M spraying solution. The resulting solutions were investigated using the LCQ classic MS with medium to high tube lens settings of 30-70 V and showed nice distribution "fishbones" of the polymerization products (s. figure 6.3 on page 105).

For the ion mobility measurements a further dilution of 1:50 with a 1:10 MeOH/CH_2Cl_2 had to be made to prevent the chlorine bridge dimer formation which has turned out to be the main product in the original solutions and to have the same conditions as for the final solutions of the "grignard" model compounds. The softer conditions of the drift tube did not cleave the dimers. Therefore also a low tube lens setting of 0-20 V on the TSQ was chosen to avoid post–fragmentation of the mobility separated species. Due to an electricity network frequency artefact at 20 ms laying in

the appearing range of the analyte peaks the tube voltage for the peak form integration measurements on the polymerization products had to be lowered to 5.35 kV.

Changed settings for the DDC project (N_2):

tf	*stdtune*
tl	0-20 V (optimized on signal intensity and dimer observation)
sfl	7–20 μl/min
dist	+4.5 mm
tv	6.0 and 5.35 kV (integration)
sp	10.0 and 9.35 kV (integration)

10.6 Ion Mobility and Structure Calculations

All calculations have been performed on AMD Athlon XP processors running RedHat 7.1 (32 bit) and Opteron (64 bit) processors running Fedora Core 2 using 64 bit compilations for the Opteron case. For MOBCAL additionally compilations on AMD Athlon processors running Windows 2000 and Cygwin[171] bash shell were used resulting in infinite results for the EHSS model due to a compiler issue but giving good results for the PA and TM model. The consistency of 64 bit, 32 bit and 32 bit Cygwin MOBCAL calculations was checked with multiple structures always giving good reliability.

The structures for the mobility calculations were calculated on PM3 and B3LYP level using Gaussian 03 rev. b03 using the following job headers:

Ammonium Ions and DCC Bound C_n Chains:

```
#p Becke3LYP/6-31G test pop=full opt gfinput gfprint
```

```
#p pm3 test pop=minimal opt gfinput gfprint
```

To test if a real minimum structure was found the keyword "freq=noraman" was added in most of the cases and checked subsequently for negative frequencies.

The resulting single structures were then prepared as MOBCAL input. The needed charge distributions were extracted from the Gaussian output taking the type including charges on H atoms.

For the mobility calculations of the ammonia ions with a *m/z* 284 two calculations sets were performed.

Set 1: $2.5*10^6$ EHSS traj. (inum=2'500'000), $2*10^4$ TM traj. (imp = 50)

Set 2: $2.5*10^6$ EHSS traj. (inum=2'500'000), $5*10^5$ TM traj. (imp = 1'250)

For the mobility calculations of the DCC bound C_n chains the calculations were made with:

$2.5*10^5$ EHSS traj. (inum=250'000), $2*10^5$ (imp=500).

The other TM values were kept at default values (itn=10, inp=40)

Part IV

Appendix

Appendix A

Nanospray Tests
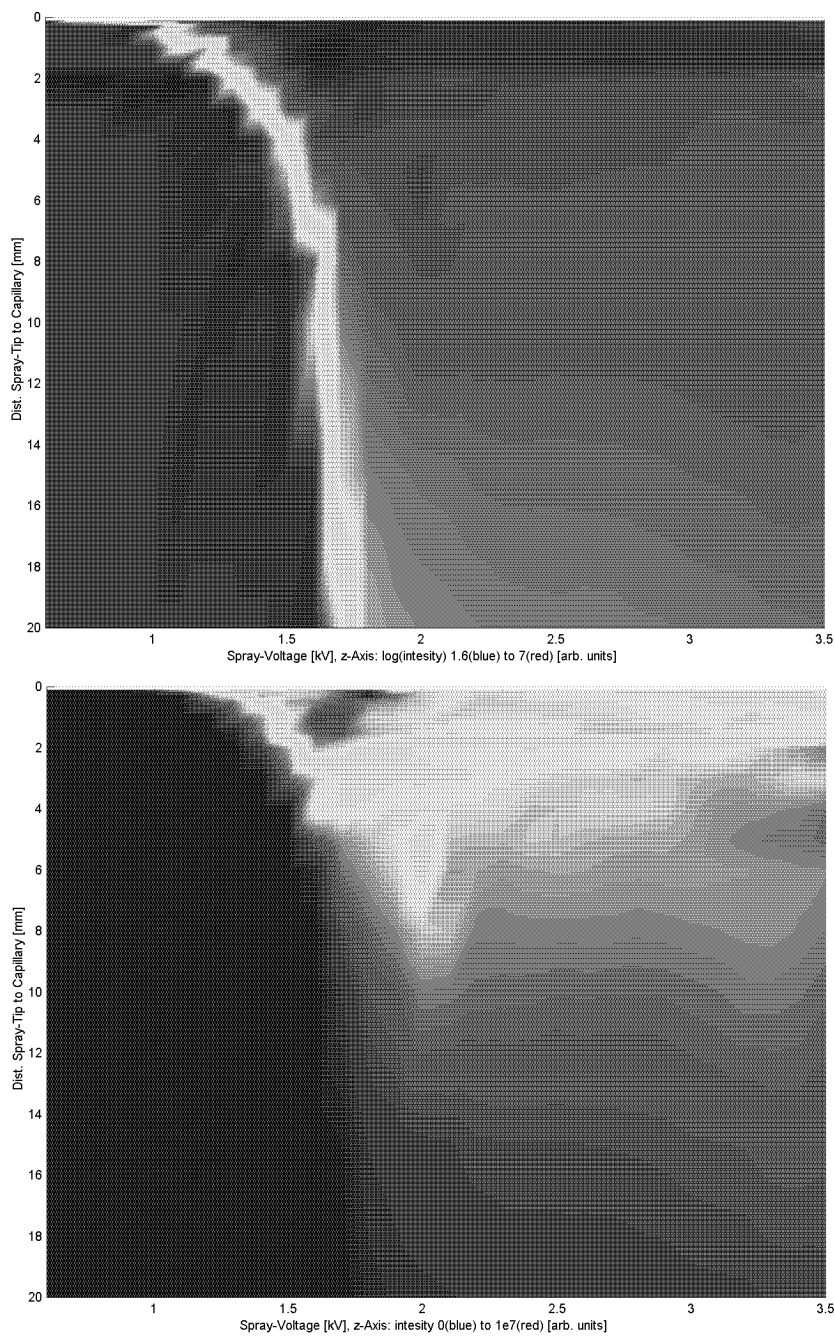
Figure A.1: Ion intensity versus spray voltage (x) and distance (y)
NBu$_4^+$ in MeOH, NewObjective nanospray 2μm.
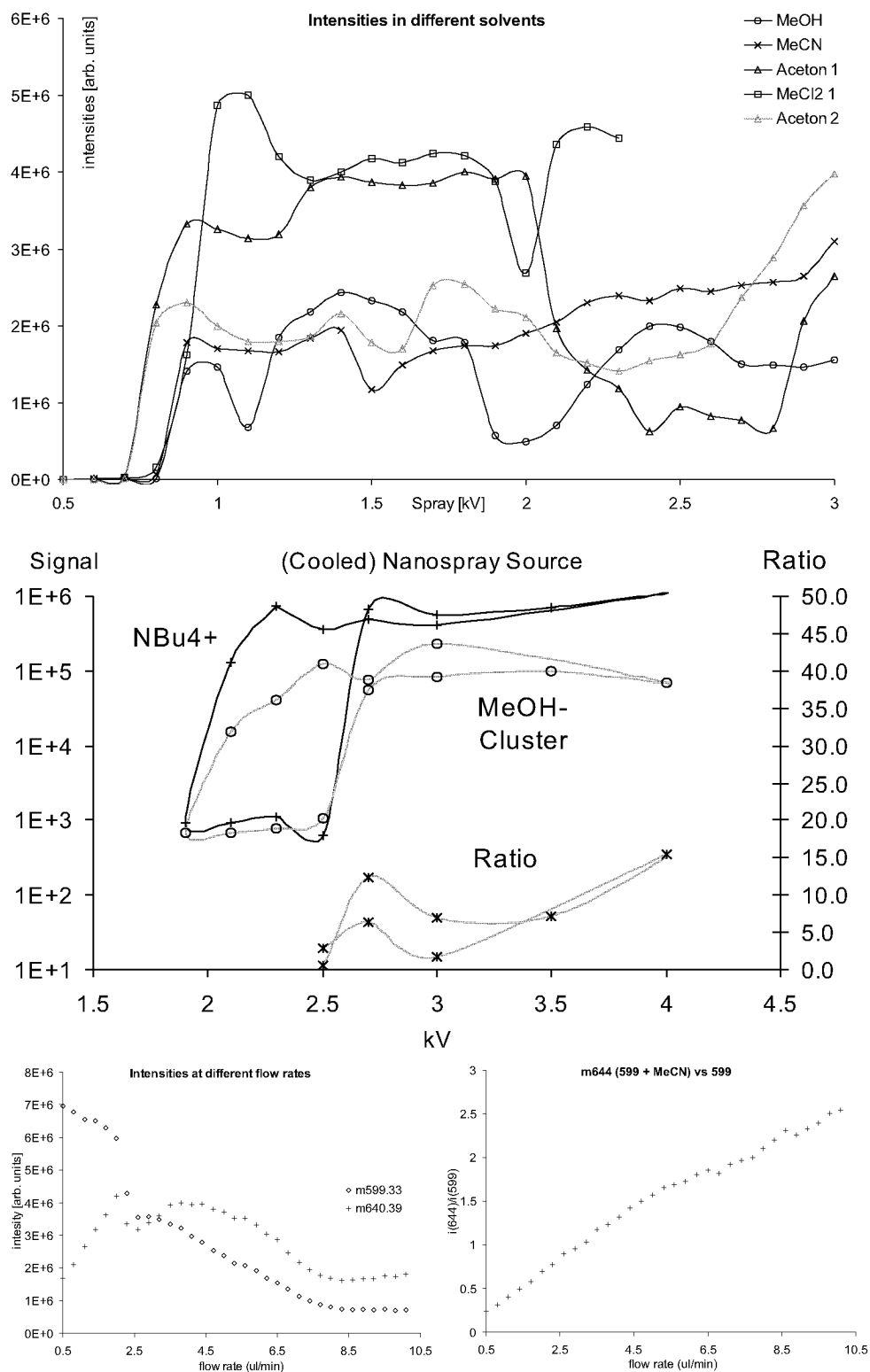
Figure A.2: Ion intensity under different conditions.
upper: Mn-Salene in different solvents at different spray voltages
middle: cyclic spray voltage dependency NBu_4^+ in MeOH
(e.g. "starting voltage effect")
lower: Mn-Salene in MeCN at different flow rates
(Mn-Salene vs. Mn-Salene-MeCN)

Appendix B

AdBasic Driver Programs

B.1   Mobility_One_Gate

AdBasic program for the one gate pulsing method.

```
******************************************
*      Proze{\ss}nummer = 1
*      Delay = 1000
*      Eventsource = 0
*      Number of Loops = 0
*      Priorit{\"a}t = 0
*      Version = 1
*      FastStop = 0
*      AdbasicVersion = 2000000
*      ATSRAM = 0
*      OPT_LEVEL = 2
*      SAVECOMPIL = 0
******************************************


DIM DATA_2[2048] AS INTEGER 'measurement in integer-values'
DIM DATA_3[2048] AS INTEGER 'gate-function'
DIM DATA_4[2048] AS INTEGER 'no of measurements'
DIM gates AS INTEGER        'gate-value'

'Time-Vars'
DIM timestep AS FLOAT       'resolution time-step [ms]'
DIM time AS FLOAT           'total time of flight [ms]'
DIM nsteps AS INTEGER       'number of timesteps'
DIM twindow AS INTEGER      'gate opening time [timesteps]'
DIM proct AS INTEGER        'process starting time [tcounts]
DIM twinmst AS INTEGER      'timestep [tcounts]

'Counters'
DIM i AS INTEGER
```

```
DIM j AS INTEGER
DIM imax AS INTEGER


REM FPAR_3=timestep, FPAR_4=time, FPAR_5=timewindow
REM 4 timesteps initial time (t0)


INIT:
DIGOUT_WORD(3)


'Definitionen, Einlesen:'
timestep = FPAR_3
time = FPAR_4


'( time = max 2000 x timestep )'
twindow = FPAR_5 / timestep
nsteps = (time / timestep)+ 4 + twindow
twinmst = timestep * 40000


EVENT:
 FOR j = 1 TO nsteps
  DATA_3[j] = 1
 NEXT j
 FOR j = 5 TO ( 4 + twindow )
  DATA_3[j] = 0
 NEXT j
 FOR i = 0 TO nsteps
  proct = READ_TIMER()
  gates = DATA_3[i]
  j = 0
  DO
   j = j + 1
   DIGOUT_WORD(gates)
   SET_MUX(0)
```

```
    START_CONV(1)
    WAIT_EOC(1)
    PAR_1 = READADC(1)
    DATA_2[i+1] = DATA_2[i+1] + ( PAR_1 - DATA_2[i+1] ) / j
    DATA_4[i+1] = j
  UNTIL (( READ_TIMER() - proct ) > twinmst )
 NEXT i
DIGOUT_WORD(3)
END
```

B.2   Mobility_Cut_Loop

AdBasic program for the two gate cutting method.

```
*****************************************
*      Proze{\ss}nummer = 1
*      Delay = 1000
*      Eventsource = 0
*      Number of Loops = 0
*      Priorit{\"a}t = 0
*      Version = 1
*      FastStop = 0
*      AdbasicVersion = 2000000
*      ATSRAM = 0
*      OPT_LEVEL = 2
*      SAVECOMPIL = 0
*****************************************


DIM DATA_2[2048] AS INTEGER 'measurement in integer-values'
DIM DATA_3[2048] AS INTEGER 'gate-function'
DIM DATA_4[2048] AS INTEGER 'no of measurements'
DIM gates AS INTEGER         'gate-value'


'Time-Vars'
DIM timestep AS FLOAT        'resolution time-step [ms]'
DIM time AS FLOAT            'total time of flight [ms]'
DIM nsteps AS INTEGER        'number of timesteps'
DIM twindow AS INTEGER       'gate opening time [timesteps]'
DIM timediff AS INTEGER
                   'time difference gate1 - gate2 [timesteps]'
DIM proct AS INTEGER         'process starting time [tcounts]
DIM twinmst AS INTEGER       'timestep [tcounts]
```

```
'Counters'
DIM i AS INTEGER
DIM j AS INTEGER
DIM imax AS INTEGER

INIT:
DIGOUT_WORD(3)

'Definitionen, Einlesen:'
timestep = FPAR_3
time = FPAR_4

'( time = max 1000 x timestep )'
twindow = FPAR_5 / timestep
nsteps = (time / timestep)+ 4 + twindow
twinmst = timestep * 40000
timediff = PAR_3 + 5            '5 timesteps initial time'

EVENT:
 FOR j = 1 TO nsteps
  DATA_3[j] = 3
 NEXT j
 FOR j = 5 TO ( 4 + twindow )
  DATA_3[j] = 2
 NEXT j
 FOR j = ( timediff ) TO ( timediff + twindow - 1)
  DATA_3[j] = DATA_3[j] - 2
 NEXT j
 FOR i = 0 TO nsteps
  proct = READ_TIMER()
  gates = DATA_3[i]
  j = 0
  DO
```

```
    j = j + 1
    DIGOUT_WORD(gates)
    SET_MUX(0)
    START_CONV(1)
    WAIT_EOC(1)
    PAR_1 = READADC(1)
    DATA_2[i+1] = DATA_2[i+1] + ( PAR_1 - DATA_2[i+1] ) / j
    DATA_4[i+1] = j
  UNTIL (( READ_TIMER() - proct ) > twinmst )
 NEXT i
DIGOUT_WORD(3)
END
```

B.3   Mobility_FT

AdBasic program for the two gate fourier transform method.

```
*****************************************
*       Proze{\ss}nummer = 1
*       Delay = 1000
*       Eventsource = 1
*       Number of Loops = 0
*       Priorit{\"a}t = 0
*       Version = 1
*       FastStop = 0
*       AdbasicVersion = 2000000
*       ATSRAM = 0
*       OPT_LEVEL = 0
*       SAVECOMPIL = 0
*****************************************


DIM DATA_2[1000] AS INTEGER 'measurement in integer-values'
DIM gates AS INTEGER        'gate-value'


'Freq-Vars'
DIM freq AS FLOAT       'actual frequence'


'Time-Vars'
DIM proct AS INTEGER            'process starting time [tcounts]'
DIM lenght AS INTEGER           'process length [ms]'
DIM hf AS FLOAT         'half frequency factor'


'Counters'
DIM i AS INTEGER
DIM j AS INTEGER
DIM k AS INTEGER
```

```
DIM n AS INTEGER            'number of measurements per point'
DIM nl AS INTEGER
DIM imax AS INTEGER

DIM a AS FLOAT
DIM b AS INTEGER

REM PAR_1 freqency [Hz]
REM PAR_2 readout signal
REM PAR_3 process length [ms]
REM PAR_4 number of measurements per point

INIT:

DIGOUT_WORD(3)

'Definitionen, Einlesen:'
freq = PAR_1
lenght = PAR_3
nl = lenght * 40000
n = lenght / 9.523  'exp'
PAR_4 = n
PAR_6 = nl
hf = freq / 4e7
FPAR_1 = hf
FOR i = 1 to 1000
DATA_2[i] = 32768
NEXT i

EVENT:

proct = READ_TIMER()
PAR_7 = proct
```

```
j = 0
DO
 j = j + 1
 PAR_2 = 0
 FOR i = 1 TO n
  a = ( READ_TIMER() - proct ) * hf
  b = a
  FPAR_2 = a - b
  IF ( FPAR_2 < 0.5 ) THEN
   DIGOUT_WORD(0)
  ELSE
   DIGOUT_WORD(3)
  ENDIF
  SET_MUX(0)
  START_CONV(1)
  WAIT_EOC(1)
  PAR_5 = READADC(1)
  PAR_2 = PAR_2 + PAR_5 / n
 NEXT i
 DATA_2[j] = PAR_2
 PAR_8 = READ_TIMER() - proct
UNTIL (( PAR_8 ) > nl )
DIGOUT_WORD(3)
END
```

Appendix C

LabView Driver Programs

C.1   Mobility_One_Gate001
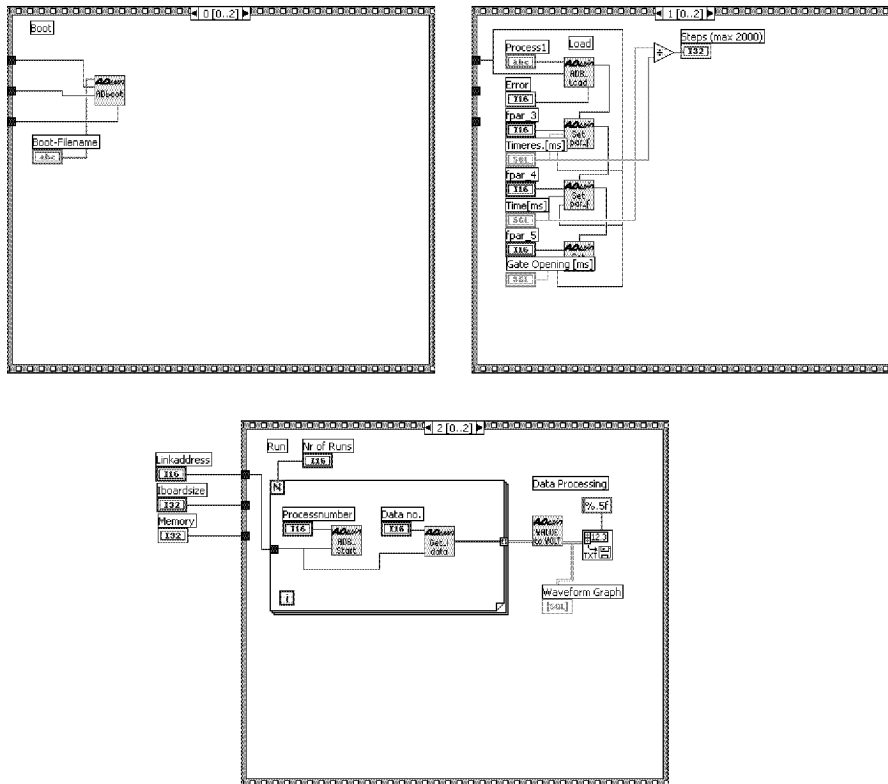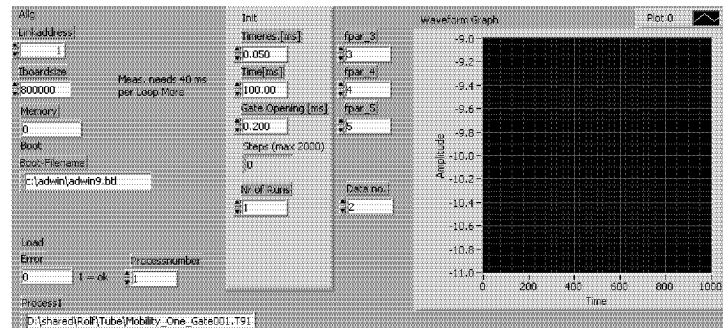
Figure C.1: LabView program for the one gate pulsing method using AdBasic
program Mobility_One_Gate.

C.2   Mobility_Cut_Loop001
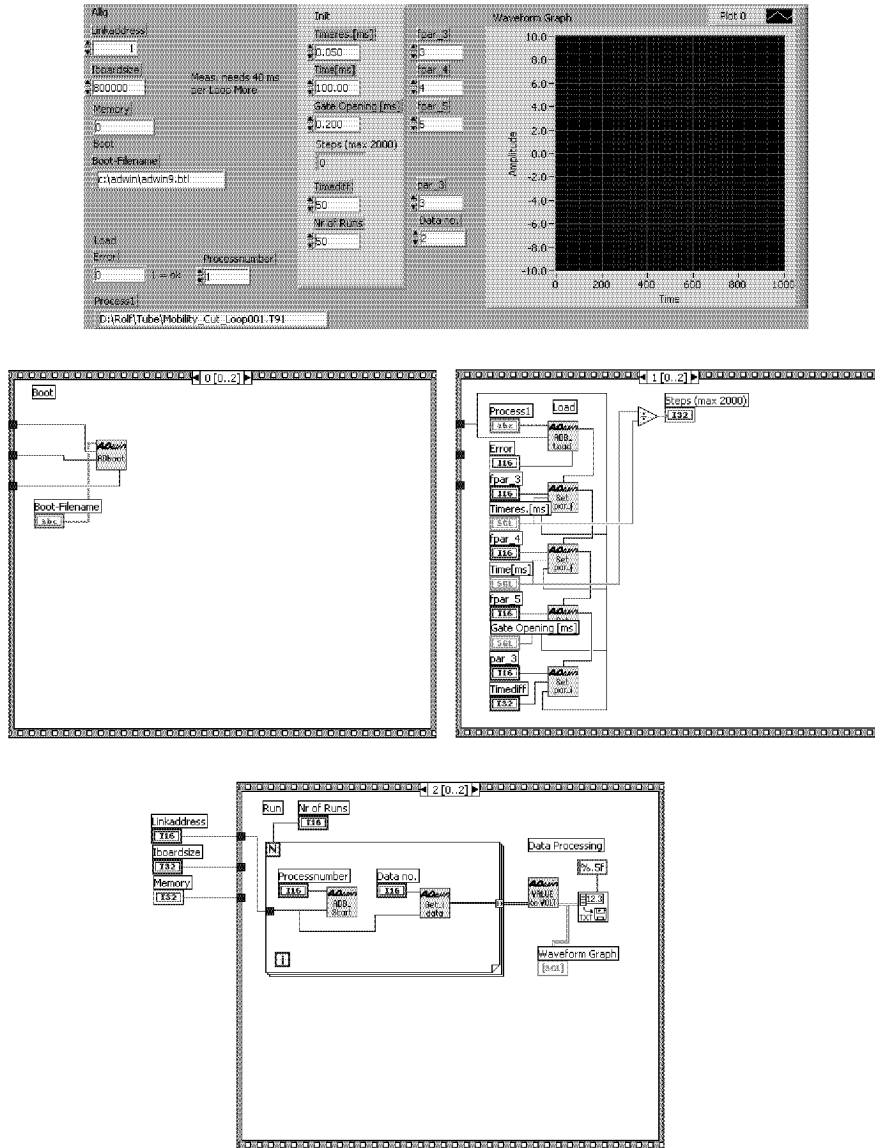
Figure C.2: LabView program for the two gate method cutting one fixed mo-
bility using AdBasic program Mobility_Cut_Loop.

C.3   Mobility_Cut_Sweep001
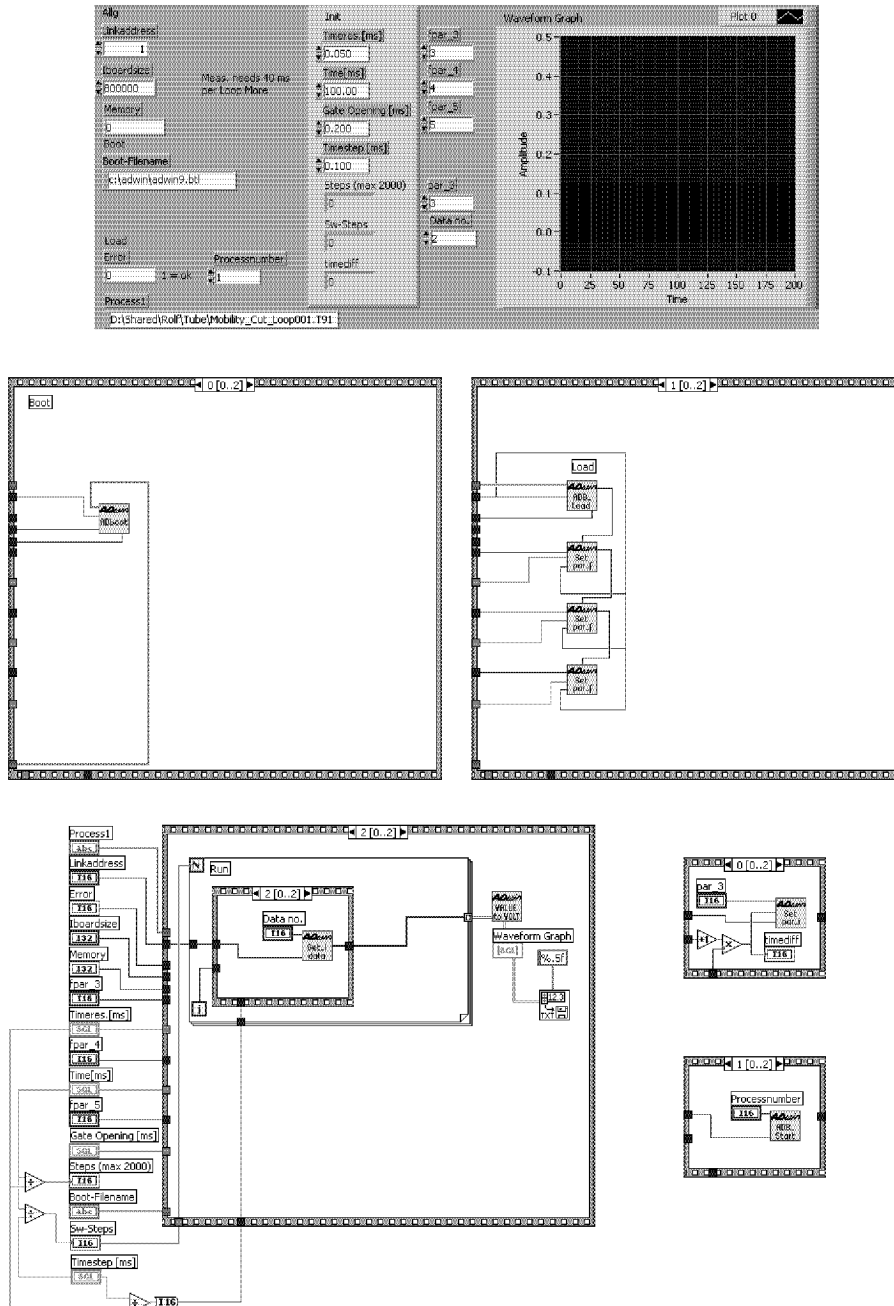
Figure C.3: LabView program for the two gate method sweeping the time difference using AdBasic program Mobility_Cut_Loop.

C.4   Mobility_FT_003_fil-v2
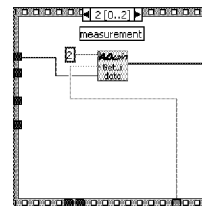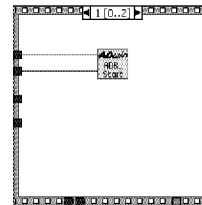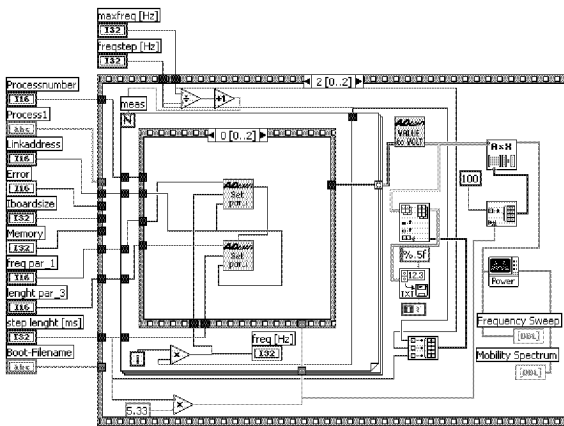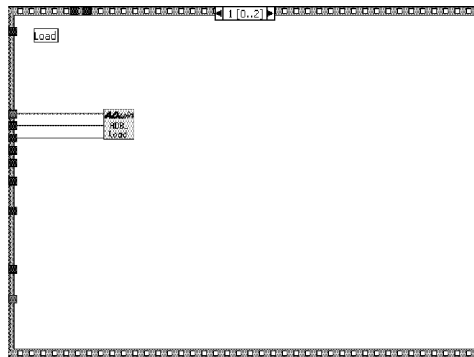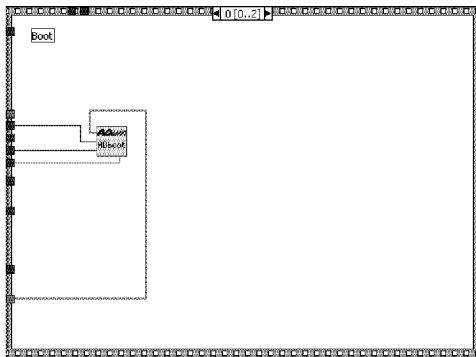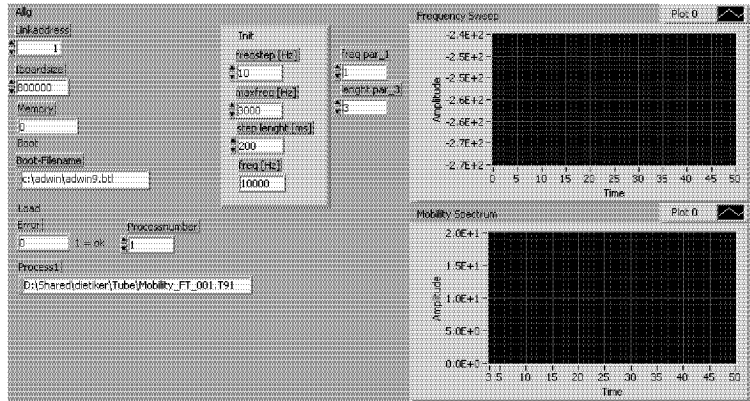
Figure C.4: LabView program for the two gate FT method using AdBasic
program Mobility_FT.

C.5 Mobility_FT_004_fil-v2
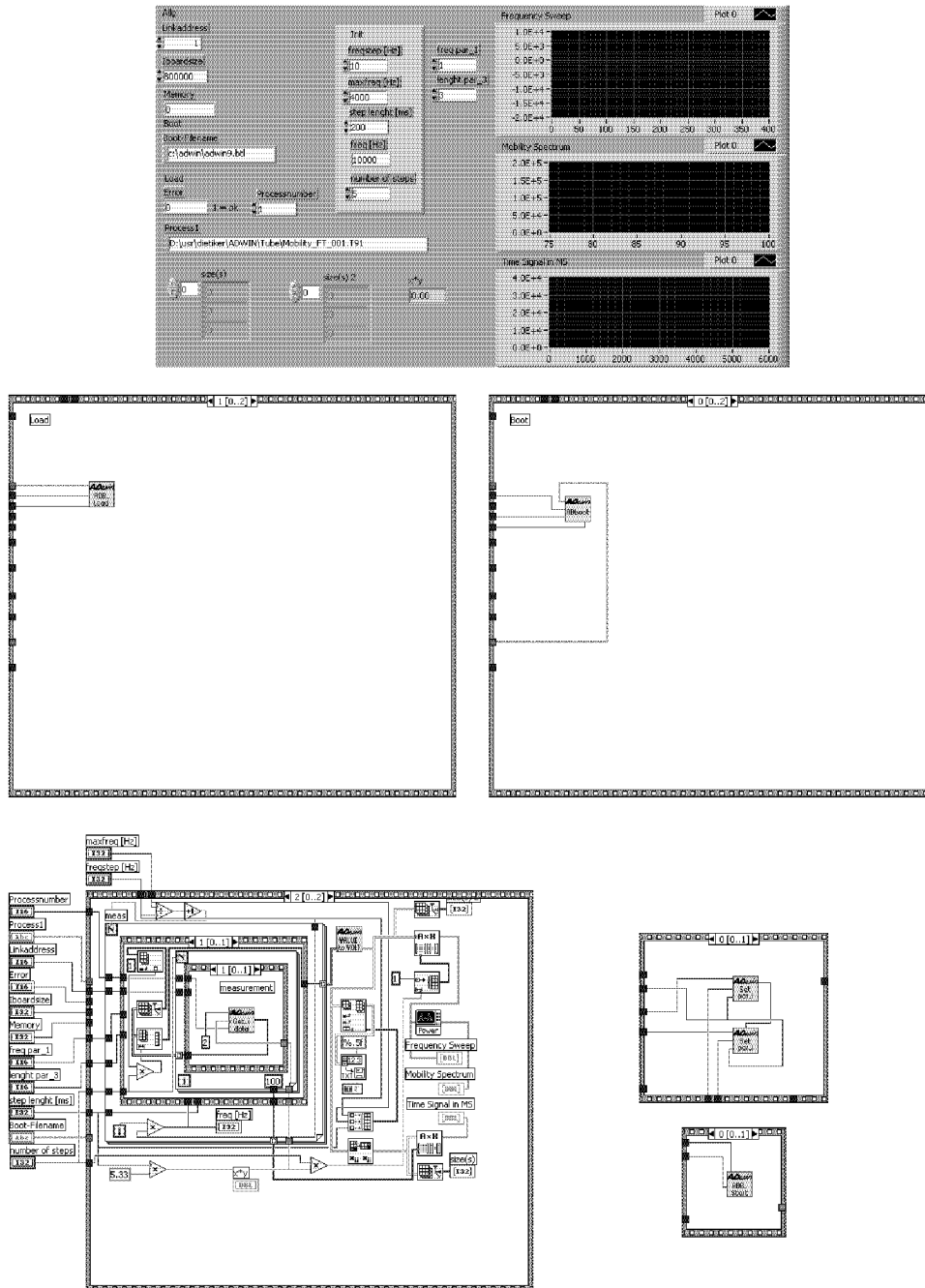
Figure C.5: LabView program for for the two gate FT method with additional averaging using AdBasic program Mobility_FT.

C.6 Direct_Gate_Driv_002-v2
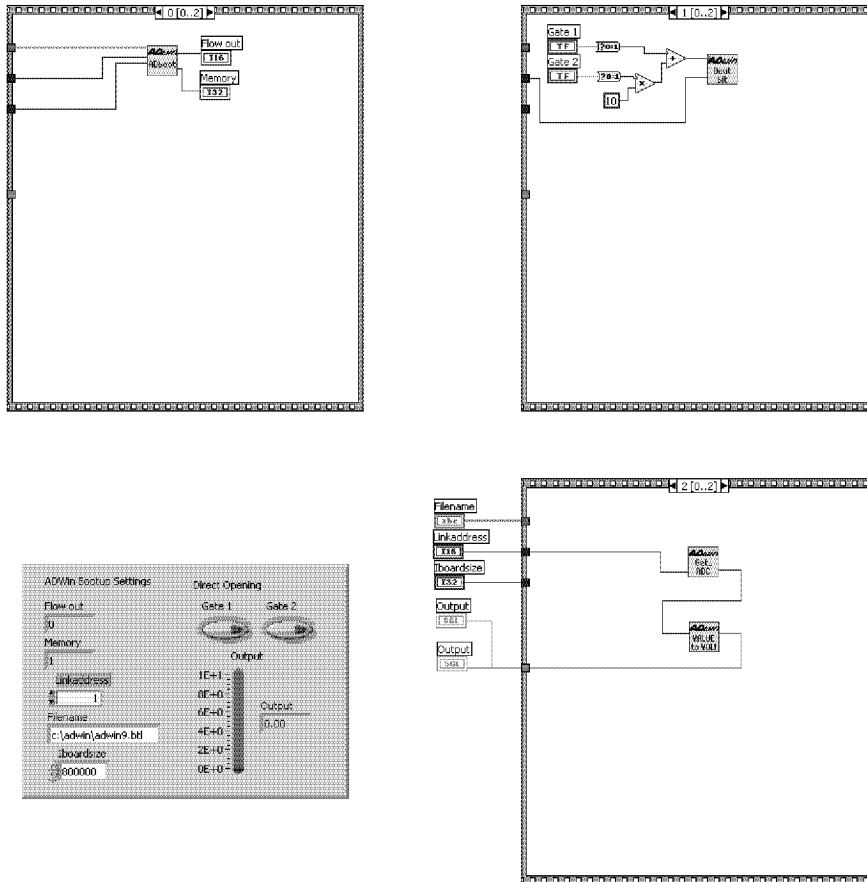
Figure C.6: LabView program for direct gate driving used for tests.

C.7 Direct_Gate_Driv_uni-v2
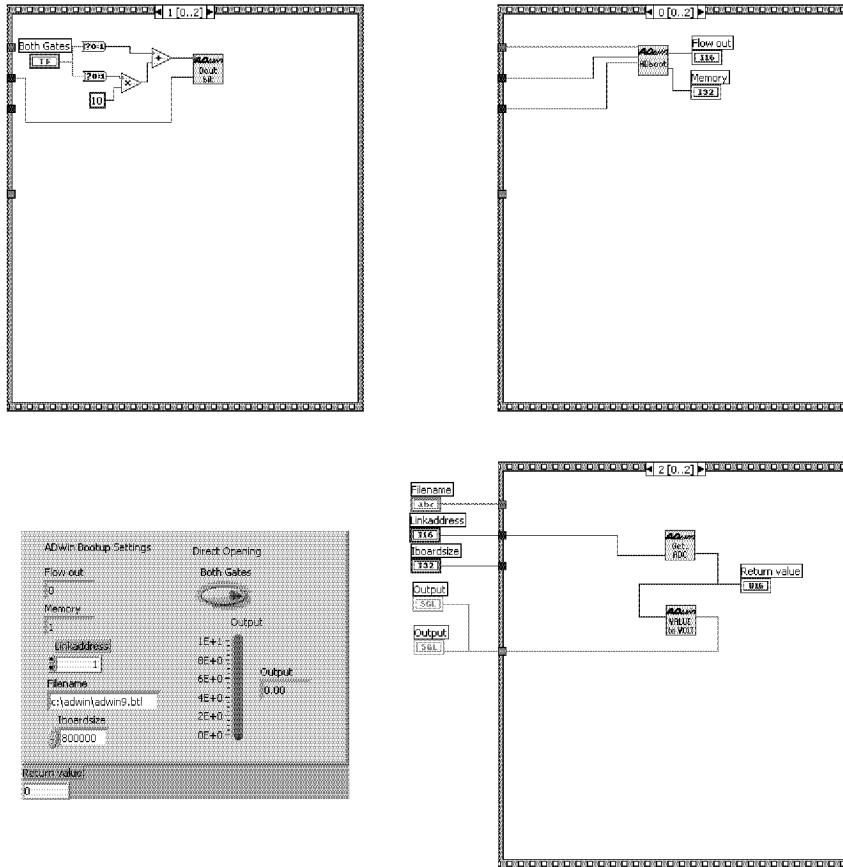
Figure C.7: LabView program for direct gate driving used tests (both gates driven simultaneously).

Bibliography

[1] G. Martino and J. P. Bôitiaux, *Actualite Chimique* **2002**, 7–11.

[2] P. Chen, *Angew. Chem. Int. Ed.* **2003**, *42*, 2832.

[3] D. Feichtinger and D. Plattner, *Chemistry-A European Journal* **2001**, *7*, 591–599.

[4] D. Feichtinger and D. Plattner, *Chemistry-A European Journal* **2001**, *7*, 591–599.

[5] C. Hinderling and P. Chen, *International Journal of Mass Spectrometry* **2000**, *195/196*, 377–383.

[6] C. Hinderling, D. Feichtinger, D. Plattner and P. Chen, *Journal Of The American Society For Mass Spectrometry* **1997**, *119*, 10793–10804.

[7] M. A. O. Volland, C. Adlhart, C. A. Kiener, P. Chen and P. Hofmann, *ChemistryA European Journal* **2001**, *7*, 4621–4632.

[8] C. Markert and A. Pfaltz, *Angew. Chem. Int. Ed* **2004**, *43*, 2498–2500.

[9] C. A. Srebalus, J. Li, W. S. Marshall and D. E. Clemmer, *Anal. Chem.* **1999**, *71*, 3918–3927.

[10] S. C. Henderson, S. J. Valentine, A. E. Counterman and D. E. Clemmer, *Anal. Chem.* **1999**, *71*, 291–301.

[11] C. Wu, W. F. Siems, G. R. Asbury and H. H. Hill Jr., *Anal. Chem.* **1998**, *70*, 4929–4938.

[12] P. Dugourd, R. R. Hudgins, D. E. Clemmer and M. F. Jarrold, *Rev. Scien. Inst.* **1997**, *68*, 1122–1129.

[13] J. C. Tabet, *Tetrahedron* **1987**, *43*, 3413–3420.

[14] W. Shen, P. S. H. Wong and R. G. Cooks, *Rapid Comm. Mass Spec.* **1997**, *11*, 71–74.

[15] W. A. Tao, D. Zhang, F. Wang, P. D. Thomas and R. G. Cooks, *Anal. Chem.* **1999**, *71*, 4427–4442.

[16] A. Paladini, C. Calcagni, T. Di Palma, M. Speranza, A. Lagana, G. Fago, A. Filippi, M. Satta, A. Guidoni and Giardini, *Chirality* **2001**, *13*, 707–711.

[17] W. A. Tao and R. G. Cooks, *Eur. J. Mass Spec.* **2002**, *8*, 107–115.

[18] P. Traldi, O. Curcuruto and O. Bortolini, *Rapid Comm. Mass Spec.* **1992**, *6*, 410–412.

[19] P. Traldi, S. Catinella and O. Bortolini, *Org. Mass Spec.* **1992**, *27*, 927–928.

[20] P. Traldi and F. D, *Rapid Comm. Mass Spec.* **1992**, *6*, 543–544.

[21] O. Bortolini and P. Traldi, *Rapid Comm. Mass Spec.* **1994**, *8*, 666–669.

[22] L. A. Gill, J. M. Wells, G. E. Patterson, J. W. Amy and R. G. Cooks, *Anal. Chem.* **1998**, *70*, 4448–4452.

[23] T. Felder, C. Schalley, H. Fakhrnabavi and O. Lukin, *Chemistry-A European Journal* **2005**, *11*, 5625–5636.

[24] C. Adlhart and P. Chen, *J. Am. Chem. Soc.* **2004**, *126*, 3496.

[25] G. Gerdes, *Catalytic C-H Activation of Benzene by Platinum(II): A Mechanistic Study*, Ph.D. thesis, ETH, **2004**, http://e-collection.ethbib.ethz.ch/ecol-pool/diss/fulltext/eth15631.pdf.

[26] G. Gerdes and P. Chen, *Organometallics* **2004**, *23*, 3031.

[27] R. Hartmann, *Investigations on the Ru-catalyzed Asymmetric Hydrogenagion of Ketones*, Ph.D. thesis, ETH, **2003**, http://e-collection.ethbib.ethz.ch/ecol-pool/diss/fulltext/eth15231.pdf.

[28] C. Adlhart, *Intrinsic Reactivity of Ruthenium Carbenes: A Combined Gas Phase and Computational Study*, Ph.D. thesis, ETH, **2003**, http://e-collection.ethbib.ethz.ch/ecol-pool/diss/fulltext/eth15073.pdf.

[29] X. Zhang, X. Chen and P. Chen, *Organometallics* **2004**, *23*, 3437.

[30] R. Dietiker and P. Chen, *Angew. Chem. Int. Ed.* **2004**, *43*, 5513.

[31] E. Schön, X. Zhang, Z. Zhou, M. Chisholm and P. Chen, *Inorg. Chem.* **2004**, *43*, 7278.

[32] X. Zhang and P. Chen, *Chem. Eur. J.* **2003**, *9*, 1852.

[33] G. Gerdes and P. Chen, *Organometallics* **2003**, *22*, 2217.

[34] C. Adlhart, M. A. O. Volland, P. Hofmann and P. Chen, *Helvetica Chimica Acta* **2000**, *83*, 3306–3311.

[35] C. Adlhart and P. Chen, *Helvetica Chimica Acta* **2000**, *83*, 2192–2196.

[36] C. Adlhart, C. Hinderling, H. Baumann and P. Chen, *Journal of the American Chemical Society* **2000**, *122*, 8204–8214.

[37] D. H. K. Feichtinger, *Untersuchung der intrinsischen Reaktivität von metallorganischen Katalysatoren mittels Elektrospray Tandem Massenspektrometrie.*, Ph.D. thesis, ETH, **2000**, http://e-collection.ethbib.ethz.ch/ecol-pool/diss/fulltext/eth13595.pdf.

[38] P. Chen and C. Hinderling, *(Thales Technologies, A.-G., Switz.). PCT Int. Appl.* **2000**, 36 pp.

[39] C. Hinderling, C. Adlhart and P. Chen, *Chimia* **2000**, *54*, 232–235.

[40] J. El-Bahraoui, O. Wiest, D. Plattner and D. Feichtinger, *Abstracts of Papers of The American Chemical Society* **2000**, *220*, 110.

[41] C. R. Hinderling, *Elektrospray-Tandem-Massenspektrometrie als vielseitiges Werkzeug zum mechanistischen Studium von organometallischen Reaktionen*, Ph.D. thesis, ETH, **1999**, http://e-collection.ethbib.ethz.ch/ecol-pool/diss/fulltext/eth13158.pdf.

[42] Y.-M. Kim, *A study of cationic rhodium complexes in the gas phase by electrospray ionization mass spectrometry. Towards a model of the diamond surface.*, Ph.D. thesis, ETH, **1999**.

[43] W. S. Barnes, D. W. Martin and E. W. McDaniel, *Phys. Rev. Lett.* **1961**, *6*, 110–111.

[44] A. Blanc, *Compt. rend.* **1909**, *147*, 39–42.

[45] M. Dole, R. L. Hines, R. C. Mack, R. C. Mobley, L. D. Ferguson and M. Alice, *J. Chem. Phys.* **1968**, *49*, 2240–2249.

[46] C. Wu, W. E. Steiner, P. S. Tornatore, L. M. Matz, W. F. Siems, D. A. Atkinson and H. H. H. Jr, *Talanta* **2002**, *57*, 123134.

[47] Z. Eiceman, Gary Alan; Karpas, *Ion mobility spectrometry*, CRC, Boca Raton, Fla., **1994**.

[48] SwissCam or "CNG", chemical agent monitor - CAM, Smiths Detection, Watford UK.

[49] C. A. Srebalus Barnes, A. E. Hilderbrand, S. J. Valentine and D. E. Clemmer, *Anal. Chem.* **2002**, *74*, 26–36.

[50] E. Badman, H.-H. CS and C. DE, *Journal Of The American Society For Mass Spectrometry* **2002**, 719–723.

[51] S. J. Valentine, M. Kulchania, C. A. Srebalus Barnes and D. E. Clemmer, *Int. J. Mass Spectrom.* **2001**, *212*, 97–109.

[52] C. S. Hoaglund-Hyzer and D. E. Clemmer, *Anal. Chem.* **2001**, *73*, 177–184.

[53] R. Guevremont and R. Purves, *Journal Of The American Society For Mass Spectrometry* **2005**, *16*, 349–362.

[54] R. Purves, R. Guevremont, S. Day, C. Pipich and M. Matyjaszczyk, *Review Of Scientific Instruments* **1998**, *69*, 4094–4105.

[55] H. E. Revercomb and E. A. Mason, *Anal. Chem.* **1975**, *47*, 970.

[56] Y. Liu, S. J. Valentine, A. E. Counterman, C. S. Hoaglund and C. D. E., *Analytical Chemistry News & Features* **1997**, *Dec 1*, 728–735.

[57] D. Wittmer, Y. H. Chen, B. K. Luckenbill and H. H. Hill, Jr., *Anal. Chem.* **1994**, *66*, 2348–2355.

[58] E. G. Stone, K. J. Gillig, B. T. Ruotolo and D. H. Russell, *International Journal of Mass Spectrometry* **2001**, *212*, 519533.

[59] B. T. Ruotolo, K. J. Gillig, E. G. Stone, D. H. Russell, K. Fuhrer, M. Gonin and J. A. Schultz, *International Journal of Mass Spectrometry* **2002**, *1-15*, 12026.

[60] J. Hunter and M. F. Jarrold, *J. Phys. Chem.* **1993**, *96*, 3460–3462.

[61] M. F. Jarrold and J. E. Bowers, *J. Chem. Phys.* **1992**, *96*, 9180–9190.

[62] M. F. Jarrold, J. E. Bowers and K. Creegan, *J. Chem. Phys.* **1989**, *90*, 2889–2896.

[63] S. Lee, G. N., G. von Helden and M. T. Bowers, *J. Phys. Chem.* **1997**, *101*, 2096–2102.

[64] M. T. Bowers, P. R. Kemper, H. G. and P. A. M. van Koppen, *Int. J. of Mass Spec. and Ion Proc.* **1993**, *123*, 1446–1451.

[65] R. E. Tosh and R. Johnsen, *Int. J. of Mass Spec. and Ion Proc.* **1993**, *123*, 193–203.

[66] C. D. Valentine SJ, Counterman AE, *Journal Of The American Society For Mass Spectrometry* **1997**, *8*, 954–961.

[67] A. J. Illies, *J. Phys. Chem.* **1988**, *92*, 2889–2896.

[68] A. Hilderbrand, S. Myung, C. Barnes and et al., *Journal Of The American Society For Mass Spectrometry* **2003**, *14*.

[69] A. C. Gill, K. R. Jennings, T. Wyttenbach and M. T. Bowers, *Int. J. Mass. Spec.* **2000**, *195/196*, 685–697.

[70] J. LK, K. CM and B. M, *J. Am. Chem. Soc.* **1995**, *117*, 6414–6415.

[71] T. Ziegler, *Angew. Chem. Int. Ed.* **1959**, *71*, 623–625.

[72] A. L. Burlingame, R. K. Boyd and S. J. Gaskell, *Anal Chem.* **1998**, *70*, 647R–716R.

[73] M. Yamashita and J. B. Fenn, *J. Phys. Chem.* **1984**, *88*, 4451–4459.

[74] M. Yamashita and J. B. Fenn, *J. Phys. Chem.* **1984**, *88*, 4671–4675.

[75] J. B. Fenn, M. Mann, C. K. Meng, S. F. Wong and C. M. Whitehouse, *Science* **1989**, *246*, 64–71.

[76] M. Karas, D. Bachmann, U. Bahr and F. Hillenkamp, *Int. J. Mass Spectrom. Ion Process.* **1987**, *78*, 53.

[77] R. D. Cole, *Electrospray ionization mass spectrometry*, John Wiley, New York, **1997**.

[78] A. P. Snyder, *Biochemical and Biotechnological Applications of Electrospray Ionization Mass Spectrometry*, volume 619 of *ACS Symposium Series*, ACS, Washington a. o., **1996**.

[79] W. Henderson, B. K. Nicholson and L. J. McCaffrey, *Polyhedron* **1998**, *17*, 4291–4313.

[80] D. A. Plattner, *Int. J. Mass Spectrom.* **2001**, *207*, 125–144.

[81] G. Siuzdak, B. Bothner, M. Yeager, C. Brugidou, C. M. Fauge, K. Hoey and C.-M. Chang, *Chem. Biol* **1996**, *3*, 45–48.

[82] P. Kebarle and L. Tang, *Anal. Chem.* **1993**, *65*, 972A–986A.

[83] J. B. Fenn, *J. Am. Soc. Mass Spectrometry* **1993**, *4*, 524–535.

[84] G. Schmelzeisen-Redeker, L. Bütfering and F. W. Röllgen, *Int. J. Mass Spectrom. Ion Proc.* **1989**, *90*, 139–150.

[85] J. V. Iribarne and B. A. Thomson, *J. Chem. Phys.* **1976**, *64*, 2287–2294.

[86] B. A. Thomson and J. V. Iribarne, *J. Chem. Phys.* **1979**, *71*, 4451–4463.

[87] M. Wilm and M. Mann, *Anal. Chem.* **1996**, *68*, 1–8.

[88] J. Appell, *Collision spectroscopy*, Plenum, New York, pages 252–256, a similar derivation for the loss of kinetic energy in an inelastic collision can be found here.

[89] G. R. Asbury and H. H. Hill Jr., *Anal. Chem.* **2000**, *72*, 580–584.

[90] D. Wittmer, Y. H. Chen, B. K. Luckenbill and H. H. Hill Jr., *Anal. Chem.* **1994**, *66*, 2348–2355.

[91] C. S. Creaser, M. Benyezzar, J. R. Griffiths and J. W. Stygall, *Anal. Chem.* **2000**, *72*, 2724–2729.

[92] D. F. Hagen, *Anal. Chem.* **1979**, *51*, 871.

[93] M. F. Mesleh, J. M. Hunter, A. A. Shvartsburg, G. C. Schatz and M. F. Jarrold, *J. Phys. Chem. A* **1997**, *101*, 968.

[94] M. F. Mesleh, J. M. Hunter, A. A. Shvartsburg, G. C. Schatz and M. F. Jarrold, *J. Phys. Chem.* **1996**, *100*, 16082.

[95] P. Dugourd, R. R. Hudgins, D. E. Clemmer and M. F. Jarrold, *Rev. Sci. Instrum.* **1997**, *68*, 1122.

[96] G. von Helden, M. T. Hsu, N. G. Gotts and M. T. Bowers, *J. Phys. Chem.* **1993**, *97*, 8182.

[97] G. von Helden, M. T. Hsu, N. G. Gotts, P. R. Kemper and M. T. Bowers, *Chem. Phys. Lett.* **1993**, *204*, 15.

[98] E. J. Mack Jr., *Am. Chem. Soc.* **1925**, *47*, 2468.

[99] A. A. Shvartsburg and M. F. Jarrold, *Chem. Phys. Lett.* **1996**, *86*, 261.

[100] E. A. Mason and H. W. Champ, *Ann. Phys.* **1958**, *4*, 233–269.

[101] H. B. Milloyt and R. Robson, *J. Phys. B: Atom. Molec. Phys.* **1973**, *6*, 1139–1152.

[102] A. A. Shvartsburg, B. Liu, M. F. Jarrold and K. M. Ho, *J. Chem. Phys.* **2000**, *112*, 4517.

[103] A. A. Shvartsburg, B. Liu, K. W. M. Siu and K.-M. Ho, *J. Phys. Chem. A* **2000**, *104*, 6152–6157.

[104] M. F. Mesleh, J. M. Hunter, A. A. Shvartsburg, G. C. Schatz and M. F. Jarrold **1996**, p: MOBCAL - A Program to Calculate Mobilities, Jarrold, University of Indiana, Chemistry, Indiana USA, http://nano.chem.indiana.edu/software/mobcal.tar.gz.

[105] R. R. Hudgins, Y. Mao, M. A. Ratner and M. F. Jarrold, *Anal. Chem* **1998**, *7*, 4111–4119.

[106] B. CAS and C. DE, *Anal. Chem.* **2001**, *73*, 424–433.

[107] N. E. Bradbury and R. A. Nielsen, *Phy. Rev.* **1936**, *49*, 388.

[108] F. J. Knorr, R. L. Eatherton, W. F. Siems and H. H. Hill, Jr., *Anal. Chem.* **1985**, *57*, 402–406.

[109] **2001**, p: MathCAD 2001i Professional, Mathsoft Engineering & Education Inc., USA.

[110] A. V. Oppenheim, R. W. Schafer and J. R. Buck, *Discrete-Time Signal Processing*, **1999**.

[111] **2004/5**, p: MATLAB 6r13/7r14, The Mathworks Inc., 3 Apple Hill Drive, Natick MA 01760-2098, USA.

[112] D. A. Dahl **1995**, p: SIMION 3D 6.0, Lockheed Idaho Technologies Company, Idaho Falls, Idaho, USA.

[113] W. E. Steiner, W. A. English and H. H. Hill, *Analytica Chimica Acta* **2005**, *532*, 3745.

[114] **2002**, p: LabView 6.1, National Instruments, Austin, Texas, USA.

[115] **2003**, p: AdBasic 3.2, Jäger GmbH, Lorsch, Germany.

[116] J. J. P. Stewart, *J. Comp. Chem.* **1989**, *10*, 209.

[117] P. Hohenberg and W. Kohn, *Phys. Rev.* **1964**, *136*, B864.

[118] A. D. Becke, *J. Chem. Phys.* **1993**, *98*, 5648.

[119] **2003**, p: Gaussian 03 Rev. B.03, Gaussian, Inc., Pittsburgh PA, USA.

[120] L. Charles, D. Pepin, F. Gonnet and F. Tabet, *Journal Of The American Society For Mass Spectrometry* **2001**, *12*, 1077–1084.

[121] S. A. Godleski, B. M. Trost, I. Fleming and M. F. Semmelhack, *Comprehensive Organic Synthesis*, volume 4, Pergamon, Oxford, **1991**.

[122] B. M. Trost and D. L. V. Vranken, *Chem. Rev.* **1996**, *96*, 395.

[123] A. Pfaltz, M. Lautens, M. F. Semmelhack, E. N. Jakobsen, A.Pfaltz and H. Yamamoto, *Comprehensive Asymmetric Catalysis*, volume 2, Springer, Heidelberg, **1999**.

[124] M. Perry, X. Cui, Powell.M.T., D. Hou, J. Reibenspies and K. Burgess, *Helv. Chim. Acta* **2000**, *83*, 2287–2294.

[125] Z. Takats, S. C. Nanita, G. Schlosser, K. Vekey and R. G. Cooks, *Anal. Chem.* **2003**, *75*, 6147–6154.

[126] R. Hodyss, R. R. Julian and J. L. Beauchamp, *Chirality* **2001**, *13*, 703–706.

[127] D. Zhang, K. J. Koch, A. Tao and R. G. Cooks, *Proceedings of the 48th ASMS Conference on Mass Spectrometry and Allied Topics* **2000**, 1361–1362.

[128] M. Quack, *ngew. Chem., Int. Ed. Engl.* **1989**, *28*, 571–586.

[129] A. Hirabayashi, M. Sakairi and H. Koizumi, *Anal. Chem.* **1994**, *66*, 4557–4559.

[130] K. J. Koch, F. C. Gozzo, D. Zhang, M. N. Eberlin and R. G. Cooks, *Chem. Commun.* **2001**, 1854–1855.

[131] A. E. Counterman and D. E. Clemmer, *J. Phys. Chem.* **2001**, *105*, 8092–8096.

[132] U. Mazurek, O. Geller, C. Lifshitz and et al., *Journal Of Physical Chemistry A* **2005**, *109*, 2107–2112.

[133] P. Flory, *J. Am. Chem. Soc.* **1940**, *62*, 1561.

[134] S. Tobisch and T. Ziegler, *J. Am. Chem. Soc.* **2004**, *126*, 9059–9071.

[135] D. Vogt, B. Cornils and W. A. Herrmann, *Oligomerization of Ethylene to Higher Linear R-Olefins. In Applied Homogeneous Catalysis with Organometallic Complexes*, VCH, Weinheim, Germany, **2002**.

[136] G. C. Eastmond, A. Ledwith, S. Russo and P. Sigwalt, *ComprehensiVe Polymer Science*, volume 4, Pergamon, Oxford, U.K., **1989**.

[137] K. Weissermal and H.-J. Arpe, *Important Raw Materials and Intermediates in Industrial Organic Chemistry*, VCH, Weinheim, Germany, **1978**.

[138] W. Kaminsky, *Catalysis Today* **1994**, *20*, 257–271.

[139] F. di Lena, E. Quintanilla and P. Chen., *Chem. Comm.* **2005**, *46*, 5757–5759.

[140] **2004/5**, p: Origin 6.1, OriginLab Corporation, One Roundhouse Plaza, Northampton MA 01760, USA.

[141] C. M. Matz, W. E. Steiner, B. H. Clowers and H. H. Hill, *International Journal of Mass Spectrometry* **2002**, *213*, 191202.

[142] G. Helmchen and A. Pfaltz, *Acc. Chem. Res.* **2000**, *33*, 336.

[143] J. Pfaltz, A.; Blankenstein, R. Hilgraf, E. Hörmann, S. McIntyre, F. Menges, M. Schönleber, S. Smidt, B. Wüstenberg and N. Zimmermann, *Adv. Synth. Cat.* **2003**, *33*, 345.

[144] D. Blackmond, A. Lightfoot, A. Pfaltz, T. Rosner, P. Schnider and N. Zimmermann, *Chirality* **2000**, *12*, 442.

[145] A. Lightfoot, P. Schnider and A. Pfaltz, *Angew. Chem. Int. Ed. Engl.* **1998**, *37*, 2897.

[146] G. Helmchen and A. Pfaltz, *Acc. Chem. Res.* **2000**, *33*, 336.

[147] R. Crabtree, *Acc. Chem. Res.* **1979**, *12*, 331.

[148] P. Brandt, C. Hedberg and A. P.G., *Chem. Eur. J.* **2000**, *9*, 339.

[149] L. Vázquez-Serrano, B. Owens and J. Buriak, *Chem. Comm.* **2002**, 2518.

[150] R. Crabtree, M. Mellea and J. Quirk, *J. Chem. Soc. Chem. Comm.* **1981**, 1217.

[151] D. Drago, P. Pregosin and A. Pfaltz, *Chem. Comm.* **2002**, 286.

[152] R. Crabtree, M. Lavin and L. Bonneviot, *J. Am. Chem. Soc.* **1986**, *108*, 4032.

[153] A. Goldman and J. Halpern, *J. Am. Chem. Soc.* **1987**, *109*, 7537.

[154] J. Brown, A. Derome, G. Hughes and P. Monaghan, *Aust. J. Chem.* **1992**, *45*, 143.

[155] E. Brunner, *Ber. Bunsenges. Phys. Chem.* **1979**, *83*, 715.

[156] M. Perry, X. Cui, Powell.M.T., D. Hou, J. Reibenspies and K. Burgess, *J. Am. Chem. Soc.* **2003**, *125*, 113.

[157] D. Hou, J. Reibenspies, T. Colacot and K. Burgess, *Chem. Eur. J.* **2001**, *7*, 5391.

[158] R. G. Cooks and T. L. Kruger, *J. Am. Chem. Soc.* **1977**, *99*, 1279.

[159] M. T. Rodgers and P. B. Armentrout, *Mass Spectrometry Reviews* **2000**, *19*, 215–247.

[160] K. Holbrook, M. Pilling and S. Robertson, *Unimolecular Reactions*, Wiley, Chichester, 2nd edition, **1996**, page 103.

[161] N. F. Dalleska, K. Honma and P. B. Armentrout, *J. Chem. Phys.* **1989**, *90*, 5466, p: CRUNCH – versions 4D (04/199D), D (4.1200D), D1 (4.1600D).

[162] L. S. Kassel, *J. Phys. Chem.* **1928**, *32*, 225.

[163] D. Gerlich, *Adv. Chem. Phys.* **1992**, *82*, 1.

[164] D. Feichtinger **1998**, p: TSQReader – version 1.0, Chen-Group, LOC, ETH Zurich, Switzerland.

[165] M. B. More, D. Ray and P. B. Armentrout, *J. Am. Chem. Soc.* **1999**, *121*, 417– 423.

[166] X. Zhanga, S. Narancic and P. Chen, *Organometallics* **2005**, *24*, 3040 – 3042.

[167] L. A. Hammad, G. Gerdes and P. Chen, *Organometallics* **2005**, *24*, 1907 – 1913.

[168] P. Chen, M. H. Chisholm, J. C. Gallucci, X. Zhang and Z. Zhou, *Inorg. Chem.* **2005**, *44*, 2588 – 2595.

[169] B. N. Praminik, A. K. Ganguly and M. L. Gross, *Applied Electrospray Mass Spectrometry*, volume 32 of *Practical Spectroscopy Series*, Marcel Dekker, Inc., New York, Basel, **2002**.

[170] M. T. Bowers, *Gas phase ion chemistry, 3 vols.*, Academic Press, New York, **1979-1984**.

[171] **2005**, p: CygWin 1.5.18-1 bash shell, free for download at http://cygwin.com.

List of Figures

List of Schemes

List of Tables

Abbreviations

Å	Ångstrœm; 1 Å= 10^{-10} m
AcOH	acetic acid
API	atmospheric pressure ionization
arg	arginine
AzaBOX	aza-bisoxazoline type ligand
BArF	tetrakis-(3,5-di(trifluoromethyl)phenyl)borate)
BINAP	2,2-bis(diphenylphosphino)-1,1'-binaphthyl
BOX	bisoxazoline type ligand
BSA	N,O–bis(trimethylsilyl)acetamide
CH_2Cl_2	dichlormethane
CID	collision induced dissociation
COD	1,4-cyclooctadiene
cys	cysteine
DCC	dicyclohexyl carbodiimine
DESI	desorption electrospray ionization
DFT	density functional theory
ee	enantiomeric excesse
EHSS	exact hard–spheres scattering
ESI	electrospray ionization
ESI-MS	electrospray ionization mass spectrometry
Et_2O	diethyl ether
FFT	fast fourier transformation (digital)
FT	fourier transformation

FWHM	full with at half maximum
GC	gas chromatography
GC-MS	gas chromatography coupled to mass spectrometry
Glu-H$^+$	protonated glutaric acid
HPLC	high pressure liquid chromatography
ICL	integrated command line of the ICIS software
IFFT	inverse fast fourier transformation (digital)
IFT	inverse fourier transformation
IMS	ion mobility spectrometry
ips	l-iso-propylserine
LC	liquid chromatography
LCQ	FINNIGAN mass spectrometer ion trap type
MALDI	matrix assisted laser desorption
MAO	methylaluminiumoxane
MD	molecular dynamics
MeOH	methanol
MS	mass spectrometry
m/z	mass over charge ratio
PA	the Bower's projection approximation
PEEK	**P**oly**E**ther**E**ther**K**etone a semicrystalline thermoplastic (- 265°C)
pdme	phtalic acid dimethylester
PHOX	chiral phosphinooxazoline
PFTE	(Teflon®) **P**oly**T**etra**F**luoro**E**thylene (- 260°C)
PP	general diphosphine chelate ligand
Pt100	100Ω linearly temperature dependent platinum resistor
QMS	quadrupole mass spectrometry
RF	radio–frequency (RF)
RT	room temperature (23-26°C)
S/N	signal to noise ratio
SEDI	scattering on electron density isosurfaces

ser   serine

SSI   sonic spray ionization

tbs   threo-tert-butylserine

TFA   trifluoro acetic acid

TFE   trifluoro ethanol

thr   threonine

TM   trajectory method

TOF   turn over frequency (TON/time)

TON   turn over number

TSQ   FINNIGAN mass spectrometer triple quad type

Compound numbers

1 tetrabutylammonium tetrafluoroborate

2 tetrabutylheptylammonium bromine

3 hexadecyltrimethylammonium bromine

4 [Pd(PHOX)]

5 [Pd(PHOX)S]$^+$

6 [Pd(PHOX)(allyl)]$^+$

7 [Pd(PHOX)(allyl*)]$^+$

8 [Ir(PHOX)(COD)]$^+$ X$^-$

9 [Ir(PHOX)L$_2$]$^+$

Curriculum Vitae

Rolf Dietiker

born on August 17th, 1975 in Zürich, Switzerland

Swiss citizen (Bülach ZH and Thalheim AG)

married with Monika Jäggi since April 8th, 2000

Education:

1982–1988	Primarschule Hohfuri, Bülach
1988–1990	Sekundarschule Hinterbirch, Bülach
1990–1995	Kantonsschule Zürcher Unterland, Bülach
1995–1999	Studies in Chemistry at ETH Zürich
1999	Diploma Thesis "Zweistufige Laser-Massenspektrometrie: Quantitative Analyse von Polyaromatischen Kohlenwasserstoffen und Phenol in Wasserproben" with Prof. Dr. Renato Zenobi, ETH Zürich
since 2/2000	PhD Thesis "Steps towards Structural Information in ESI-MS Gas Phase Investigations" with Prof. P. Chen, ETH Zürich

Collaborations:

1997	SATW Project at Givaudan, Dübendorf
2000	Ch. Hinderling(Group of Prof. Dr. P. Chen), Planning and Preparation of Modifications of a Finnigan TSQ 700 ESI-MS
2001	R. Hartmann (Group of Prof. Dr. P. Chen), Development of a Water-cooled Electrospray Ionization Interface, ETH Zürich
2001	Ch. Adlhart (Group of Prof. Dr. P. Chen), Ion Mobility Measurements in a Conventional ESI Mass Spectrometer
2004	A. Zumbühl (Group of Prof. Dr. E. Carreira), Investigations on Steroid-Amphotericin Dimers